

Patient-specific CT dose determination from CT images using Monte
Carlo simulations

by

Qing Liang

A dissertation submitted in partial fulfillment of
the requirements for the degree of

Doctor of Philosophy

(Medical Physics)

at the

UNIVERSITY OF WISCONSIN-MADISON

2013

Date of final oral examination: 06/19/13

This dissertation is approved by the following members of the Final Oral Committee:

Larry A. DeWerd, Professor, Medical Physics
Guang-Hong Chen, Professor, Medical Physics
Michael W. Kissick, Assistant Professor, Medical Physics
Michael A. Speidel, Assistant Professor, Medical Physics
Weibo Cai, Assistant Professor, Radiology
Jeffrey P. Kanne, M.D., Associate Professor, Radiology

To my daughters, Lisa and Brynna. You have brought the most joy of my life.

Also to my husband, Jie, who always keeps me motivated.

Abstract

Radiation dose from computed tomography (CT) has become a public concern with the increasing application of CT as a diagnostic modality, which has generated a demand for patient-specific CT dose determinations. This thesis work aims to provide a clinically applicable Monte-Carlo-based CT dose calculation tool based on patient CT images.

The source spectrum was simulated based on half-value layer measurements. Analytical calculations along with the measured flux distribution were used to estimate the bowtie-filter geometry. Relative source output at different points in a cylindrical phantom was measured and compared with Monte Carlo simulations to verify the determined spectrum and bowtie-filter geometry. Sensitivity tests were designed with four spectra with the same kVp and different half-value layers, and showed that the relative output at different locations in a phantom is sensitive to different beam qualities.

An mAs-to-dose conversion factor was determined with in-air measurements using an Exradin A1SL ionization chamber. Longitudinal dose profiles were measured with thermoluminescent dosimeters (TLDs) and compared with the Monte-Carlo-simulated dose profiles to verify the mAs-to-dose conversion factor.

Using only the CT images to perform Monte Carlo simulations would cause dose underestimation due to the lack of a scatter region. This scenario was demonstrated with a cylindrical phantom study. Four different image extrapolation methods from the existing CT images and the Scout images were proposed. The results show that performing image

extrapolation beyond the scan region improves the dose calculation accuracy under both step-shoot scan mode and helical scan mode.

Two clinical studies were designed and comparisons were performed between the current CT dose metrics and the Monte-Carlo-based organ dose determination techniques proposed in this work. The results showed that the current CT dosimetry failed to show dose differences between patients with the same scan parameters.

The methodology proposed in this work required simple measurements on the CT scanner for scanner-specific Monte Carlo model establishment, and uses patient CT images to provide patient-specific organ dose calculations. This is an improvement on current CT dosimetry and benefits the patient dose tracking and individual risk estimates.

Acknowledgments

The five years I spent at the Calibration Laboratory at UW-Madison have been an invaluable experience in my life. I would first like to express my special appreciation to my advisor, Professor Larry DeWerd. Thank you for trusting me and giving me the opportunity of joining the lab. You have been a tremendous mentor for me. Thank you for your encouragement and support on my research work. You kept on teaching me to perform science in the correct way, and not to give up on details. You have been a great resource for ideas and advice. I have never felt afraid of explaining my thoughts to you, because I know you are always willing to listen and help.

I would like to thank my committee members, Dr. Guang-Hong Chen, Dr. Michael Kissick, Dr. Michael Speidel, Dr. Weibo Cai, and Dr. Jeffrey Kanne. Thank you for spending the time reviewing my work and giving comments on it. I sincerely appreciate the support from UW CT group led by Dr. Chen, for letting me borrow your scanner and helping me perform the scans. I could not have finished my work without the help from you.

I thank all the staff working in Cal Lab. You guys have made me feel I joined in a happy family other than just a lab. Special thanks to John Micka, Cliff Hammer, Keith Kunugi, and Denise Roche. John, you have been such a big help for everything. Every time I was in a hard situation, I just went to your desk, and I always got great advice, from research to career. Thanks Cliff for teaching me all the TLD knowledge in a very clear

and straightforward way. Your patience and kindness made my beginning year of research journey easy and fun. Keith, I appreciate your help and experience on phantom designs. Thank you Denise for taking care of all the general issues with conferences and making it easy for students! I will miss the cookies, cheese, bagels and candies at the usual place, which brought up a lot of funny conversations.

I also thank all the former and current Cal Lab students. I learned a lot from every one. My first mentor, Stephanie Junell, thank you for trying to understand my opinions all the time and giving advice especially for my first projects. Laura Bartol has been a great help on ideas from my first project to the last one. Julie Raffi, the days when we were pregnant buddies are a sweet memory, and you definitely set an excellent example of being an efficient researcher mom. Also the Research Oversight Committee (ROC) members who have given awesome suggestions on my prelim and research project, Steve Davis, Jackie Moga, Tina Pike, Adam Paxton, Regina Fulkerson, Jessica Snow, Travis McCaw, Martha Malin. Special thanks to Travis, Martha, Laura, and Joshua Reed, for editing my thesis.

I would like to thank Dr. Bruce Thomadsen and Dr. Jeni Smilowitz for giving me the opportunity of being your TA. I gained numerous experiences from that.

I also thank Dr. Ranjini Tolakanahalli and Dr. Jeni Smilowitz who spent a lot of time teaching me how to work on the machines when I was on Team Tomo and Team Johnson Creek. Thank you Dr. Jessica Klaers and Dr. Frank Goodin for giving me the chance to work at Turville Bay Radiation Oncology Center. I gained a lot of hands on clinic experience from working there.

Last but not least, I would like to express my appreciation to my family and friends. Thanks to Dad and Mom for trusting me all the time and letting me be as independent as I want. Thanks to my parents-in-law for trying so hard to help with taking care of the girls. Thanks to my husband, Jie, for being supportive, caring and loving. You are not only a good partner in life, but also a great teacher for study and research. Thanks also to Lisa

and Brynna who have made my life joyful and sweet. Thank you all the friends I met in Madison and old friends who are in China. You guys have made this a wonderful journey!

Contents

Abstract	ii
Acknowledgments	iv
List of Figures	xv
List of Tables	xvi
1 Introduction	1
1.1 Overview	1
1.2 Description of upcoming chapters	2
2 Background	4
2.1 Ionizing radiation and its biological effects	4
2.1.1 Ionizing radiation	4
2.1.2 Biological effect of radiation	5
2.2 Radiation dose from CT	7
2.2.1 Rapid increase of radiation exposure from CT	7
2.2.2 Potential risk from CT scans	8
2.3 Current CT dosimetry	10
2.3.1 Computed tomography dose index (CTDI) metrics	10
2.3.1.1 CTDI	10
2.3.1.2 Dose-length product (DLP)	12
2.3.1.3 Limitations of CTDI-based metrics	12
2.3.2 Size-Specific Dose Estimates (SSDE)	13
2.3.2.1 AAPM Task Group 204	13
2.3.2.2 The limitations of SSDE	16
2.3.3 Absorbed dose and effective dose	18
2.3.3.1 Absorbed dose measurements and calculations	18
2.3.3.2 Effective dose and weighting factors	19
2.4 Monte Carlo simulations for CT dose determination	22
2.4.1 Monte Carlo simulations	22
2.4.2 Spectrum and bowtie filter determinations	25
2.4.2.1 CT spectrum determination	25

2.4.2.2	Bowtie filter determination	27
2.4.3	Verification of Monte Carlo simulations	30
2.5	Anthropomorphic phantoms for CT dosimetry	30
2.5.1	Development of phantoms for CT dose calculations	30
2.5.1.1	Physical phantoms	30
2.5.1.2	Computational phantoms	31
2.5.2	Limitations of using phantoms for patient-specific dose determination	34
2.6	Project motivation and goals	34
3	Monte Carlo dose calculations	36
3.1	GMctdospp and cross-validation with MCNP5	36
3.1.1	GMctdospp	36
3.1.2	Cross-validation with MCNP5	39
3.1.2.1	Methods and materials	40
3.1.2.2	Results	41
3.2	Spectrum determination	43
3.2.1	Methods and materials	43
3.2.1.1	Spectrum determination methodology	43
3.2.1.2	Calibration of ionization chamber	44
3.2.1.3	HVL measurements	46
3.2.2	Results	47
3.2.2.1	Energy response of ionization chamber	47
3.2.2.2	Half-value layer of CT beam	48
3.2.2.3	Spectrum of CT beam	48
3.3	Bowtie filter determination	49
3.3.1	Flux distribution measurements on a CT scanner	49
3.3.2	Flux distribution using Monte Carlo simulations	50
3.3.3	Methodology to determine bowtie filter	50
3.3.3.1	Analytical calculations	52
3.3.3.2	Scatter correction	53
3.3.4	Results	55
3.3.4.1	Bowtie filter geometry	55
3.3.4.2	Comparison of simulated-flux and measured-flux	55
3.4	Determination of mAs-to-dose conversion factor	56
3.4.1	Methodology to determine mAs-to-dose conversion factor	56
3.4.2	Linearity test of dose and mAs	57
3.4.2.1	Methods and materials	57
3.4.2.2	Results	58
3.4.3	A1SL ionization chamber modeling and in-air measurement	59
3.4.3.1	A1SL ionization chamber calibrations	59
3.4.3.2	Measurements	60
3.4.3.3	Monte Carlo simulations	60
3.4.4	Conversion factor for absolute dose	62

4	Monte Carlo verification and clinical implementation	63
4.1	Verification of spectrum and bowtie filter	63
4.1.1	In-phantom output measurements	63
4.1.1.1	Methods and materials	64
4.1.1.2	Results	67
4.1.2	Sensitivity tests of different beam qualities	68
4.1.2.1	Descriptions of the four different spectra	69
4.1.2.2	Monte Carlo simulations	71
4.1.2.3	Results	72
4.2	TLD measurements for mAs-to-dose conversion factor	73
4.2.1	Thermoluminescent dosimeter (TLD) use and calibration	73
4.2.1.1	TLD handling	73
4.2.1.2	Chip factor determination	75
4.2.1.3	TLD air kerma calibration	77
4.2.1.4	Dose to TLD determinations	79
4.2.2	z -profile measurements on a CT scanner	80
4.2.2.1	Methods and materials	80
4.2.2.2	Comparison between simulation and measurement	81
4.2.2.3	Uncertainty analysis of TLD measurements	83
4.3	Summary and clinical implementation	84
5	Image extrapolations	86
5.1	Cylindrical phantom study	88
5.1.1	Methods and materials	88
5.1.2	Results	91
5.2	Anthropomorphic phantom study	97
5.2.1	Methods and materials	97
5.2.1.1	CT scan	97
5.2.1.2	Monte Carlo simulations	98
5.2.1.3	Image extrapolation methods	99
5.2.2	Results	102
5.2.2.1	Nearest neighbor and linear extrapolations	102
5.2.2.2	Extrapolation using Scout images	105
5.3	Summary of image extrapolations	110
6	Clinical studies on patient CT dose	112
6.1	Study design	112
6.1.1	CTDI _{vol} and DLP determinations	113
6.1.2	Effective dose determinations	114
6.1.3	SSDE determinations	114
6.1.4	Monte-Carlo-based organ dose determinations	115
6.1.4.1	Image processing	115
6.2	Clinical study case 1	116
6.2.1	CT images and patient size measurement	116

6.2.2	Scan parameters for Monte Carlo simulations	118
6.2.3	Results	118
6.2.3.1	Dose determinations following current CT dosimetry	118
6.2.3.2	Monte-Carlo-based dose determinations	121
6.2.3.3	Summary for clinical study 1	122
6.3	Clinical study case 2	123
6.3.1	CT images and patient size measurement	123
6.3.2	Scan parameters for Monte Carlo simulations	124
6.3.3	Results	124
6.3.3.1	Dose determinations following current CT dosimetry	124
6.3.3.2	Monte-Carlo-based dose determinations	125
6.3.3.3	Summary for clinical study 2	126
6.4	Uncertainty analysis	126
7	Conclusions and future work	128
7.1	Conclusions	128
7.1.1	Monte Carlo model establishment and verification	128
7.1.2	Determination and verification of mAs-to-dose conversion factor	129
7.1.3	Image extrapolations	129
7.1.4	Clinical studies	130
7.2	Future work	130
7.2.1	CT dose calculations for CT-based screenings	130
7.2.2	Modeling for mA modulated CT scans	131
7.2.3	In-phantom dose calibrations of TLDs for CT sources	133
	Bibliography	136

List of Figures

2.1	Linear no-threshold model, threshold model and hormetic model. The x-axis represents the radiation dose and the y-axis the likelihood of a potential risk, such as cancer. From Siemens, “Guide to Low Dose”.	6
2.2	Plot of the estimated number of CT scans performed annually in the United States from 1980 to 2006. From IMV 2006 CT Market Summary Report. . .	7
2.3	Number of CT scanners per million people in selected G8 countries for which time series were available, 1990 to 2005. From Medical Imaging in Canada, 2005.	8
2.4	Radiation dose from different medical procedures in the 1980s and 2006 in the United States.	8
2.5	Photograph of the head and body CT dose phantoms and a pencil ionization chamber.	11
2.6	The various tools used by the four independent research groups: (A) McCollough and colleagues (Mc) performed physical dose measurements using a series of eight anthropomorphic tissue-equivalent phantoms. (B) Toth and Strauss (TS) used two existing cylindrical PMMA phantoms, the 16 cm and 32 cm diameter CT dose phantoms, and a third 10 cm diameter phantom. (C) McNitt-Gray and colleagues (MG) performed Monte Carlo dose calculations using a series of seven anthropomorphic mathematical phantoms, of which three are shown here. (D) Boone and colleagues (ZB) used Monte Carlo calculations on a series of cylinders of different diameters with different compositions. The figures are adopted from AAPM TG-204 [2011]. . . .	14
2.7	Plot of the normalized dose coefficient as a function of effective diameter (a) for a 32 cm diameter PMMA CT dose phantom, and (b) for a 16 cm diameter PMMA CT dose phantom, from AAPM report TG-204 [2011].	17
2.8	Mathematical phantom used with ImPACT spreadsheet to compute patient organ doses for CT. Picture from www.impactscan.org	20
2.9	Weighting factors for different organs and tissues from ICRP publications 26 [1977], 60 [1991], and 103 [2007].	21
2.10	Flowchart for the development, validation and application of CT models to calculate organ dose using Monte Carlo simulations, from Gu et al. [2009].	24
2.11	A schematic of a CT scanner model, from Gu et al. [2009].	25
2.12	Screenshot of the SpekCalc GUI.	27
2.13	A photograph of a typical bowtie filter made of Teflon.	28

2.14	Diagram of bowtie profile measurements of attenuation across the fan beam. [Turner et al., 2009]	29
2.15	Photographs of (a) Rando phantoms (The Phantom Laboratory, Salem, NY, USA), (b) ATOM phantoms (CIRS, Norfolk, VA, USA), (c) whole body phantom PBU-60 (Kyoto Kagaku Co., Japan).	31
2.16	(a) MIRD-5 hermaphrodite adult phantom, (b) ORNL phantoms for different ages, (c) GSF phantoms ADAM and EVA, (d) RPI pregnant female phantom.	33
3.1	A screen shot of the GMctdospp GUI. The scan parameters can be set in the area shown on the left. The dose distribution on the transverse plane and a dose profile along a certain direction shown by the green line in the dose distribution image are demonstrated here.	38
3.2	Depth dose profile along the central axis at different distances from the phantom surface.	41
3.3	Axial planar dose distribution: (a) GMctdospp and (b) MCNP5.	42
3.5	Sagittal planar dose distributions: (a) GMctdospp and (b) MCNP5.	42
3.4	Coronal planar dose distributions: (a) GMctdospp and (b) MCNP5.	43
3.6	Workflow for spectrum determination in this work.	44
3.7	Photograph of Capintec PS-033 ionization chamber used in this work: (a) front, (b) back.	45
3.8	Photograph of the HVL measurement setup.	47
3.9	Determined large body spectrum of the GE HD750 CT scanner using 120 kVp.	49
3.10	Workflow to determine the effective bowtie filter. “BT” stands for bowtie filter, and “MC” stands for Monte Carlo.	51
3.11	Not-to-scale drawing of a CT scanner configuration with bowtie filter in the beam.	53
3.12	Comparison of flux distribution between analytical calculations and Monte Carlo simulations using the starting bowtie geometry.	54
3.13	EGSnrc rendering of the determined large-body bowtie filter shape.	55
3.14	Comparison between the simulated and measured post-bowtie-filter flux distributions.	56
3.15	Photograph of linearity test setup. The Exradin A101 ionization chambers was placed in the central insert of the head CT dose phantom.	58
3.16	The relationship between the ionization chamber readings and different mAs settings.	59
3.17	Photograph of the setup of A1SL in-air CT scan.	60
3.18	The manufacturer-provided dimension information (a) and the EGSnrc rendering of an Exradin A1SL ionization chamber (b).	61
4.1	Photograph of the CT dose phantom kit used for output measurements. An Exradin A101 CT ionization chamber is inserted at one of the peripheral locations.	65

4.2	The axial view of the CT dose phantom kit. The images of the phantom were used to perform dose calculations using GMctdospp. No ionization chamber was inserted into this phantom. The x , y , and z directions are shown to represent the coordinates of CT system.	67
4.3	The dose distribution (mGy/mAs) within the central slice along the z direction.	68
4.4	Four different spectra for the sensitivity test of simulated output for different beam qualities.	71
4.5	The x -direction dose profiles crossing the center of the phantom within the central axial plane of the CT dose phantom when using the four different spectra for Monte Carlo simulations.	72
4.6	Photograph of an aluminum holder for TLD annealing.	76
4.7	Setup for ^{60}Co irradiations of TLDs.	77
4.8	Custom-designed holder for x-ray irradiations of TLDs.	78
4.9	Photograph of the custom-designed TLD insert for z -direction profile measurements	80
4.10	Comparison of TLD-measured z profile (dose to TLD) and Monte-Carlo-simulated z profile (dose to PMMA). For these profiles, the beam width is 20 mm.	83
5.1	Illustration of the mathematical water cylinder size and scanned region (shown in blue).	89
5.2	Locations for dose comparison between using only the images within the scanned region and the gold standard. The diamonds show the different locations along the z direction. The location where $z = 0$ cm represents the center of the cylinder. (a) Locations are on the central axis of the cylinder. (b) Locations are at 1 cm from the periphery of the cylinder, i.e. 9 cm from the center of the cylinder.	90
5.3	Illustration of scanned region and various scatter region sizes for the mathematical phantom study.	90
5.4	Longitudinal dose profiles within the scanned region using the images within the scanned region only and the gold standard for a collimation size of 40 mm. (a) Longitudinal dose profile at the central location of the cylinder. (b) Longitudinal dose profile at 1 cm from the edge of the cylinder.	92
5.5	Illustration of the groves on the dose profiles at the edge of the cylinder. The dash line shows the isocenter positions when the source rotates.	93
5.6	Dose underestimation on the edge slice of the cylinder with different scatter regions. Comparisons were made with the gold standard. The simulations were performed using a 40 mm collimation.	94
5.7	Longitudinal dose profiles within the scanned region using the images within the scanned region only and the gold standard for a collimation size of 5 mm. (a) Longitudinal dose profile at the central location of the cylinder. (b) Longitudinal dose profile at 1 cm from the edge of the cylinder.	96

5.8	Dose underestimation on the edge slice of the cylinder with different scatter regions. Comparisons were made with the gold standard. The simulations were performed using a 5 mm collimation.	97
5.9	Photograph of the setup for the CT scan of a male anthropomorphic phantom.	98
5.10	(a) The coronal view of a chest scan with the red line indicating the slice used for the nearest neighbor stacking (left), and the extrapolated scatter region shown in the dashed boxes generated by the nearest neighbor stacking (right). (b) The coronal view of a chest scan with the red lines indicating the slices used for the linear extrapolation (left) and the extrapolated scatter region shown in the dashed boxes generated by the linear extrapolation (right).	100
5.11	(a) The determination of the long and short axes at a z location from AP and lateral scout images; (b) the coronal view of the chest scan with the scatter region shown in dashed boxes generated by the ellipses based on scout images; (c) the coronal view of the chest scan with the scatter region shown in dashed boxes generated by resized nearest neighbor based on scout images.	101
5.12	Dose difference (%) on the inferior slice of the chest scan (pelvic) compared to using whole-body Rando CT images. Monte Carlo simulations were performed for a step-shoot scan mode using (a) chest CT images; (b) chest CT images with extrapolated images by stacking the nearest neighbor; and (c) chest CT images with extrapolated images by linear extrapolation of 5 slices on the edge.	103
5.13	Dose difference (%) on the superior slice of the chest scan (shoulder) compared to using whole-body Rando CT images. Monte Carlo simulations were performed for a step-shoot scan mode using (a) chest CT images; (b) chest CT images with extrapolated images by stacking the nearest neighbor; and (c) chest CT images with extrapolated images by linear extrapolation of 5 slices on the edge.	104
5.14	Dose difference (%) on the inferior slice of the chest scan (pelvic) compared to using whole-body Rando CT images. Monte Carlo simulations were performed for a helical scan mode using (a) chest CT images; (b) chest CT images with extrapolated images by stacking the nearest neighbor; and (c) chest CT images with extrapolated images by linear extrapolation of 5 slices on the edge.	106
5.15	Dose difference (%) on the superior slice of the chest scan (shoulder) compared to using whole body Rando CT images. Monte Carlo simulations were performed for a helical scan mode using (a) chest CT images; (b) chest CT images with extrapolated images by stacking the nearest neighbor; and (c) chest CT images with extrapolated images by linear extrapolation of 5 slices on the edge.	107
5.16	Dose difference (%) on the inferior slice of the chest scan (pelvic) compared to using whole-body Rando CT images. Monte Carlo simulations were performed for a step-shoot scan mode using (a) chest CT images plus the ellipses determined from Scout images and (b) chest CT images plus the resized nearest neighbor extrapolated images.	108

5.17	Dose difference (%) on the superior slice of the chest scan (shoulder) compared to using whole-body Rando CT images. Monte Carlo simulations were performed for a step-shoot scan mode using (a) chest CT images plus the ellipses determined from Scout images and (b) chest CT images plus the resized nearest neighbor extrapolated images.	108
5.18	Dose difference (%) on the bottom slice of the chest scan (pelvic) compared to using whole body Rando CT images. Monte Carlo simulations were performed for a helical scan mode. (a) using chest CT images plus the Scout-images-determined ellipses ; (b) using chest CT images plus the extrapolated images by resized nearest neighbor.	109
5.19	Dose difference (%) on the superior slice of the chest scan (shoulder) compared to using whole body Rando CT images. Monte Carlo simulations were performed for a helical scan mode. (a) using chest CT images plus the Scout-images-determined ellipses ; (b) using chest CT images plus the extrapolated images by resized nearest neighbor.	110
6.1	Determined dose-related term normalized to patient (a) from current CT dosimetry.	120
6.2	Determined dose-related term normalized to patient (a) from current CT dosimetry.	122
6.3	Axial CT images of abdomen/pelvis patient (left) and CTC patient (right).	123
7.1	Illustration of the concept of angular mA modulation, in which the tube current (mA) (vertical axis) is varied as the x-ray tube rotates around the patient (horizontal axis). Adopted from McCollough et al., 2006.	132
7.2	Graph of tube current (in mA) superimposed on a CT projection radiograph that illustrates the concept of z-axis modulation, with variation of the tube current along the z-axis. The curve is determined by using attenuation data from the CT projection radiograph and a manufacturer-specific algorithm. Adopted from McCollough et al., 2006.	132
7.3	Photograph of the custom-designed PMMA cylindrical insert for A1SL ionization chamber.	134

List of Tables

2.1	Published k coefficients for effective dose calculations based on DLP.	23
3.1	kVp, HVL1, HVL2 and air-kerma calibration coefficients N_k for PS-033 ionization chamber for four beams at the UWADCL.	48
4.1	Comparisons of the output at different locations relative to isocenter between in-phantom measurements and Monte Carlo simulations.	69
4.2	The kVp and HVL of the four x-ray beams for sensitivity test.	70
4.3	Differences of the output relative to center at each location between in-phantom measurements and Monte Carlo simulations, and the root mean square deviation (RMSD) of the differences at three locations for four different beam qualities.	74
4.4	Uncertainties related to Monte-Carlo calculated organ dose.	84
5.1	Dose underestimation at different locations when using only the images within the scanned region compared to the gold standard. Collimation size: 40 mm.	93
5.2	Dose underestimation at different locations when using only the images within the scanned region compared to the gold standard. Collimation size: 5 mm.	95
6.1	Coronal views of the patient CT images for the three patients.	117
6.2	Averaged effective diameters and scan lengths for the three patients in clinical study 1.	118
6.3	Patient CT doses determined from current CT dosimetry.	120
6.4	Patient CT doses determined from current CT dosimetry. Values are normalized to patient (a).	120
6.5	Patient CT doses determined with Monte Carlo simulations.	121
6.6	Patient CT doses determined with Monte Carlo simulations. Values are normalized to patient (a).	121
6.7	Averaged effective diameters and scan lengths for the two patients in clinical study 2.	124
6.8	Patient CT doses determined from current CT dosimetry.	125
6.9	Patient CT doses determined with Monte Carlo simulations.	125
6.10	Differences of Monte-Carlo-calculated organ dose between the two patients.	126
6.11	Uncertainties related to Monte-Carlo calculated organ dose.	127

Chapter 1

Introduction

1.1 Overview

With the expanding use of computed tomography (CT), the radiation dose received by patients from CT scans has become a major public concern. CT is the single largest source of medical radiation exposure to the population of the United States, contributing half of the total medical exposure in 2006 [NCRP Report 160, 2006]. As there is an increasing demand for individual dose tracking of medical imaging radiation exposures [Amis et al., 2007], a clinically applicable methodology for patient-specific CT dose determination has become necessary. Knowledge of the dose received and the associated risk for a patient can provide insight about any additional risk that may arise from CT, and help providers to carefully consider the necessity and frequency of CT examinations. An accurate determination of dose from CT scans also helps to estimate the risk of secondary cancers to the population from CT scans [Hall and Brenner, 2008].

Current dose reports from CT scanners use computed tomography dose index (CTDI)-based metrics. CTDI only accounts for scanner output, and does not calculate patient-specific dose. AAPM Task Group 204 (TG-204) recommends Size-Specific Dose Estimates (SSDE) to make patient-size-specific dose corrections, however, it does not take the patient

anatomy into account. The goal of this work is to develop a clinically applicable dosimetry package for the medical physicist to estimate the patient-specific organ dose from CT scans based on the CT images using Monte Carlo simulations.

1.2 Description of upcoming chapters

Chapter 2 describes the basic interaction physics of x-ray radiation and the increasing use of CT. It provides an overview of the current CT dose metrics and their limitations. The project motivation and goals are presented in this chapter.

In Chapter 3, cross validation of GMctdospp, the Monte Carlo simulation program used in this work, is described. The characterization of two essential parts of an accurate CT scanner, the source spectrum and the bowtie-filter geometry are discussed. Since the calculated dose from a Monte Carlo simulation is normalized per starting particle, a method to determine the conversion factor to dose at different mAs levels (mAs-to-dose conversion factor) is introduced. Linearity tests between dose and mAs with in-phantom ionization chamber measurement are included.

Chapter 4 presents the validation of the Monte Carlo model and the mAs-to-dose conversion factor determined in Chapter 3. Methodology of comparing relative output measurements at different locations in a cylindrical phantom with simulations is described. A sensitivity test of this methodology is presented. TLD measurements of z-direction profiles are included to verify the determined mAs-to-dose conversion factor. It also discusses the clinical implementation of CT Monte Carlo model based on simple measurements on a CT scanner.

Chapter 5 demonstrates a possible situation when the dose would be underestimated without taking the scatter from the regions adjacent to the scan region into account, using a cylindrical phantom study. With the cylindrical phantom study, the amount of scatter region required for accurate dose calculations is also presented. In this chapter, four different

image extrapolation methods are presented based on an anthropomorphic phantom study to approximate the scatter conditions and to improve the dose calculation accuracy.

Chapter 6 presents two clinical studies using the Monte-Carlo-based dose calculation tool provided in this thesis. Comparisons with the current CT dosimetry, including $CTDI_{vol}$, DLP, effective dose, SSDE are performed for both of the clinical cases.

Chapter 7 provides an overall summary of the work. Several possible future research directions related to this work are also discussed.

Chapter 2

Background

Radiation dose from computed tomography (CT) has become a public concern as a result of its increasing application for diagnostic purposes. In this chapter, the basic interaction physics of x-ray radiation is described. The current CT dosimetry methods and their limitations are reviewed. Project motivation and research goals are described.

2.1 Ionizing radiation and its biological effects

2.1.1 Ionizing radiation

Radiation describes the emission and propagation of energy from a central source within vacuum or medium. Depending on the range of energy involved, radiation can be divided into two categories: non-ionizing radiation (e.g., radio waves, heat, and visible light) and ionizing radiation. Ionizing radiation refers to radiation in which the energy is high enough to liberate electrons from an atom or molecule, i.e. ionization. Photons and particles with energies greater than 5-10 eV are considered ionizing. X-rays used in CT have a energy range of 50-140 keV and are ionizing. In this thesis radiation refers to this ionizing radiation only. Other types of ionizing radiation sources such as alpha particles, beta particles and gamma rays are not discussed here.

2.1.2 Biological effect of radiation

Ionizing radiation can be harmful and potentially produce lethal damage to the human body because it causes damage to tissues and organs, although within a certain dose range, it can have health benefits in radiation therapy for the treatment of cancer and thyrotoxicosis. There are two mechanisms by which radiation damages the human body: (1) radiation interacts directly with the DNA of the cells by ionizing atoms in its molecular structure or, (2) radiation interactions with water to create free radicals, which are atoms, molecules, or ions with unpaired electrons. These unpaired electrons are usually highly reactive and are likely to participate in chemical reactions that eventually change or harm the DNA of the cells.

The human body can repair much of the DNA injury. However, when the radiation dose is higher than a threshold, deterministic effects are observed, such as radiation burns, acute radiation syndrome, chronic radiation syndrome, and radiation-induced thyroiditis. Exposure levels of typical medical diagnostic imaging procedures are, in general, much lower than the threshold for deterministic radiation damage, and only have stochastic effects on human health. Stochastic effects are effects whose probability of occurrence increases with the radiation dose received, while the severity is independent of dose. In these cases, cellular self-repair mechanisms may fail, and some cells may experience non-lethal DNA modifications that are passed on through subsequent cell divisions. Examples of stochastic effects from radiation include cancer, leukemia, genetic effects, cataracts, and heart disease.

Much of the data on radiation-induced cancers in humans comes from the Hiroshima and Nagasaki atomic bomb survivors, in which the exposure to the population was primarily from gamma rays and neutrons emitted almost simultaneously with the bomb explosion. The effect of very low amounts of radiation is still subject to debate. The models used to predict the effects of low amounts of radiation: the linear, no-threshold model, the threshold model and the hormetic model. The linear, no-threshold model assumes that

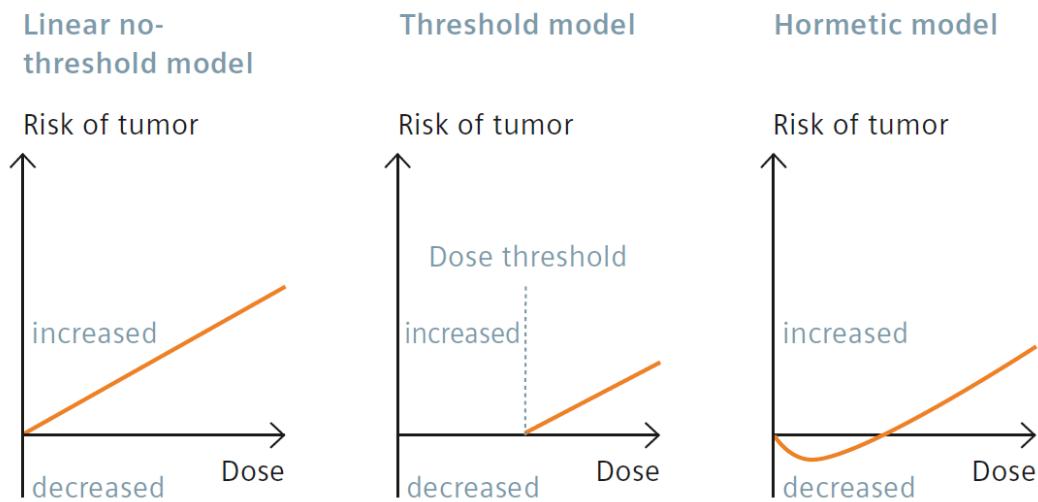


Figure 2.1: Linear no-threshold model, threshold model and hormetic model. The x-axis represents the radiation dose and the y-axis the likelihood of a potential risk, such as cancer. From Siemens, “Guide to Low Dose”.

even the smallest radiation exposure carries a risk, and the risk from radiation is linearly proportional to the dose level. The threshold model proposes that any exposure below a given threshold is safe, and only if this level is exceeded does the probability of radiation damage increase proportionally to the received radiation. More recently, the hormetic model has been proposed to describe the relationship between the cancer risk and the radiation dose. This model proposes that at very low doses, the cancer risk is lower than that for zero dose. The three types of models are shown in Figure 2.1 [Siemens]. While all three models agree that large radiation doses are harmful to humans, each model differs on the risk prediction associated with the exposure to low levels of radiation.

2.2 Radiation dose from CT

2.2.1 Rapid increase of radiation exposure from CT

Since its inception in the 1970s, CT has provided many benefits to the public as a diagnostic imaging modality. The utilization of CT imaging as a tool for diagnosing or confirming disease has increased dramatically since the introduction of CT, especially with the development of multi-slice CT and helical CT. In 2006, approximately 62 million CT examinations were performed in hospitals and outpatient imaging facilities in the United States, as compared with 3 million in 1980 (see Figure 2.2) [IMV]. This increasing trend is also evident in other countries. Figure 2.3 shows the number of CT scanners per million population several selected G8 countries [2005].

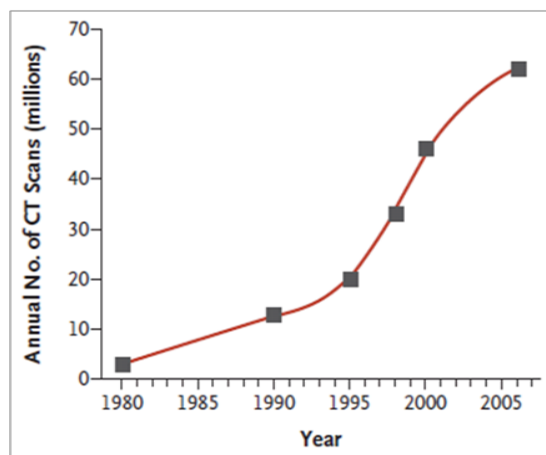


Figure 2.2: Plot of the estimated number of CT scans performed annually in the United States from 1980 to 2006. From IMV 2006 CT Market Summary Report.

With the increasing use of CT, the radiation exposure from CT scans has become the primary contributor to the public medical exposure. According to National Council on Radiation Protection and Measurements (NCRP) report No. 160 [2006], in 2006, CT scans contributed half of the total patient medical exposure. The annual per capita radiation dose from medical exposure rose from 0.53 mSv to 3.1 mSv from 1980 to 2006 (see Figure 2.4).

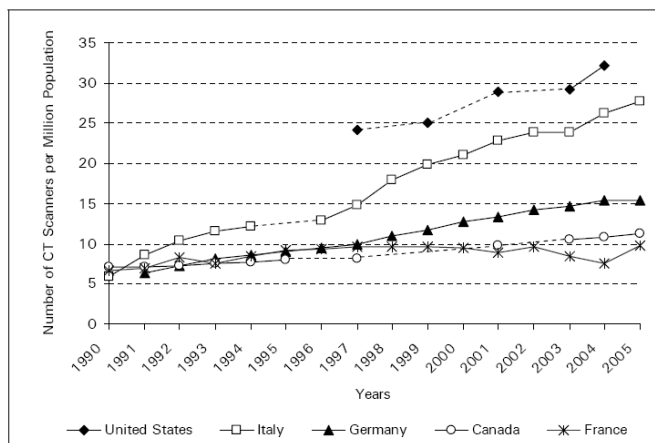


Figure 2.3: Number of CT scanners per million people in selected G8 countries for which time series were available, 1990 to 2005. From Medical Imaging in Canada, 2005.

Similarly, in the United Kingdom, CT scans accounted for 20% of the annual collective dose due to all radiological exams in 1990. The estimated contribution from CT is believed to have increased to 40% in 1998, and to 50% in 2003.

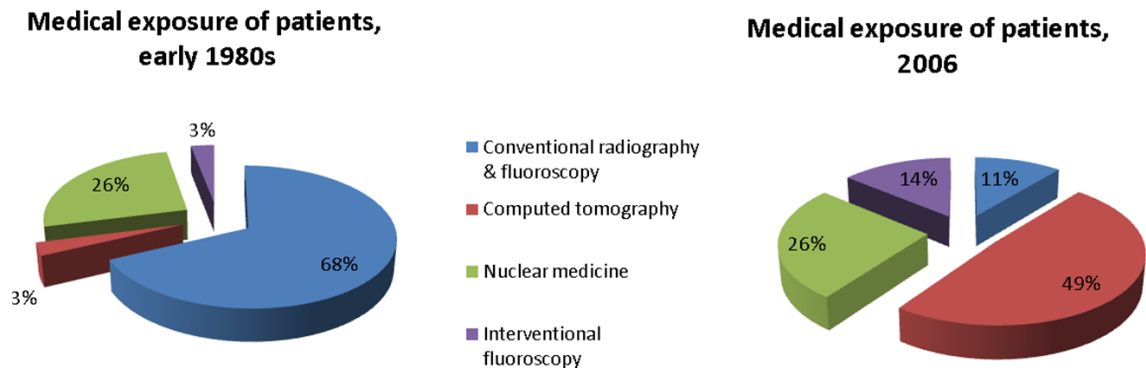


Figure 2.4: Radiation dose from different medical procedures in the 1980s and 2006 in the United States.

2.2.2 Potential risk from CT scans

The effective dose of radiation associated with most CT scans are typically low, on the order of 1.0-12.0 mSv [2006]. However, there have been several published papers showing

that CT scans may be responsible for increasing cancer risk [Brenner and Hall, 2007, Smith-Bindman et al., 2009, González et al., 2009]. Brenner and Hall used the data from survivors of the atomic bombs dropped on Japan in 1945, who were exposed to an average dose of approximately 20 mSv to predict radiation-related risks in a population [Brenner and Hall, 2007]. They found that organ doses corresponding to a common CT study result in an increased risk of cancer, especially for children. The American Association of Physicists in Medicine (AAPM) released a statement in response to this paper in November 2007 to point out the flaws of the data and mathematical assumptions used in Brenner’s analysis, and tried to prevent the public from being misled by this paper [2007]. In 2009, the AAPM made a similar statement in response to two other published articles [Smith-Bindman et al., 2009, González et al., 2009] that suggests the increased use of diagnostic CT leads to the cancer deaths of tens of thousands of Americans each year [2009]. The AAPM pointed out that the series of assumptions used in these articles utilized the worst case scenarios and the most conservative assumptions. In June 2012, the AAPM restated that the risk from CT scans should not be overlooked and that CT scans are an important diagnostic tool when used appropriately [2012].

Although it is still not clear whether there is an increased cancer risk due to radiation dose from a typical CT scan, a recent medical misadministration has intensified the scrutiny to CT scan safety. In October 2009, the Food and Drug Administration (FDA) issued an initial safety notification to 206 patients who had been exposed to excess radiation from brain perfusion CT studies at Cedar-Sinai Medical Center in Los Angeles, CA, over an 18-month period. As a result of these events, the state of California passed the first law in the United States that will require hospitals and clinics to record the radiation dose to any patient who receives a CT scan. California Senate Bill 1237 went into effect in July 2012 and requires $CTDI_{vol}$ and DLP to be printed on the patient’s radiology record (see Section 2.3.1 for definition of $CTDI_{vol}$ and DLP).

2.3 Current CT dosimetry

2.3.1 Computed tomography dose index (CTDI) metrics

2.3.1.1 CTDI

CTDI is currently the primary method for measuring CT dose. The AAPM Report 96 [2008] recommends CTDI-based metrics as the reference CT standard for measuring, comparing, and communicating of CT dose. CTDI is defined as

$$\text{CTDI} = \frac{1}{NT} \int_{-\infty}^{\infty} D(z) dz, \quad (2.1)$$

where $D(z)$ is the radiation dose profile along the z axis, N is the number of tomographic sections imaged in a single axial scan, and T is the nominal scan width. After normalizing with the nominal scan width, the CTDI has a unit of mGy. CTDI is measured from one axial CT scan and is calculated by dividing the integrated absorbed dose by the nominal total beam collimation. It should be noted that although CTDI has the same units as dose (mGy), they are inherently different. CTDI represents an average energy deposition within a specified phantom, and does not directly represent a point dose.

The integral of the dose profile with the limits of infinity is not practical to measure, so CTDI_{100} is typically used. CTDI_{100} represents the accumulated multiple-scan dose at the center of a 100-mm scan. Setting the integration limits to ± 50 mm, CTDI_{100} is expressed as:

$$\text{CTDI}_{100} = \frac{1}{NT} \int_{-50 \text{ mm}}^{50 \text{ mm}} D(z) dz. \quad (2.2)$$

CTDI_{100} is commonly measured with a commercially available pencil ionization chamber in a simple cylindrical phantom (shown in Figure 2.5) on a stationary patient table. Most

CT ionization chambers have a 100 mm nominal length. With a single-rotation CT scan to the center of the ionization chamber, the integral dose along the z direction can be calculated by the chamber reading, and the CTDI_{100} is determined by taking the chamber-measured integral dose divided by the nominal beam width.



Figure 2.5: Photograph of the head and body CT dose phantoms and a pencil ionization chamber.

CTDI_{100} is defined at the center of the field of view; however, CTDI varies across the field of view. The CTDI_{100} measured in the body phantom (with a diameter of 32 cm) is typically a factor of two higher at the surface of the phantom compared to the phantom center. The weighted CTDI (CTDI_w) is defined to provide an estimate of the CTDI_{100} averaged across the field of view. CTDI_w gives a weight of $\frac{1}{3}$ to the CTDI_{100} measured at the central location within the phantom ($\text{CTDI}_{100, \text{center}}$) and a weight of $\frac{2}{3}$ to the CTDI_{100} measured at the edge locations within the phantom ($\text{CTDI}_{100, \text{edge}}$), as shown in Equation 2.3.

$$\text{CTDI}_w = \frac{1}{3}\text{CTDI}_{100, \text{center}} + \frac{2}{3}\text{CTDI}_{100, \text{edge}} \quad (2.3)$$

All CTDI measurements made with a pencil ionization chamber are performed with a stationary patient table. To represent dose for a specific scan protocol, it is essential to take into account any gaps or overlaps between the radiation dose profiles from consecutive rotations of the source. For this purpose, the volume CTDI (CTDI_{vol}) is defined as

$$\text{CTDI}_{\text{vol}} = \frac{1}{\text{pitch}} \times \text{CTDI}_{\text{w}}. \quad (2.4)$$

Pitch is defined as the table travel per rotation divided by the collimation of the x-ray beam for helical CT scans. Whereas CTDI_{w} represents the average absorbed dose over the x and y directions at the center of the scan, CTDI_{vol} represents the average absorbed dose over the x , y and z directions. However, CTDI_{vol} does not represent the average dose for objects of substantially different size, shape, or attenuation. Further, it does not indicate the total energy deposited into the scan volume, since the scan length is not taken into account.

2.3.1.2 Dose-length product (DLP)

The z direction coverage of the scans varies from scan to scan and patient to patient. To better represent the total energy delivered by a given scan protocol, the absorbed dose can be integrated along the scan length to compute the dose-length product (DLP):

$$\text{DLP (mGy} \cdot \text{cm)} = \text{CTDI}_{\text{vol}} \text{ (mGy)} \times \text{scan length (cm)}. \quad (2.5)$$

Since CTDI_{vol} represents the average dose within the phantom, DLP is considered a proxy for the total absorbed dose in a phantom over the length of a scan.

Both CTDI_{vol} and DLP are typically displayed on modern scanner consoles before and after a CT scan is performed. This information is commonly used for scan parameter optimization and patient records.

2.3.1.3 Limitations of CTDI-based metrics

Although widely implemented in the clinics, CTDI is not a physically appropriate way to estimate patient dose [McCollough et al., 2011]. The insufficient length of a 100-mm-long

pencil ionization chamber underestimates the dose deposited in the phantom [Dixon, 2003]. In addition, depending on the effective length of the pencil ionization chamber, the response of the chamber can vary up to 20% over its length [Jensen et al., 2006], which would affect the measurement of CTDI_{vol} and DLP. Moreover, CTDI-based metrics only provide a measure of the CT scanner output in phantom and do not directly correspond to patient dose. In addition to scanner output, the patient dose is also directly related to the size and anatomy of the patient. For a given CT scanner output, patients with different sizes and anatomy would have different absorbed organ and tissue doses. CTDI-based measurements are based on a phantom only, and do not take patient size or anatomy into account. As a result, CTDI and DLP cannot provide adequate information on the amount of dose a specific patient gets from a CT scan.

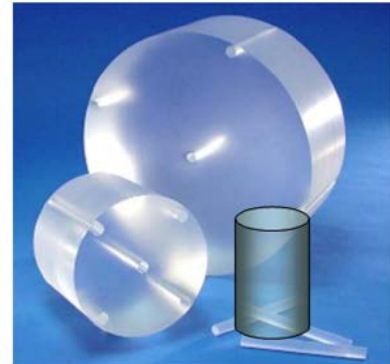
2.3.2 Size-Specific Dose Estimates (SSDE)

2.3.2.1 AAPM Task Group 204

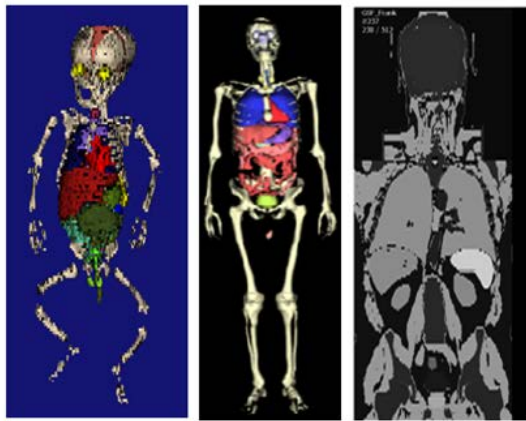
AAPM Task Group 204 (TG-204) released a report in 2011 titled “Size-Specific Dose Estimates (SSDE) in Pediatric and Adult Body CT Examinations” [2011]. This report suggested applying a correction factor to CTDI_{vol} to estimate size-specific patient dose. This recommendation is based on the work of four independent research groups that investigated the relationship between patient dose and patient size. The research was done either with physical measurements on cylindrical or anthropomorphic phantoms, or with Monte Carlo simulations on cylindrical or voxelized anthropomorphic phantoms. The tools used by these four research groups are shown in Figure 2.6.



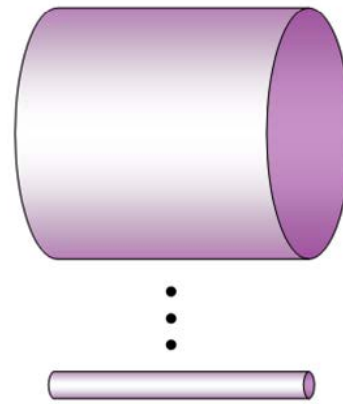
A. Physical Anthropomorphic Phantoms
(McCollough and collaborators, Mc)



B. Cylindrical PMMA phantoms
(Toth and Strauss, TS)



C. Monte Carlo Voxelized Phantoms
(McNitt-Gray and collaborators, MG)



D. Monte Carlo Mathematical Cylinders
(Boone and collaborators, ZB)

Figure 2.6: The various tools used by the four independent research groups: (A) McCollough and colleagues (Mc) performed physical dose measurements using a series of eight anthropomorphic tissue-equivalent phantoms. (B) Toth and Strauss (TS) used two existing cylindrical PMMA phantoms, the 16 cm and 32 cm diameter CT dose phantoms, and a third 10 cm diameter phantom. (C) McNitt-Gray and colleagues (MG) performed Monte Carlo dose calculations using a series of seven anthropomorphic mathematical phantoms, of which three are shown here. (D) Boone and colleagues (ZB) used Monte Carlo calculations on a series of cylinders of different diameters with different compositions. The figures are adopted from AAPM TG-204 [2011].

The first group, McCollough et al. at the Mayo Clinic (Rochester, MN), performed physical measurements using a set of eight tissue-equivalent anthropomorphic phantoms (CIRS, Norfolk, VA) to cover different sizes of patients from newborn to large adult with lateral dimensions ranging from 9 cm to 39 cm. The phantoms were all 15 cm in length. The exposure from the CT scans was measured using a 0.6 cm³ ionization chamber (Radcal, Monrovia, CA) and converted to dose to tissue (mGy) using an f-factor of 1.073 mGy [dose]/mGy [air kerma] or 9.27 mGy [dose]/R [exposure]. During the exposure measurements, scatter material with similar attenuation properties to tissue was placed adjacent to the CIRS phantom along the longitudinal direction to simulate the realistic scattering environment. The phantoms were scanned using helical (spiral), axial (sequential), and cine (perfusion) scan protocols on CT scanners from four different manufacturers, and the mean dose was divided by CTDI_{vol} at each patient size.

The second group, Toth and Strauss, used standard 15 cm long, 16 cm and 32 cm diameter PMMA phantoms, and a 15 cm long, 10 cm diameter CTDI cylinder to perform physical measurements. Standard CTDI_{vol} for 16- and 64-slice CT scanners from the same four manufacturers were measured using kV values from 80 kV to 140 kV. In their work, they used water-equivalent diameters for a cohort of head, chest, and body CT radiographs and CT images from pediatric patients, as well as measurement of the patient's lateral dimension using electronic calipers. A set of scale factors that estimate the dose to a 15 cm long phantom having the same water-equivalent diameters as the patients were shown in their results.

McNitt-Gray et al. at the University of California-Los Angeles used Monte Carlo simulations to study the effect of patient size on organ dose for abdominal CT exams. Eight voxelized patient models, known as the GSF patient models [Petoussi-Henss et al., 2002] were used to represent a range of sizes from newborn to large adult including males and females. The simulated scan lengths ranged from 15 cm to 33 cm. For each patient model,

the scanner-specific organ doses were calculated and normalized by corresponding CTDI_{vol} and averaged across scanners to obtain scanner-independent organ dose per CTDI_{vol} coefficients. The patient size was determined by the outer perimeter of each patient measured at the central slice of the abdominal scan region. The relationship between organ dose per CTDI_{vol} coefficients and patient perimeter was investigated for organs that were directly irradiated by the abdominal scan.

The last group, Zhou and Boone at the University of California-Davis also performed Monte Carlo simulations to compute dose to infinitely long cylinders of different materials (water, PMMA and polyethylene). The diameters ranged from 1 cm to 50 cm in 22 increments. The Monte-Carlo-determined air kerma values for the 16 cm and 32 cm PMMA phantoms were used and normalized to the physically measured CTDI_{vol} .

TG-204 combined the results from these four groups and found that there is a clear dependence of patient dose on patient size. It also showed that this dependence could be represented by the lateral dimension, anterior-posterior (AP) dimension, lateral plus AP dimension, or the effective diameter (the diameter of a circle having an area equal to that of the patient cross section) on a CT image. Two plots from TG-204, as shown in Figure 2.7, show the relationship between dose and the effective diameter. Based on the combined data, a set of patient-size-dependent conversion factors were presented to convert CTDI_{vol} to the new patient dose estimate, SSDE. The patient size information can be measured from either the reconstructed CT image or the CT radiograph, using either the lateral dimension, the AP dimension, lateral plus AP dimension, or the effective diameter.

2.3.2.2 The limitations of SSDE

The simple measurement of patient size makes the SSDE metrics one step closer to patient-specific dose. While the dose report method suggested in TG-204 has seen increased use

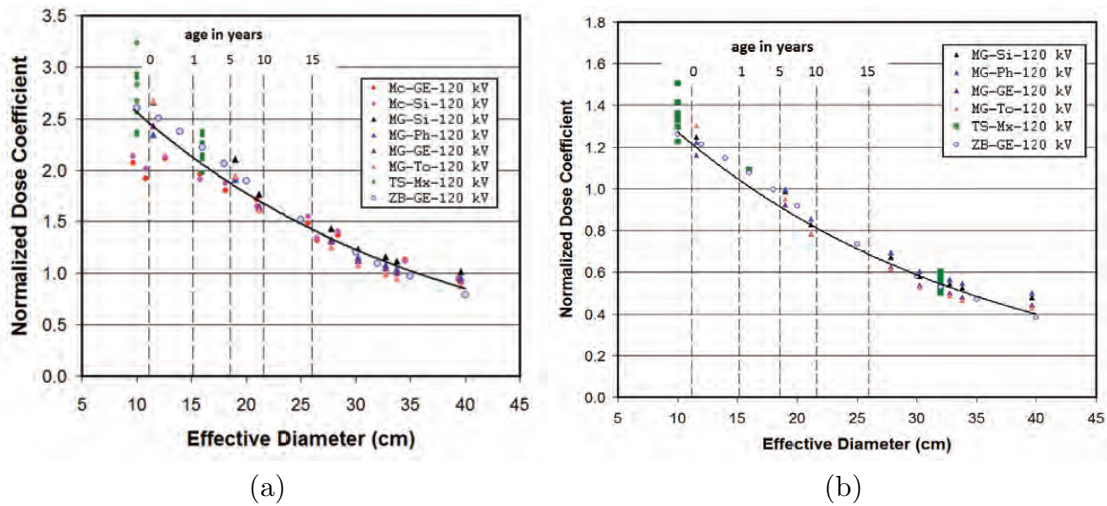


Figure 2.7: Plot of the normalized dose coefficient as a function of effective diameter (a) for a 32 cm diameter PMMA CT dose phantom, and (b) for a 16 cm diameter PMMA CT dose phantom, from AAPM report TG-204 [2011].

in the clinic [Strauss and Goske, 2011], it should be noted that there are some limitations with this method.

First, although it has the unit of Gy, the resulting SSDE is still not organ dose. As specified in Section 2.3.1.3, CTDI metrics only characterize the scanner output; although related to dose, they do not provide the dose to the patient organ or tissue. SSDE is simply a dose index that utilizes CTDI, corrected by the patient size, so that it has the same limitation as CTDI-based metrics.

Furthermore, the SSDE correction factor is based only on the outline of the patient, with no consideration of the internal anatomy information. This could be particularly problematic for special clinical procedures, such as CT Colonography, where a large amount of gas is present in the patient. Indeed, in 2012, Li and Behrman wrote a letter to the editor of Medical Physics and commented on the patient dimension determination method for pulmonary CT procedures, where large volume of low-density lung tissue is present in the chest region. In this case, using the size-specific correction factors provided in TG-204 would underestimate the dose to the patient since the mass of the patient's chest would be

much lower than the reference CT dose phantom which is made of PMMA. Based on this argument, the authors suggested caution should be taken for pulmonary CT procedures and a different size determination method should be applied to account for the density difference [Li and Behrman, 2012]. Based on our investigation of CT Colonography cases, where considerable portions of the scanned anatomy are gas, the SSDE method fails to predict the dose to the patient organs. More details will be described in Chapter 6.

Third, the longitudinal location (z location) where the size measurement should be performed is not specified in TG-204. For some patients, the dimensions measured at different z locations can vary significantly. Using the measured dimension at a single z location or taking the average of several measurements at different z locations give different results for the same patient. A potentially large uncertainty would be associated with this when different institutes or individuals apply the size-specific corrections with different z -values to determine the size-related correction factor.

2.3.3 Absorbed dose and effective dose

Two dose-related terms are commonly mentioned in the field of CT dose: the patient dose or absorbed dose, and the effective dose.

2.3.3.1 Absorbed dose measurements and calculations

Absorbed dose is a measure of the energy deposited in a medium per unit mass, and has a unit of joules per kilogram (J/kg), or Gray (Gy), milliGray (mGy). In the medical physics field, dose to an organ of interest is usually expressed as the mean organ dose, which calculates the total energy deposited in the organ divided by the total mass of the organ of interest. The mean organ dose is usually called organ dose and has a unit of Gy or mGy.

Average organ dose can be measured with small-volume dosimeters. This kind of measurement is usually done using an anthropomorphic phantom and is not practical for mea-

suring real patient doses. For example, Einstein et al. [2010] performed measurements with one to six metal oxide semiconductor field effect transistors (MOSFETs) at different locations in a Rando phantom to approximate the average dose to these measured organs. Li et al. [2011a] placed a pair of TLD chips in each organ of a Rando phantom to calculate the average organ dose and then compared the physical measurements with Monte Carlo simulated results.

The most commonly used way to calculate organ dose is Monte Carlo simulation and is considered the gold standard for organ dose determination. A review on Monte Carlo simulation for patient CT dose determination will be given in Section 2.4.

2.3.3.2 Effective dose and weighting factors

Since the potential biological effects from radiation exposure depend not only on the dose to a tissue or organ, but also on the biological sensitivity of the tissue or organ irradiated, it is important to have an indicator to account for this biological sensitivity. This is particularly important for the stochastic effects as defined in Section 2.1.2, in which the probability rather than the severity depends on the dose level. Effective dose is a parameter that reflects the risk of a non-uniform exposure in terms of an equivalent whole-body exposure. In other words, it distills the distribution of dose to various tissues and organs from a particular irradiation into a single parameter, which reflects the risk from radiation in terms of a uniform or whole-body exposure. The unit of effective dose is millisievert (mSv). Two methods have commonly been used to determine the effective dose. One is based on organ dose estimates that explicitly uses tissue-weighting coefficients as specified by the International Commission on Radiological Protection (ICRP). In this method, Monte Carlo simulations were performed on a hermaphroditic mathematical phantom, as shown in Figure 2.8. The CT scanner geometry, beam spectrum and filtration were modeled and the absorbed doses to each organ of this phantom were calculated for different CT scanners

and scan protocols. The total organ doses were summed and normalized to $CTDI_{100}$ measurements in air. The results were summarized and published by the National Radiological Protection Board (NRPB) in the United Kingdom in 1993. An updated version of these results for newer scanner types is given in the ImPACT spreadsheet, from which organ dose can be looked up based on scanner type, tube voltage and current, rotation time, and scan type [ImP]. The effective dose can then be determined by summing the products of each organ or tissue dose and the ICRP-defined tissue-weighting factors for the same organ or tissue. The effective dose can be expressed as

$$\text{Effective dose} = \sum \text{Dose}_{\text{tissue}} \times \text{Weighting factor}_{\text{tissue}}. \quad (2.6)$$

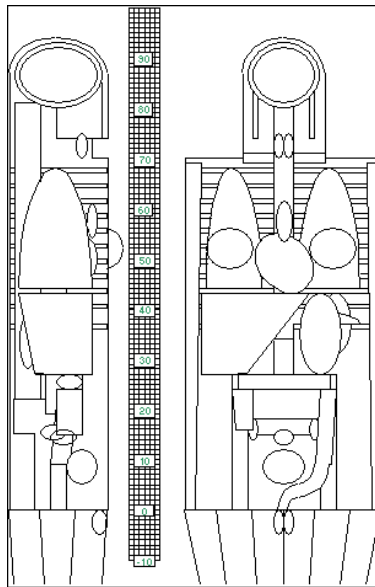


Figure 2.8: Mathematical phantom used with ImPACT spreadsheet to compute patient organ doses for CT. Picture from www.impactscan.org.

ICRP 26 [1977], ICRP 60 [1991] and ICRP 103 [2007] published the initial and updated tissue- or organ-specific weighting factors, as shown in Figure 2.9. These factors were derived from data regarding a variety of exposed cohorts that includes patients of both sexes and all ages, and depended heavily on the excess risk in survivors of the Japanese atomic bombings.

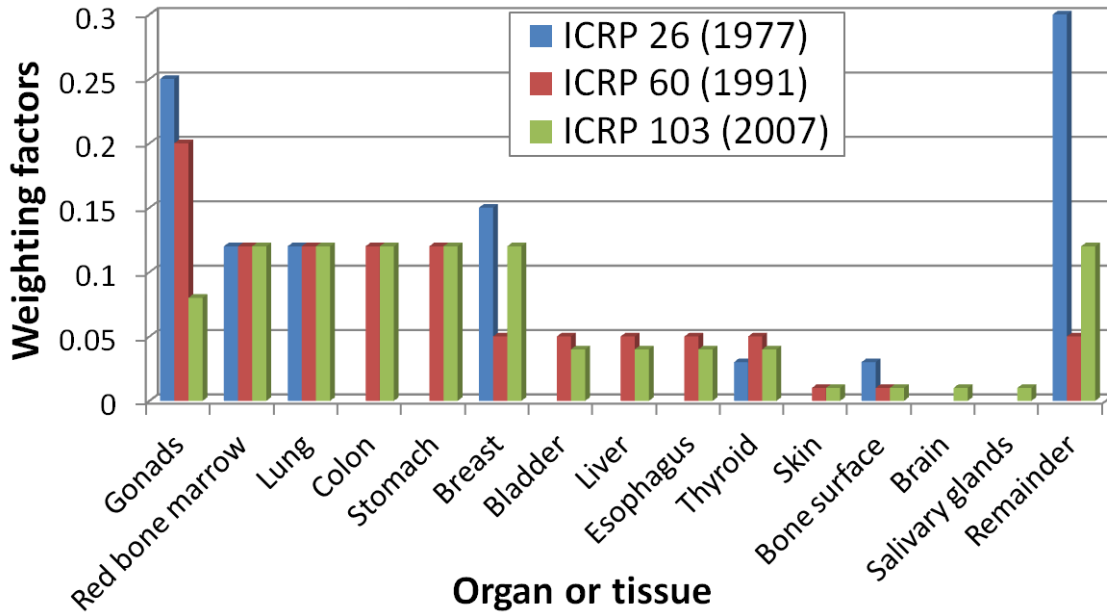


Figure 2.9: Weighting factors for different organs and tissues from ICRP publications 26 [1977], 60 [1991], and 103 [2007].

The Monte Carlo-determined organ dose is considered the gold standard for estimating effective dose. However, for CT examinations, a commonly used simplified methodology is to have a set of k coefficients, which are dependent only on the region of the body, and were determined to convert DLP values to effective dose for different organs in AAPM TG-96 [2008]. With the scan-specific DLP and the k coefficients for different organs, the effective dose can be determined by:

$$\text{Effective dose} = \text{DLP} \times k \text{ coefficients.} \quad (2.7)$$

Christner et al. [2010] summarized several available k -coefficient datasets from different groups of work, as shown in Table 2.1 . These k coefficients were based on data averaged over a large number of CT scanners and were based on a standard patient. The k coefficients were independent of patient size, age, or sex, and do not represent the dose to any individual. There have been efforts to improve the calculations of k coefficients to make them more

age, size, weight and sex specific [Huda et al., 2010, Christodoulou and Goodsitt, 2011]. Using the patient-specific information, a k factor which corresponds to the patient-specific physical parameters can be looked up and used to report the patient-specific effective dose [Jessen et al., 2000, Bongartz et al., 2004, Shrimpton et al., 2005, Jessen et al., 1999]. This is considered a possible improvement towards patient-specific dose.

2.4 Monte Carlo simulations for CT dose determination

2.4.1 Monte Carlo simulations

Due to the lack of practical ways to measure patient CT dose directly during CT scans, Monte Carlo simulation is considered one of the most accurate ways to determine radiation dose from CT scans. Monte Carlo techniques simulate all the possible interactions between the incident x-rays and the patient. With a proper model of the CT scanner and scan parameters, along with correct patient information, the dose calculation can be scan specific and patient specific. General simulation packages include MCNP [Briesmeister, 1993], EGSnrc [Kawrakow, 2000], and PENELOPE [Baróa et al., 1995] developed at different institutions. Several works have been published on CT dose calculation based on Monte Carlo simulations [Jarry et al., 2003, DeMarco et al., 2005, 2007, Li et al., 2011a]. Li et al. [2011a, 2011b] used PENELOPE to simulate patient-specific organ dose from CT scans. Gu et al. [2009] used MCNPX to simulate organ dose using a computational phantom. Some research groups also used EGSnrc [Downes et al., 2009, Caon et al., 1997] and Geant4 [Jiang and Paganetti, 2004] to perform organ dose simulations. Monte Carlo simulations of CT organ dose typically follows a common procedure for the development and validation of the source model, and the execution of the dose calculations. A typical flowchart is shown in Figure 2.10 which is taken from Gu et al.'s paper. Figure 2.11 shows a typical geometry of a CT scanner used in Monte Carlo simulations [Gu et al., 2009].

Table 2.1: Published k coefficients for effective dose calculations based on DLP.

Scan region	DLP to Effective Dose k Conversion Coefficients [mSv/(mGy \times cm)]			Phantom (cm)
	Jessen et al. (1999)	EC* (2000)	EC Appendix B (2004)	
Head	0.0021	0.0023	0.0023	16
Head and neck				16
Neck	0.0048	0.0054	0.0059	32
Chest	0.014	0.0017	0.0018	32
Abdomen	0.012	0.015	0.017	32
Pelvis	0.019	0.019	0.017	32
Chest, abdomen and pelvis			0.015	32

EC = European Commission, NRPB = National Radiological Protection Board.

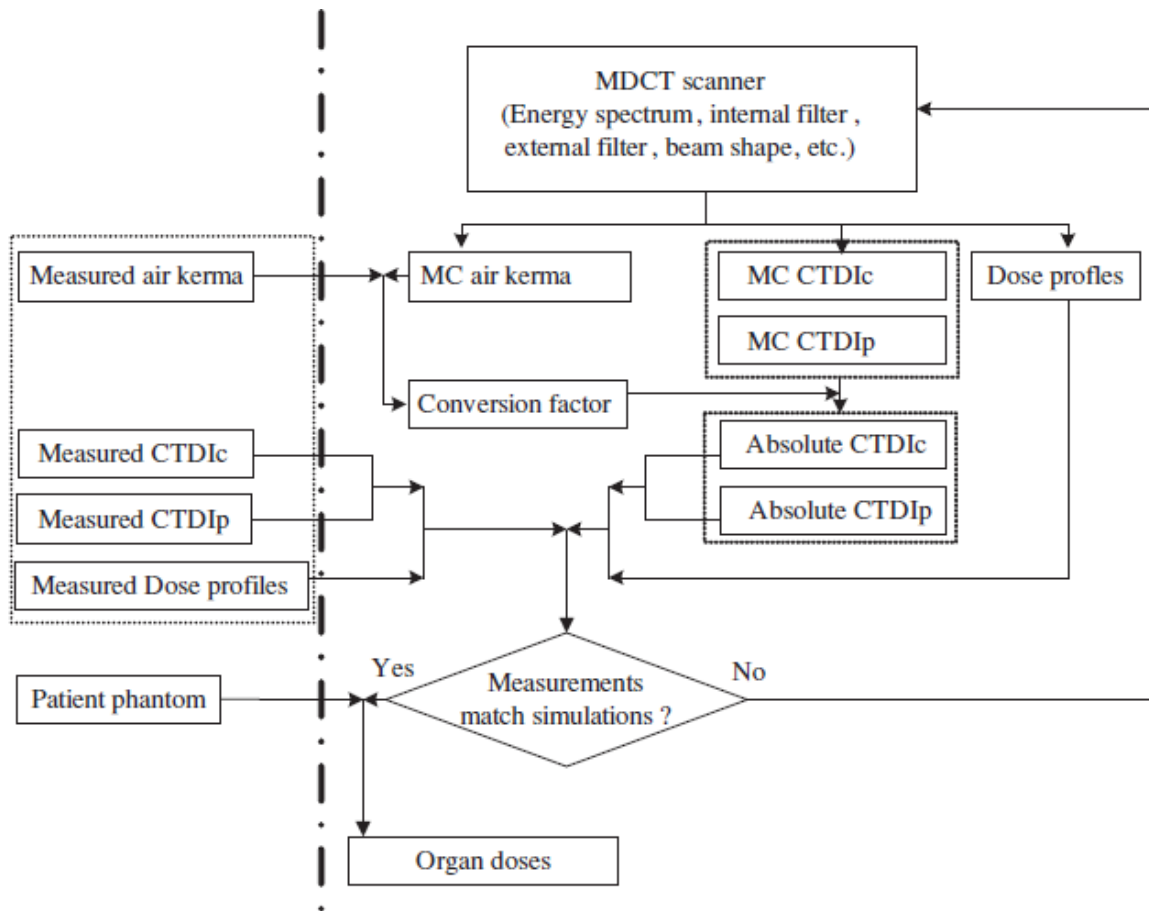


Figure 2.10: Flowchart for the development, validation and application of CT models to calculate organ dose using Monte Carlo simulations, from Gu et al. [2009].

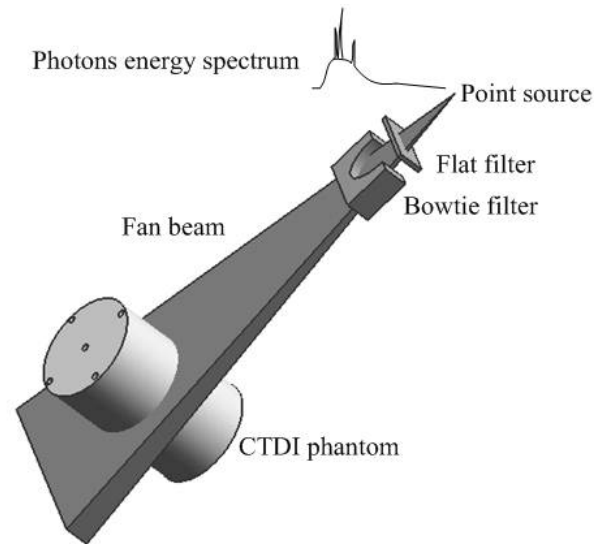


Figure 2.11: A schematic of a CT scanner model, from Gu et al. [2009].

2.4.2 Spectrum and bowtie filter determinations

2.4.2.1 CT spectrum determination

Direct CT source spectrum measurement requires substantial efforts. One reason for this is the high flux of the x rays from the CT source. When using high-efficiency detectors to measure the spectrum, the count rates are high, and pulse pile-up becomes an issue. In general, the count rates can be reduced by using collimators, low tube current or larger distance from the source. However, this is not approachable in CT spectrum measurements, due to the geometry limitations of CT gantry and the tube current settings for CT scanner. In order to determine the CT spectrum, measurement-based and model-based technologies have been investigated. For measurement-based techniques, Compton scattering spectroscopy techniques have been applied to measure the diagnostic x-ray spectra. Yaffe et al. and Matscheko et al. used a high-purity Ge detector to measure the 90-degree Compton-scattered photons that originated in the CT source, and were scattered from a

scattering object placed in the beam [Yaffe et al., 1976, Matscheko and Carlsson, 1989, Matscheko et al., 1989, Matscheko and Ribberfors, 1989]. An energy correction was applied, and the Klein-Nishina formula was used to extract the incident x-ray spectrum. A similar technique was applied by Meada et al. [Maeda et al., 2005] using a high-resolution Schottky CdTe detector. Another example of a measurement-based technique was shown by Duan et al. [Duan et al., 2011] using transmission measurements. For this type of measurement, different amounts of attenuating material were placed in the beam, and the transmitted photon signal was measured. The beam spectrum was reconstructed based on the equations that represent the attenuation processes of polychromatic x-ray photons.

Model-based methods usually generate spectra from empirical or semi-empirical physical models. The gold standard technique for x-ray tube calculations remains Monte Carlo simulations. Several analytic spectrum calculation tools have been developed to generate the x-ray spectrum for a CT scanner, including xcomp5r, TASMIP, Srs-78, Specgen T, Specgen B, and SpekCalc, which have the advantages of fast calculation speed and a user friendly interface [Gu et al., 2009].

In this work, the SpekCalc x-ray spectrum generator program developed by Poludniowski et al. [Poludniowski et al., 2009] from the Institute of Cancer Research and Royal Marsden NHS Foundation Trust in UK was used to perform CT spectrum calculations. It is free-to-download software and is based on a deterministic model of x-ray spectrum generation [Poludniowski and Evans, 2007, Poludniowski, 2007]. Figure 2.12 shows a screenshot of the Graphical User Interface (GUI) of SpekCalc. The electron energy in keV, the x-ray take-off angle and the amount of filtration can be entered into the program. Filtration can be applied for seven materials: air, water, Be, Al, Cu, Sn and W. After the spectrum is calculated, the program provides the first and second half-value layers (HVL1 and HVL2) in mm Al and mm Cu, the mean energy, and the effective energy for the calculated spectrum. The range of tube potentials can be modeled from 40 kV to 300 kV, which covers the commonly used

CT kVp. Validation of SpekCalc was performed by Moga [Moga, 2011] with a high-purity Ge x-ray spectrometry system. It was found to be accurate in the energy range of 80 kVp to 140 kVp.

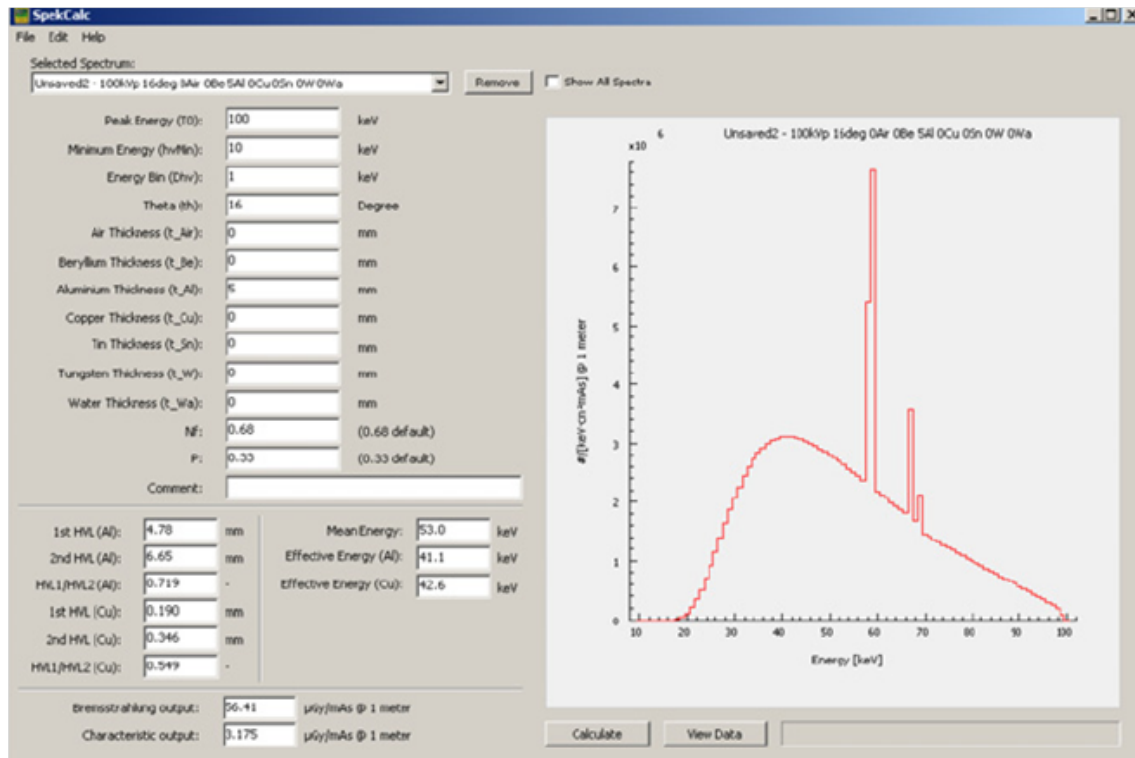


Figure 2.12: Screenshot of the SpekCalc GUI.

2.4.2.2 Bowtie filter determination

The bowtie filter is an important component in CT scanners. It is a beam shaping filter which modifies the distribution of x-ray fluence across the field of view. The bowtie filter is located after the collimated beam in a CT scanner, as shown in Figure 2.11. Ideally with the use of a bowtie filter, the fluence along the detector is equalized. Bowtie filters of earlier generations of CT scanners were typically comprised of a single compound such as Teflon (CF_2) which is approximately tissue equivalent, whereas modern CT scanners have bowtie filters with two components of metal and plastic to reduce the thickness of the bowtie filter

[Boone, 2010]. Figure 2.13 shows a photograph of a typical Teflon-made bowtie filter which has a small thickness in the center and more material on the edges [Habibzadeh et al., 2012]. The advantage of using a bowtie filter is to reduce the radiation dose to the patient and to improve the image quality, specifically in terms of contrast-to-noise ratio, scatter-to-primary ratio, CT number accuracy, and uniformity. Since the x-ray beam goes through the bowtie filter before it is incident on the patient, knowledge of the geometry and composition of the bowtie filter is necessary for an accurate Monte Carlo model of a CT scanner. However, the geometry and composition of a bowtie filter are typically not available to the CT scanner user and are proprietary information. Different groups have tried to estimate bowtie filter geometry and composition based on experimental measurements and appropriate modeling.



Figure 2.13: A photograph of a typical bowtie filter made of Teflon.

Boone proposed a method to evaluate bowtie filter geometry based on the derivation of the relative attenuation properties of a CT scanner's bowtie filter as a function of angle. The relative attenuation across the field of view can be determined from measurements made with an x-ray flux measurement probe, capable of real-time readout, placed near the edge of the field of view. Based on the simulations, the combined attenuation factors from the determined hypothetical bowtie filter matched that of the actual filter across a range of kVp to within an average of 0.057%. The author mentioned that experimental validation is needed for this theory [Boone, 2010]. In 2011, McKenney and Nosratieh et al. applied this theory for characterization of a bowtie filter using a prototype dose probe, which has the properties suggested in Boone's paper. Measurements were done in both a

custom-designed CT system and a commercial whole body CT system at at four discrete x-ray tube potentials. This work experimentally validates Boone’s theory of generating a calculation-based equivalent bowtie filter [McKenney et al., 2011].

Turner and Zhang et al. [2009] presented a method for generating x-ray source models for performing dosimetry simulations for CT scanners. This method requires the first and second half-value layers of the CT spectrum and the bowtie filter attenuation profile measurements. The bowtie filter attenuation profile measurements were performed with a CT ionization chamber. The profile measurement geometry is shown in Figure 2.14. The fact that the exposure is proportional to air kerma was utilized. For determining the effective bowtie filter, the attenuation material was arbitrarily assigned as aluminum and a central thickness of 0.5 mm was used. In Monte Carlo simulations, different amounts of aluminum at different positions within the bowtie filter was added in the model until the calculated air kerma distribution agreed with the exposure distribution measured with the ionization chamber. Using the combined effective spectrum and bowtie filter determined in this work, the average root mean square error between the measured and simulated CTDI values was approximately 5%.

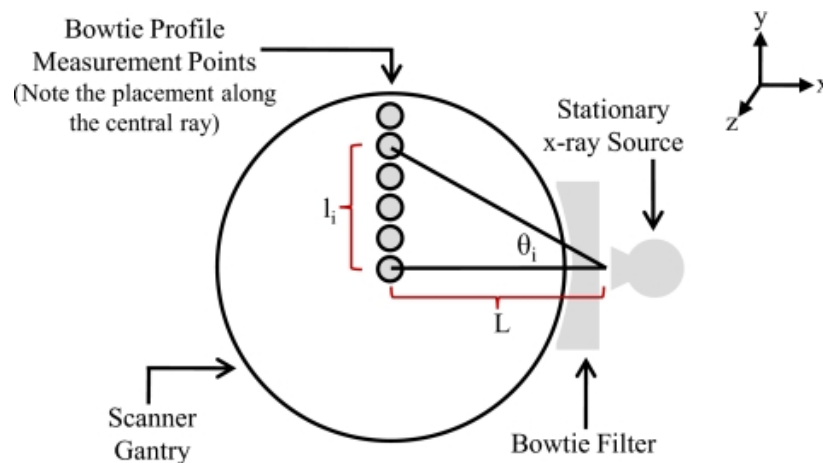


Figure 2.14: Diagram of bowtie profile measurements of attenuation across the fan beam. [Turner et al., 2009]

2.4.3 Verification of Monte Carlo simulations

For accurate dose simulations, the Monte Carlo model should always be verified. Various validation methods have been applied by different research groups who did Monte-Carlo-based CT dose calculations. In general, two categories of dose validation measurements were performed: cylindrical phantom measurements, usually using a CT dose phantom, and anthropomorphic phantom measurements with small size dosimeters. Li et al. [2011a] designed a 7-inch-diameter, 7-inch-long PMMA cylindrical phantom with seven through-holes at different locations relative to the center. An ionization chamber was inserted at each of the seven different locations, and the ratios of the peripheral doses relative to central dose were taken and compared with the Monte Carlo simulated ratio. An anthropomorphic phantom was also used in this work to further validate the Monte-Carlo-calculated doses by comparing the organ doses measured with thermoluminescent dosimeters (TLDs) inserted in the phantom and the calculated dose from Monte Carlo simulations. Zhang et al. [2009] perform central and peripheral dose profile measurements on a CT dose phantom using a Farmer-type ionization chamber and optically stimulated luminescence dosimeters (OSLs). Surface dose profiles on an anthropomorphic phantom were also measured and compared with simulated surface dose profiles.

2.5 Anthropomorphic phantoms for CT dosimetry

2.5.1 Development of phantoms for CT dose calculations

2.5.1.1 Physical phantoms

Anthropomorphic phantoms refer to physical models of the human body with appropriate anatomical structures. There are several commercially available whole body anthropomorphic phantoms including Rando[®] phantoms (The Phantom Laboratory, Salem, NY, USA), ATOM phantoms (CIRS, Norfolk, VA, USA), and adult and pediatric whole body phantoms

PBU-50, PBU-60 and PBU-70 (Kyoto Kagaku Co., Japan), etc. Photographs of these phantoms are shown in Figure 2.15. These phantoms are commonly used in radiation therapy and diagnostic fields for dose verification and image quality examinations [Li et al., 2011a, Einstein et al., 2010]. Axelsson et al. [1996] used an anthropomorphic phantom of one year old child and multiple TLDs to estimate organ doses for head exams under axial CT scans, and in the lower trunk under helical CT scans. Chapple et al. [2002] performed organ dose and effective dose estimations using the whole series of pediatric physical anthropomorphic phantoms of Varco with internally placed TLDs in a Siemens Somatom Plus 4 CT scanner of head, chest, abdomen, and pelvis examinations. These kinds of measurements provide dose to the organs of the physical phantoms and give estimates of the dose from the CT scans to patients with similar sizes.

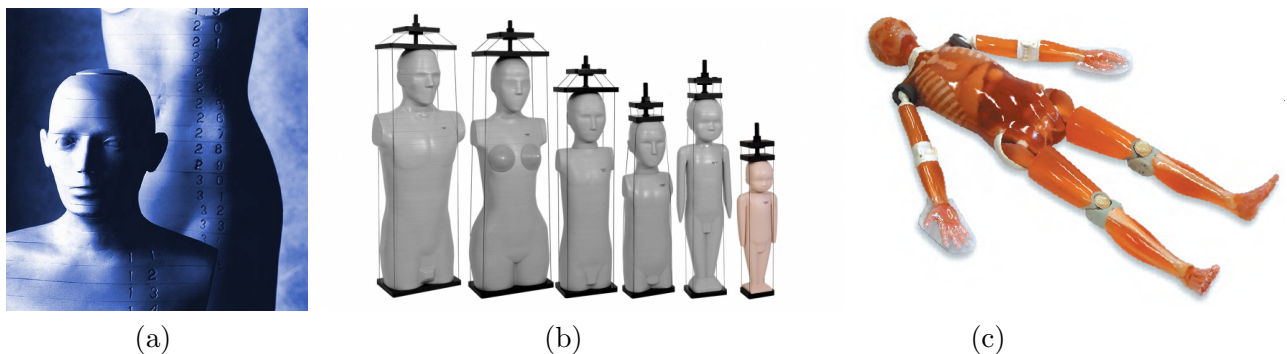


Figure 2.15: Photographs of (a) Rando phantoms[®] (The Phantom Laboratory, Salem, NY, USA), (b) ATOM phantoms (CIRS, Norfolk, VA, USA), (c) whole body phantom PBU-60 (Kyoto Kagaku Co., Japan).

2.5.1.2 Computational phantoms

In order to simulate the interactions between the incident radiation source and a patient with Monte Carlo dose calculations, a computational anthropomorphic phantom that is usable by a Monte Carlo code is necessary. This computational phantom should have accurate anatomical information, and mimic the density and chemical composition of the organs and tissues of interest. A handbook of anatomical models for radiation dosimetry was edited

by Xu and Eckerman, which provides a comprehensive review of the historical development and application of a large number of important computational phantoms that have been widely reported in the literature [Xu and Eckerman, 2009].

The first computational anthropomorphic phantom was developed in the 1960s by Fisher and Snyder [Fish and Snyder, 1966]. Simple shapes such as elliptical cylinders and cones were utilized to generate adult and pediatric phantoms with homogeneous tissue. Later on, heterogeneous phantoms with more complex geometries were developed at different institutes. The MIRD-5 phantom, developed by the Medical Internal Radiation Dosimetry (MIRD) Committee of the Society of Nuclear Medicine, represents a hermaphrodite adult (Figure 2.16 (a)). During the 1980s, Cristy and Eckerman at Oak Ridge National Laboratory (ORNL, Oak Ridge, TX) developed a phantom series that included an adult, a newborn, and individuals of ages 1, 5, 10, and 15 (Figure 2.16 (b)). This type of phantom was named “stylized phantom”, meaning only simple geometries were involved. Other stylized computational phantoms/phantom series include the ADAM and the EVA phantoms, developed by GSF, Germany representing Caucasian adult male and female human (Figure 2.16 (c)); and the KMIRD phantom representing an adult male humans developed at Hanyang University, Korea. Stylized phantoms cannot reflect the complexity of the actual human anatomy. Voxel phantoms, which were created based on CT or magnetic resonance (MR) images, can better represent the organs and tissues of the human body. The organs and tissues of interest (eg., lungs, liver, skin, etc) were identified based on the images. The density and chemical composition of these organs or tissues was assigned for each voxel. The segmented volume can then be used for Monte Carlo simulations. A family of 12 voxel phantoms was developed at GSF-National Research Center for Environment and health in Germany. Other voxel phantoms were summarized in Table 1.2 in the handbook of anatomical models for radiation dosimetry [Xu and Eckerman, 2009]. Phantoms representing a pregnant woman with her fetus at the end of 3, 6, and 9 month gestation was

developed by Xu et al, and are referred to as the Rensselaer Polytechnic Institute (RPI) Pregnant Females using BREP technique [Shi and Xu, 2004] (see Figure 2.16 (d)).

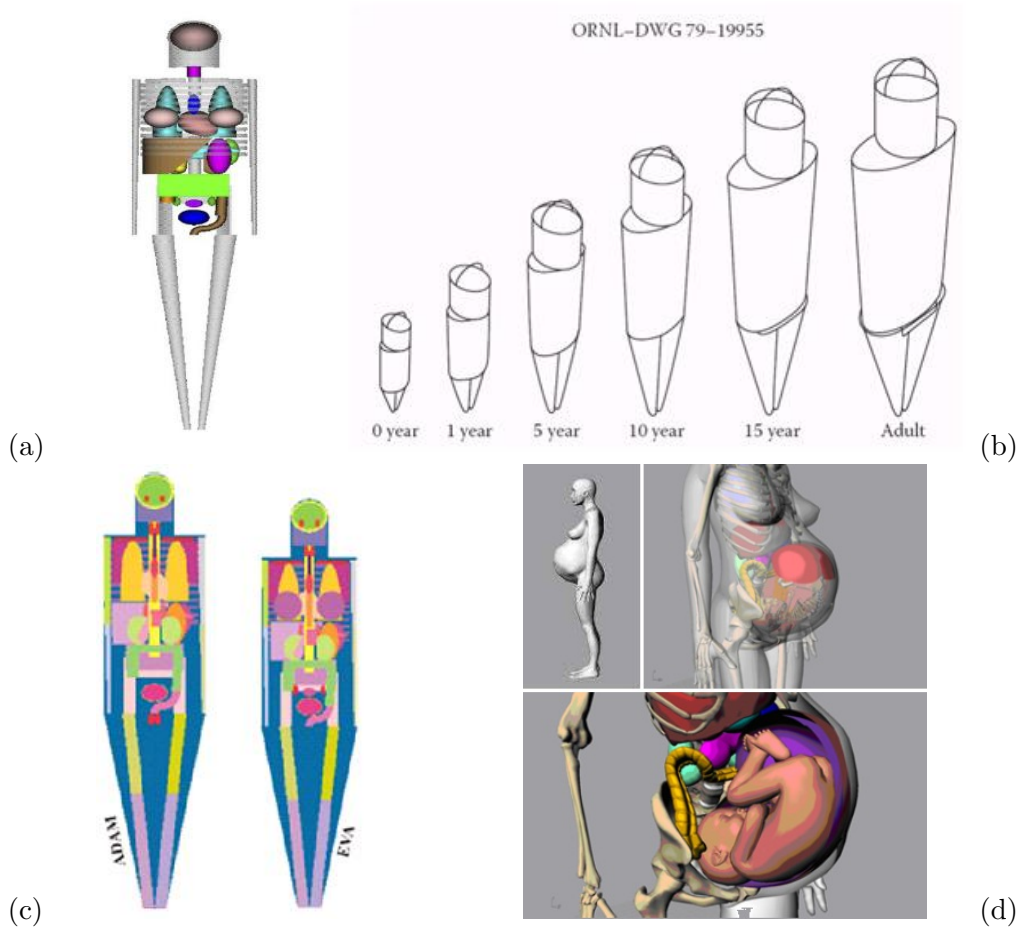


Figure 2.16: (a) MIRD-5 hermaphrodite adult phantom, (b) ORNL phantoms for different ages, (c) GSF phantoms ADAM and EVA, (d) RPI pregnant female phantom.

Several works have been reported on using computational human phantoms for CT dose calculations. Khurseed et al. utilized a series of pediatric-stylized phantoms to estimate effective dose in CT examinations [Khurseed et al., 2002]. The use of these stylized phantoms, however, can result in considerable discrepancies in organ dose, due to the unrealistic torso shape and internal organ locations [Castellano et al., 2005]. Jarry et al. published a study on the Monte Carlo method of estimating organ doses in adult patients undergoing

either axial or helical CT scans using both the adult-stylized ORNL phantom and a simple partial-body voxel phantom. Gu et al. assessed fetal and organ doses with a RPI Pregnant Females phantoms with Monte Carlo simulations [Jarry et al., 2003].

2.5.2 Limitations of using phantoms for patient-specific dose determination

With the enormous efforts from different research institutes and groups, the physical and computational human phantoms have been greatly improved and applied for CT dose measurements and simulations. For Monte-Carlo-based CT dose calculations, with the proper scanner parameters modeled, the simulations can be scan-specific. However, the calculated organ dose is only valid for the phantom being used, not a specific patient.

2.6 Project motivation and goals

The research for this dissertation is focused on the determination of patient-specific dose based on patient CT images using Monte Carlo simulations. The motivation for this work is to improve upon the current CTDI- and SSDE- based CT dose determination methods, which do not or only partially represent the dose to a patient during a CT scan. Monte Carlo simulation is the gold standard for dose calculation from radiation exposure. To perform Monte-Carlo-based dose calculations from CT scans, knowledge of Monte Carlo simulation codes and the ability to establish an accurate model for CT scanners is required. This is challenging for clinical physicists to perform since it is not part of their routine job duties, and necessary computing resources are not normally available. A secondary goal of this work is to provide a clinically applicable dosimetry package for clinical medical physicists to perform Monte-Carlo-based, patient-specific dose determinations with simple measurements of the CT scanner and patient CT images. Methodologies to determine the essential parts for CT scan modeling, including the CT source spectrum and effective bowtie

filter, are proposed in this work, which only require half-value layer measurements and the flux distribution from an air CT scan. Patient CT images are always available after the CT scan is performed, and are the best way to represent the patient-specific information, including patient size and anatomical information. Patient CT images can be loaded, and scan parameters, including a predetermined spectrum and bowtie filter, can be selected in a free program, GMctdospp with a user friendly interface. With a proper material assignment technique, an input file representing the patient-specific features and scan parameters can be established. A Monte Carlo model validation method is also presented in this work and proved to be sensitive to the beam quality. We demonstrate that with this dosimetry package, simple clinical measurements and patient CT images are sufficient for patient-specific CT dose calculations. With two clinical cases studied in this work, the feasibility of this dosimetry package for clinical application is demonstrated and the improvements on current CT dosimetry are shown.

Chapter 3

Monte Carlo dose calculations

GMctdospp, the Monte Carlo simulation program used in this work has been cross-validated. The accuracy of a CT dose simulation primarily relies on the accuracy of the characterization of a CT scanner's geometry and x-ray beam properties [Ay and Zaidi, 2005]. The characterization of a CT scanner includes the physical construction information of the CT scanner, the beam spectrum, and the bowtie filter material and geometry. In this section, the spectrum simulation and the bowtie filter determination is discussed. Since the calculated dose from a Monte Carlo simulation is normalized per starting particle, a method to determine the conversion factor to obtain doses at different mAs levels is introduced.

3.1 GMctdospp and cross-validation with MCNP5

3.1.1 GMctdospp

Some user-friendly codes that have been developed by different research groups are available for calculating CT dose, such as CT-Expo developed by Medizinische Hochschule, Germany [Stamm and Nagel, 2002], WAZA-ARI, a web-based CT dose calculation system developed in Japan [Ban et al., 2011], RADAR Medical Procedure Radiation Dose Calculator, developed by Stanford Dosimetry in the United States [RADAR]. This work uses GMctdospp,

which was developed at the University of Applied Sciences Giessen-Friedberg in Germany [Schmidt et al., 2009]. It is an EGSnrc-based Monte Carlo program for dose assessment in CT examinations. The implementation includes a graphical user interface (GUI) for simulation setup, steering of the CT scan, and analysis of results. It includes a Digital Imaging and Communications in Medicine (DICOM) loader, which can be used to import patient CT images. DICOM CT images with organ-contour information, which are usually obtained from a treatment planning system, are also supported. Simulations take full advantage of the EGSnrc physics models, while a distributed computing option (for Windows systems) and special variance reduction techniques (e.g., track-length estimators) allow efficient calculation of organ doses. Figure 3.1 shows a screen shot of the GMctdospp GUI with a calculated dose distribution.

In this work, the CT scanner-related geometry information is defined in the GMctdospp GUI including the focus-to-isocenter distance, the focus-to-detector distance, the fan angle of the beam, total collimation size (beam width), rotation angle, shift per rotation (pitch) for helical scan, number of rotations, and the location of the scan region. All this information can be defined specifically for the scanner and scan parameters used for a CT scan. Gantry/detector tilt and the over-beaming effect was kept as 0 for this work. The spectrum and bowtie filter information were predefined and used for modeling of the CT scanner. The determination methodology will be specified in Sections 3.2 and 3.3.

For a set of CT images, the material of each voxel can be determined from the CT number of this voxel. The upper and lower CT number boundaries and the upper and lower densities of a material can be defined in this program. The density gradient of this material is then obtained as

$$Gradient_{Mat} = \frac{DensityUpper_{Mat} - DensityLower_{Mat}}{CT\#Upper_{Mat} - CT\#Lower_{Mat}}, \quad (3.1)$$

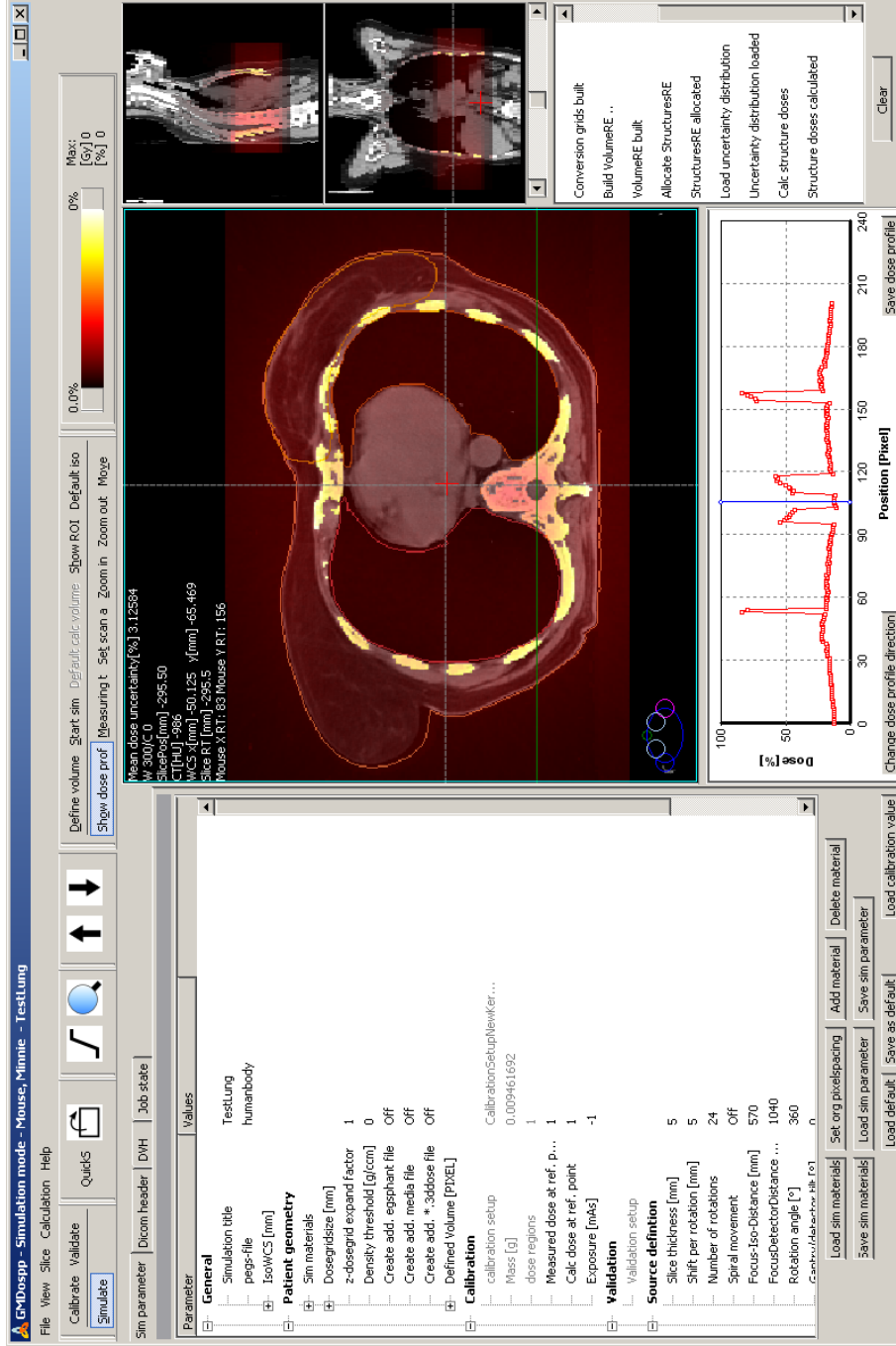


Figure 3.1: A screen shot of the GMctdospp GUI. The scan parameters can be set in the area shown on the left. The dose distribution on the transverse plane and a dose profile along a certain direction shown by the green line in the dose distribution image are demonstrated here.

where the $DensityUpper_{Mat}$ and $DensityLower_{Mat}$ are the defined upper and lower density boundaries, and $CT\#Upper_{Mat}$ and $CT\#Lower_{Mat}$ are the defined upper and lower CT number boundaries for this material. Based on the gradient, the density of each voxel is then determined by

$$Density_{Voxel,Mat} = DensityLower_{Mat} + Gradient_{Mat} \times (CT\#_{Voxel,Mat} - CT\#Lower_{Mat}). \quad (3.2)$$

PEGS (Preprocessor for EGS) file is required in this program, which includes the composition and cross sections for different materials. PEGS file and μ_{en} file including the materials of interest were predefined using the egs-gui GUI [NRC, 2009]. For dose calculations, GMctdospp scores the collision kerma per history in each voxel via a track-length estimator. Due to the fact that only low-energy photons are involved, the charged particle equilibrium can be assumed and the collision kerma can be considered equal to the absorbed dose to the medium. So the dose in each voxel is expressed as

$$D^j = K_{col}^j = \sum_i E_i t_i \left(\frac{\mu_{en}}{\rho} \right)_i / V_j, \quad (3.3)$$

where D^j and K_{col}^j are the dose and collimation kerma in the j th voxel, E_i is the energy of the i th photon, and t_i is the track-length of that photon in the voxel. The mass-energy absorption coefficient corresponding to energy E_i is $\left(\frac{\mu_{en}}{\rho} \right)_i$, and V_i is the volume of the voxel [Taylor et al., 2007].

3.1.2 Cross-validation with MCNP5

Since the EGSnrc-based user-friendly code GMctdospp is still under development, it was necessary to investigate the accuracy of this program. To achieve this goal, another commonly used Monte Carlo code, MCNP5 (version 5 of Monte Carlo N-Particle Code) [2005],

was used to perform the cross-validation. The main functions that were to test were the DICOM import and material assignment functions. Identical phantoms were defined in both GMctdospp and MCNP5 using different methods (see the following sections). A percentage depth dose curve from one view angle and a 2D dose distribution with one rotation were calculated by the two programs.

3.1.2.1 Methods and materials

To calculate dose distributions in GMctdospp, a voxelized cylindrical water phantom was generated. First, an arbitrary CT DICOM image series (with 206 slices) was loaded into Matlab (2011b, Mathworks, Natick, MA), with DICOM header information and image data stored separately. Next, the image data of each slice was replaced with a disk that had a CT number of 0 (water) inside the phantom and -1000 (air) outside of the phantom. The diameter of the disk was 256 pixels and was defined as 20 cm. The dimension of the field of view in the DICOM header was 400 mm. Since the original DICOM images had a reconstruction slice thickness of 1.25 mm, the total length of the designed water cylinder was 25.75 cm. A 120 kVp sample source spectrum provided by the GMctdospp program was used. No bowtie filter was used in any of the calculations. A 538 mm source-to-isocenter distance and 54.8896° degree fan angle were defined to match the GE Discovery CT 750 HD scanner (GE HD750 CT, GE Healthcare, Waukesha, WI) configuration, and a 20 mm collimation was defined. The depth dose curve from a single view angle and the dose distribution for a single rotation were calculated using the GMctdospp program.

For comparison, a water phantom of the same size was defined in MCNP5. The source spectrum and phantom geometry definitions were the same as the one used in GMctdospp. The depth dose curve from one view angle was simulated to represent the dose distribution. To simulate the dose distribution for a single rotation, 20 sources were situated along a single axial scan trajectory. This number of sources was demonstrated by Gu et al. [2009]

and Khurshed et al. [2002] to be sufficient to approximate the continuous axial movement of the source without significantly affecting the dose calculation results. The *F4 mesh tally was used to tally the energy fluence in each rectangular tally cell. Interpolation was used to make the dose grid identical for the GMctdospp- and MCNP5- calculated dose distributions. Both the depth dose curve and planar dose distribution were normalized to the maximum dose point within the phantom.

3.1.2.2 Results

The normalized depth dose curves calculated by GMctdospp and MCNP5 from one view angle are shown in Figure 3.2, and demonstrate good agreement. The relative planar dose distribution in axial, coronal, and sagittal views for the two methods are shown in Figures 3.3, 3.4, and 3.5. Since this work employed a cylindrical phantom, the coronal and sagittal planar dose distributions are essentially the same. The accuracy of GMctdospp was cross-validated by MCNP5 and good agreement between these two methods is shown here.

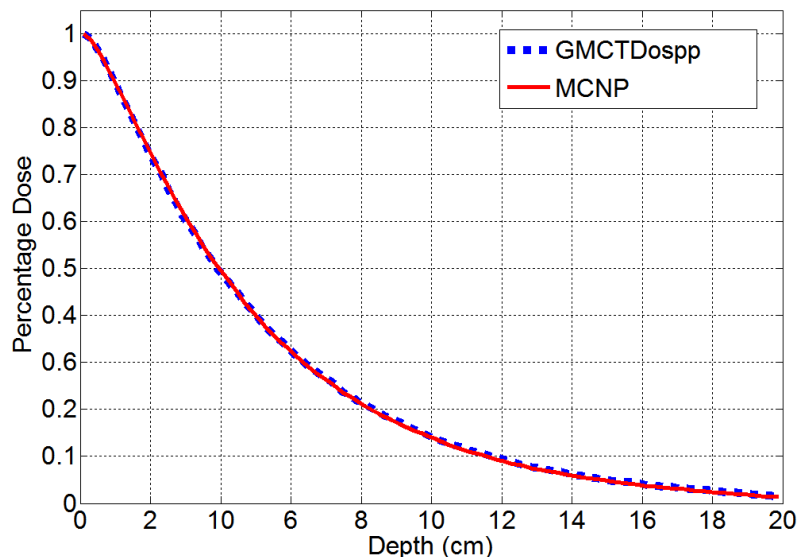


Figure 3.2: Depth dose profile along the central axis at different distances from the phantom surface.

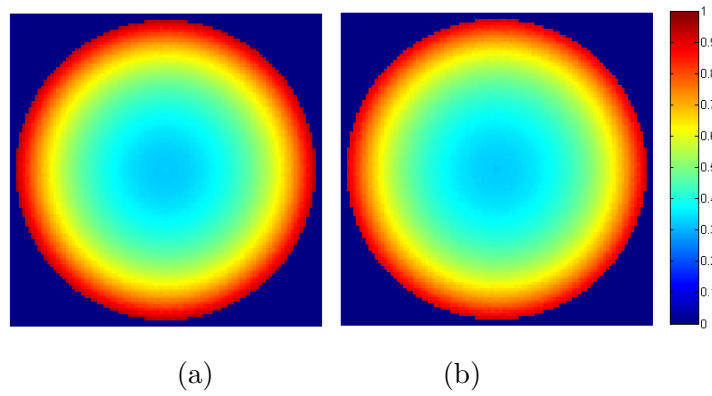


Figure 3.3: Axial planar dose distribution: (a) GMctdospp and (b) MCNP5.

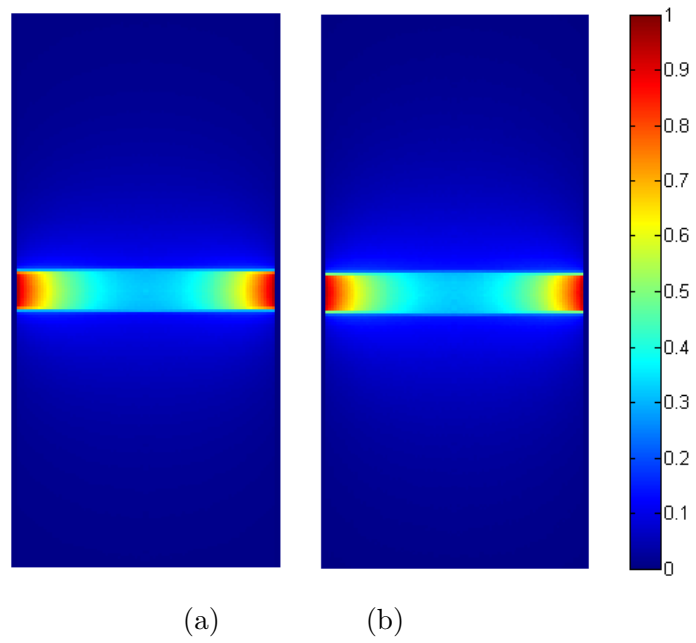


Figure 3.5: Sagittal planar dose distributions: (a) GMctdospp and (b) MCNP5.

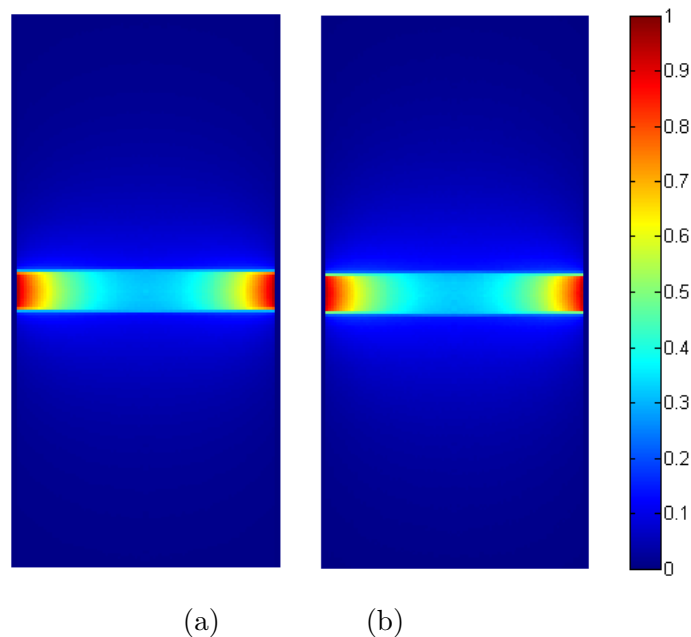


Figure 3.4: Coronal planar dose distributions: (a) GMctdospp and (b) MCNP5.

3.2 Spectrum determination

3.2.1 Methods and materials

3.2.1.1 Spectrum determination methodology

As described in Section 2.4.2.1, SpekCalc, which has been verified by Moga [2011], was used for determination of the CT source spectrum. In this work, the GE HD750 CT spectrum for a large body scan protocol was investigated. The GE HD750 CT manual-stated filtration is 1.998 mm C (graphite) and 4.7 mm Al. Since C is not included in SpekCalc, another element, Be was used instead since the atomic number of Be is close to that of C. This information was used to get the initial spectrum. The first and second Half-value layers (HVL1 and HVL2) were determined using GMctdospp. An original exposure was represented by the dose to air at the isocenter from one view angle without adding any filtration to the beam. Different amounts of aluminum attenuation were added at 1 cm from

the source until the exposure (dose to air) at the isocenter was half and a quarter of the original exposure. HVL1 and HVL2 were also measured on the CT scanner. Discrepancies between the measured HVL1 and HVL2 and the Monte-Carlo-simulated HVL1 and HVL2 based on this initial spectrum matching the filtration in the scanner manual was found. Adjustment of the filtration information was performed until the Monte-Carlo-simulated HVL1 and HVL2 using the adjusted spectrum matched the measured HVL1 and HVL2. This workflow is shown in Figure 3.6.

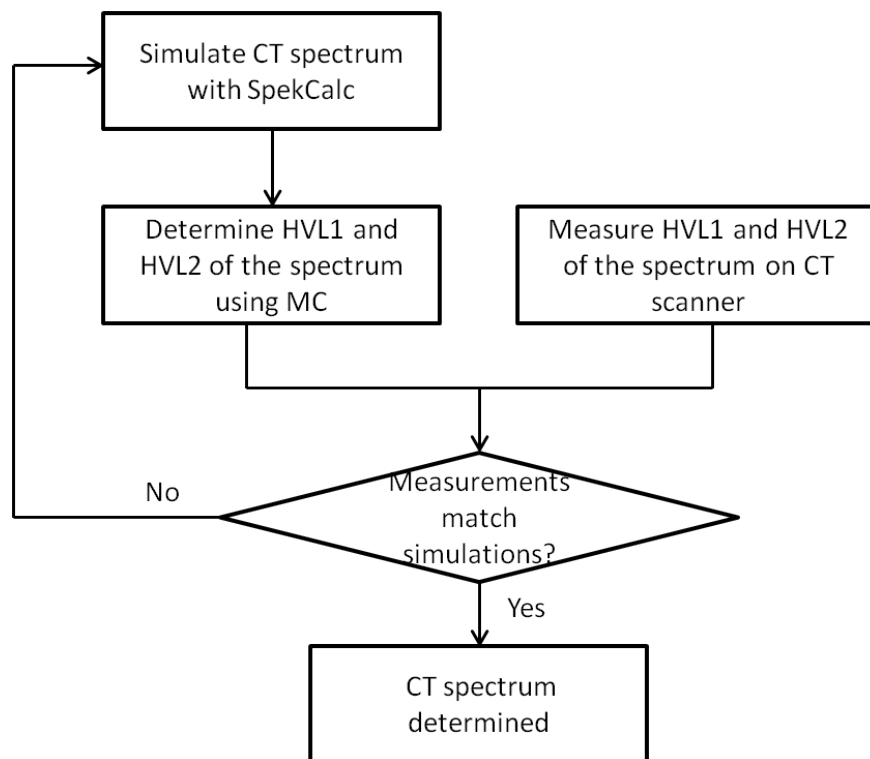


Figure 3.6: Workflow for spectrum determination in this work.

3.2.1.2 Calibration of ionization chamber

For half-value layer (HVL) measurements, a Capintec PS-033 thin-window parallel plate ionization chamber (Capintec Inc., NJ) was used. It has a 0.5 cm^3 active volume, 1.6 cm active volume diameter, and 2 cm cavity diameter. This chamber was mounted in an air-

equivalent plastic block. To minimize the scatter from the gantry and table of the CT scanner, a piece of thin lead foil was taped on the back and sides of the plastic block. Figure 3.7 shows the photograph of the front and back of the Capintec PS-033 ionization chamber with the lead foil on it.

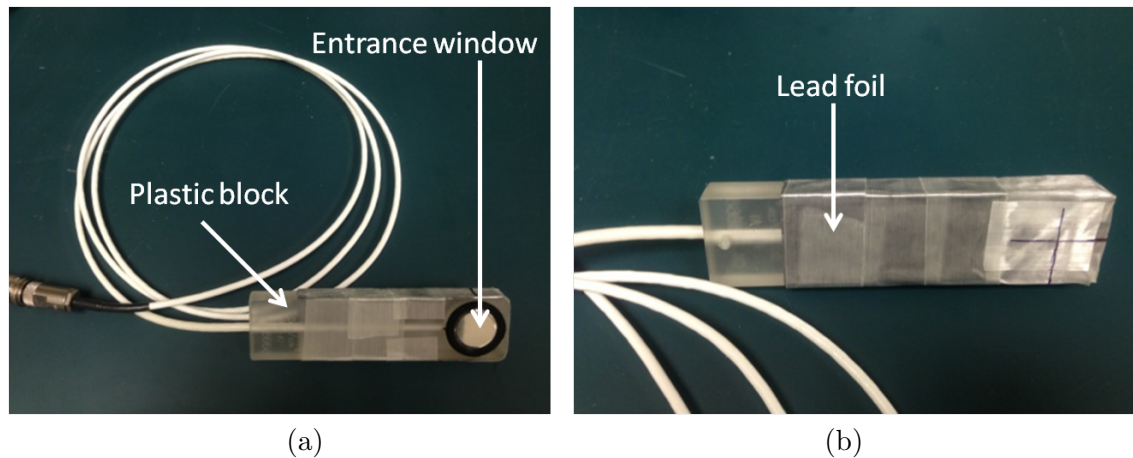


Figure 3.7: Photograph of Capintec PS-033 ionization chamber used in this work: (a) front, (b) back.

The air-kerma calibration of this ionization chamber was performed on a constant potential x-ray system with a Gulmay CP 320 generator and a COMET 320/26 tungsten anode tube at University of Wisconsin Accredited Dosimetry Calibration Laboratory (UWADCL). With the presence of attenuation material when performing HVL measurements, the beam spectrum changes, so it was necessary to test the chamber response for different filtered beams. To investigate the energy dependence of this ionization chamber, four different beam qualities were used to perform the calibration: UW100-M, UW120-M, UW150-M, and UW250-M, which match the HVL1s and HVL2s of M100, M120, M150 and M250 beams at the National Institute of Standards and Technology (NIST). The kVp, effective energies, HVL1s and HVL2s of these four beams are shown in Table 3.1. A NIST-calibrated reference-class ionization chamber was used to get the chamber reading, $R_{dg_{NIST, BQ_i}}$, in nC, for the beam quality BQ_i . The reading from the PS-033 chamber using the same beam,

was recorded as Rdg_{PS-033,BQ_i} in nC. The air-kerma calibration coefficient, N_k for a certain beam quality can be expressed as

$$N_{k,PS-033,BQ_i} = N_{k,NIST,BQ_i} \times \frac{Rdg_{PS-033,BQ_i}}{Rdg_{NIST,BQ_i}}. \quad (3.4)$$

In this equation, the N_k for both the NIST-calibrated ionization chamber and the PS-033 chamber has units of cGy/nC. At UWADCL, the NIST-calibrated ionization chamber is an Exradin A3 ionization chamber (Standard Imaging, Middleton, WI). All measurements were corrected to standard temperature and pressure, and for the electrometer calibration coefficient.

3.2.1.3 HVL measurements

The HVL measurements were performed on a GE HD750 CT scanner (GE Healthcare, Waukesha, WI) at the University of Wisconsin Imaging Center. The “Scout” scan mode, which is used prior to CT scans for providing landmarks for CT scan ranges, was used to perform the measurements. Under Scout scan mode, a large-body bowtie filter is in the beam and the source can be parked at different locations. For HVL measurements, the source was parked at 6 O’clock position in the gantry, and a beam width of 20 mm was used. The entrance window of the shielded PS-033 ionization chamber was placed at the isocenter of the system using the lasers as shown in Figure 3.8. The couch was fully retracted and the chamber was held from a stand on the other side of the gantry. A PMMA holder for the attenuators was placed on the gantry close to the source. To make sure the beam was going through the attenuation material perpendicularly, a bubble level was used to verify that the holder was level. Aluminum filters of 0.999 purity made by PTW (Freiburg, Germany) with different thicknesses were used as the attenuation material. The thinnest piece had a thickness of 0.1 mm.

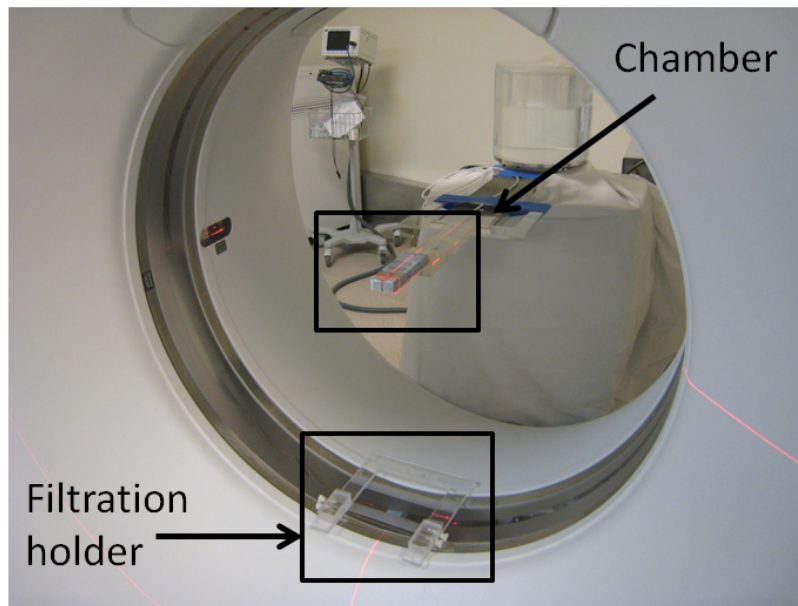


Figure 3.8: Photograph of the HVL measurement setup.

A Max 4000 electrometer (Standard Imaging, Middleton, WI) was used and a +300 V bias was applied to the ionization chamber. The original chamber reading was obtained without any filtration material in the beam. Different amounts of aluminum filters were added in the beam until the chamber reading decreased by a factor of 2 for HVL1. Additional attenuation material was added until the chamber reading was further reduced by half to get the HVL2.

3.2.2 Results

3.2.2.1 Energy response of ionization chamber

The kV_p, HVL1, HVL2 and air-kerma calibration coefficients, N_k of the PS-033 ionization chamber for the four beam qualities are shown in Table 3.1. The largest discrepancy in the N_k among the four beams was 1.72% (between UW150-M and UW250-M). Since a relative flat response for different beam qualities was shown for the PS-033 ionization chamber, an energy dependence correction was not considered necessary for this work.

Table 3.1: kVp, HVL1, HVL2 and air-kerma calibration coefficients N_k for PS-033 ionization chamber for four beams at the UWADCL.

Beam codes	kVp	HVL1 (mm Al)	HVL2 (mm Al)	N_k (Gy/C)
UW-100M	100	4.98	6.92	5.175×10^7
UW-120M	120	6.96	8.92	5.091×10^7
UW-150M	150	14.9	17.1	5.010×10^7
UW-250M	250	18.5	18.9	5.185×10^7

3.2.2.2 Half-value layer of CT beam

The measured HVL1 and HVL2 for the GE HD750 CT scanner using a large-body scan protocol are 7.8 mm Al and 10.0 mm Al, respectively. In the scanner's manual, the HVL1 is specified as 7.7 mm. Thus, the measured HVL1 agrees well with the manufacturer specified value. The uncertainty associated with HVL measurements was determined as ratio of the thinnest thickness of Al filter (0.1 mm) and the measured HVL (7.8 mm), which is 1.28%.

3.2.2.3 Spectrum of CT beam

After matching the measured and simulated HVL1 and HVL2, the GE HD750 large-body spectrum was determined as shown in Figure 3.9. 120 kVp was used for this spectrum, which is typical for adult body scans. This spectrum was used for the source modeling in the Monte Carlo simulations in this work.

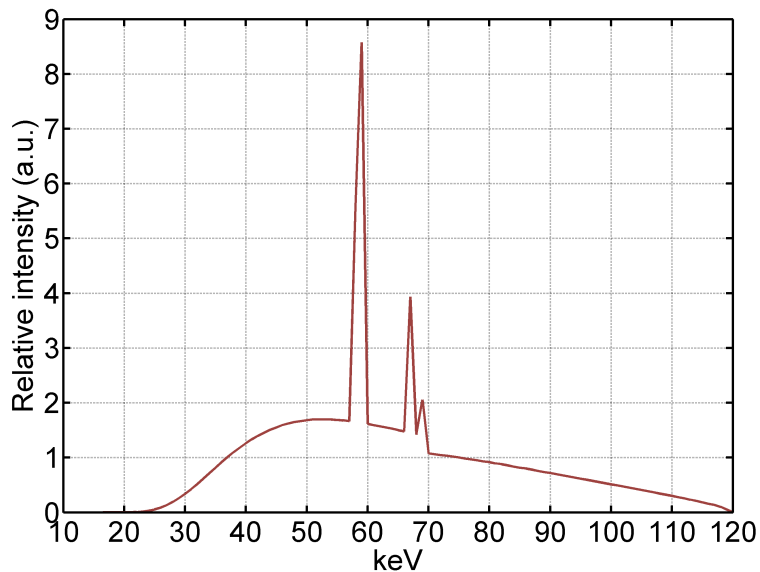


Figure 3.9: Determined large body spectrum of the GE HD750 CT scanner using 120 kVp.

3.3 Bowtie filter determination

3.3.1 Flux distribution measurements on a CT scanner

The photon fluence distribution on the detector was determined using an air scan on a GE HD750 CT scanner (GE Healthcare, WI) at the University of Wisconsin Imaging Center. No object was present and the couch was fully retracted to be outside of the field of view. A large-body scan protocol was applied with 120 kVp and a large-body bowtie filter in the beam. The mA was set to 100 mA. One rotation was performed with a rotation speed of 1 s/rotation. After the scan was performed, the 2D flux distribution within the fan angle (the range of the x-ray beam within $x - y$ plane of a CT system, 55° for GE HD750 CT scanner) from each projection angle was obtained from the scanner. A total of 984 projection angles were performed within one single rotation for GE HD750 scanner and the averaged flux distribution of the 984 projection angles was used as the measured flux distribution in this work.

3.3.2 Flux distribution using Monte Carlo simulations

Flux distribution was simulated using GMctdospp Monte Carlo simulation program. A set of DICOM images with air only (CT number of -1000) was imported for dose calculations. The source spectrum determined in Section 3.2 was used in the input file. This determined spectrum represents a multienergetic beam. However, for flux distribution simulations, a linear relationship between air kerma and photon flux was assumed in this work, which indeed is only valid for monoenergetic beam. Based on this assumption, the flux distributions with and without a bowtie filter were simulated by scoring the air kerma at the detector locations.

The source-to-isocenter distance and the source-to-detector distance are specified as 54 cm and 95 cm, respectively in the GE HD 750 CT scanner manual. Instead of modeling a full rotation, one projection was modeled. The flux distribution at 41 cm from the isocenter within the $x - y$ plane within the fan angle was obtained from the calculated 3D air kerma distribution.

3.3.3 Methodology to determine bowtie filter

A methodology similar to that of Boone [2010] and Turner and Zhang et al. [2009] (reviewed in Section 2.4.2) was used to determine a bowtie filter geometry and composition that had the same beam-shaping effect along the detector direction (within the fan beam) as the one in the CT scanner. In other words, with the determined bowtie filter in the Monte Carlo model, the simulated post-bowtie-filter flux distribution should be equal to the measured flux distribution. Because the geometry and composition of the modeled bowtie filter may not be equal to the actual bowtie filter, it should be referred to as an “effective bowtie filter” or “estimated bowtie filter”.

To perform the bowtie filter determination, the workflow in Figure 3.10 was applied. Some details regarding this workflow will be discussed in the following sections.

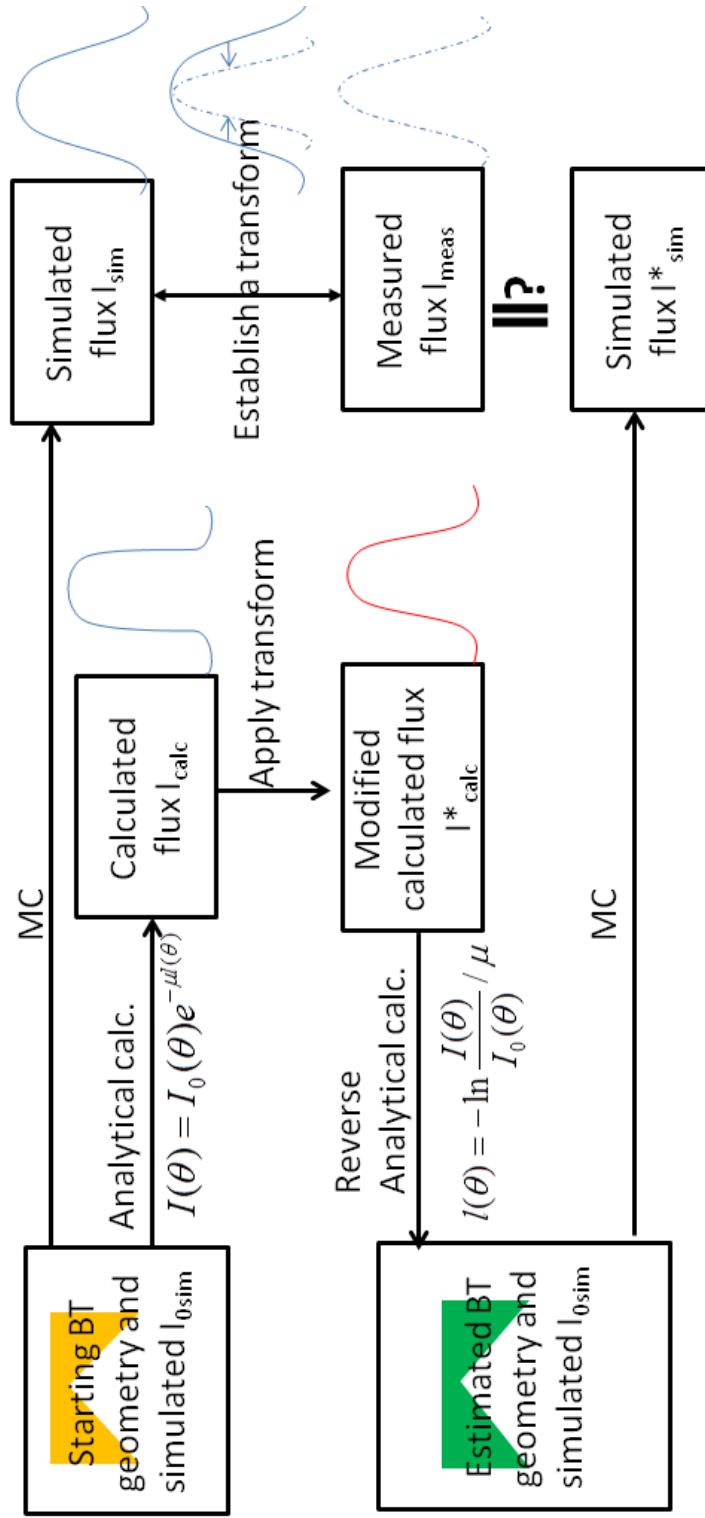


Figure 3.10: Workflow to determine the effective bowtie filter. “BT” stands for bowtie filter, and “MC” stands for Monte Carlo.

3.3.3.1 Analytical calculations

Figure 3.11 shows a not-to-scale CT scanner configuration with the bowtie filter in the beam. In this work, it was assumed that the bowtie filter was composed solely of Teflon. Other assumptions include a 12 mm distance from the source (L_0 in Figure 3.11), and a 1.6 mm central thickness. The bowtie filter geometry from GMctdospp was used for the initial model, or starting bowtie in Figure 3.10. At any fan angle θ , the detected flux at the detector when the beam does not go through a bowtie filter is expressed as $I_0(\theta)$. With the bowtie filter present, the detected flux at the same point on the detector depends on the amount of material the beam goes. The amount of material $l(\theta)$ is a function of fan angle θ and can be determined with a known bowtie geometry. The detected flux $I(\theta)$ can then be expressed as

$$I(\theta) = I_0(\theta) e^{-\mu l(\theta)}, \quad (3.5)$$

where μ is the linear attenuation of the filtration material, Teflon in this case.

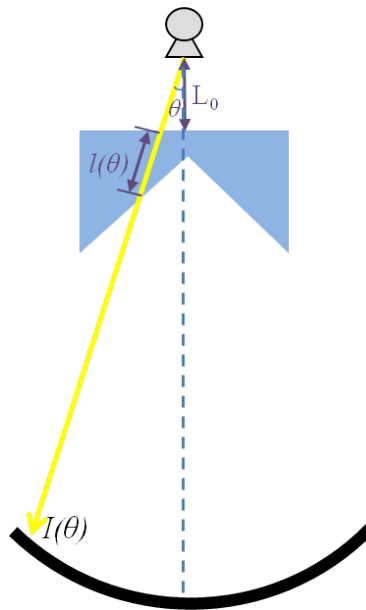


Figure 3.11: Not-to-scale drawing of a CT scanner configuration with bowtie filter in the beam.

Using the same relationship as shown in Equation 3.5, if the flux distributions on the detector both with and without bowtie filter in the beam are known, a reverse analytical calculation can be performed according to Equations 3.6 and 3.7. With the $l(\theta)$ distribution determined, the bowtie filter geometry is also determined.

$$\ln \frac{I(\theta)}{I_0(\theta)} = -\mu l(\theta), \quad (3.6)$$

$$l(\theta) = -\ln \frac{I(\theta)}{I_0(\theta)} / \mu. \quad (3.7)$$

3.3.3.2 Scatter correction

A flux distribution along the fan angle at the detector, $I_{0\text{sim}}$, was simulated using GMctdospp with the absence of the bowtie filter in the model. Using this flux distribution $I_{0\text{sim}}$, the calculated post-bowtie-filter flux distribution along fan angle on the detector, I_{calc} , using

the analytical calculation Equation 3.5 based on the starting bowtie filter was found as shown by the blue line in Figure 3.12. Monte Carlo simulation with the starting bowtie filter in the model was also performed to obtain the flux distribution along the fan angle at the detector, I_{sim} , and the result is shown as the red line in Figure 3.12. It is seen that disagreement exists between the analytical calculations and Monte Carlo simulations. The reason for this disagreement is that the scatter effect was not considered in the analytical calculations and thus, corrections were required.

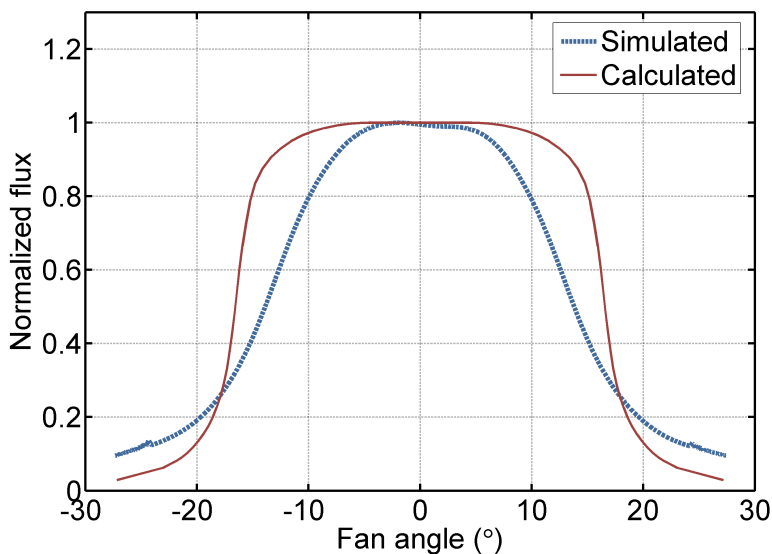


Figure 3.12: Comparison of flux distribution between analytical calculations and Monte Carlo simulations using the starting bowtie geometry.

The goal for bowtie filter determination is to get the simulated post-bowtie-filter flux distribution, I_{sim} , to match the one measured on the CT scanner I_{meas} . The results in Figure 3.11 shows that the shape of bowtie filter cannot be directly obtained from I_{meas} based on analytical calculations because the scatter effect was not included. To achieve the goal for effective bowtie filter determination and to minimize the discrepancy between the measured and simulated flux distribution, a transform between I_{sim} and I_{meas} was established by applying a correction matrix on the simulated flux. This matrix was then

applied to the analytical calculated flux distribution I_{calc} to get an intermediate term, I_{calc}^* . Reverse analytical calculations as shown in Equation 3.7 were used to get an estimated bowtie filter geometry. With this geometry, Monte Carlo simulations were performed to get I_{sim}^* , and a comparison was made between I_{sim}^* and I_{meas} . If good agreement was found, the bowtie filter geometry was determined, and if not, the transform matrix was modified until good agreement was shown between I_{sim}^* and I_{meas} . This process is shown in Figure 3.10.

3.3.4 Results

3.3.4.1 Bowtie filter geometry

After several iterations of modifying the bowtie-filter geometry following the methodology in this work, the final large-body bowtie filter geometry using this methodology is shown in Figure 3.13. This is an EGSnrc rendering of the bowtie filter.

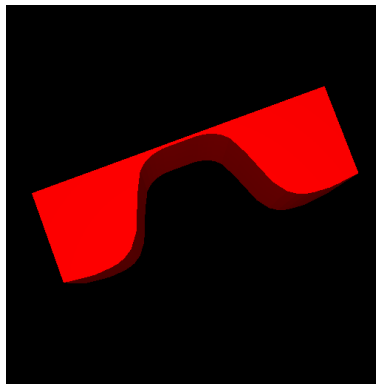


Figure 3.13: EGSnrc rendering of the determined large-body bowtie filter shape.

3.3.4.2 Comparison of simulated-flux and measured-flux

Figure 3.14 shows the comparison of the measured photon flux along the fan angle and the simulated post-bowtie-filter flux after the determined large-body bowtie filter was added to the Monte Carlo simulation model. The fan angle was 55° . The noise shown in the measured flux distribution is primarily from the gain factor variation of the detector elements, and

no smoothing was performed. Both of the flux distributions were normalized to the largest value within the fan angle. The difference (absolute value) between the measurement and simulation at each fan angle was calculated. The average difference between the measurement and the simulation within in the 55° fan angle was 5.8% and good agreement is shown here.

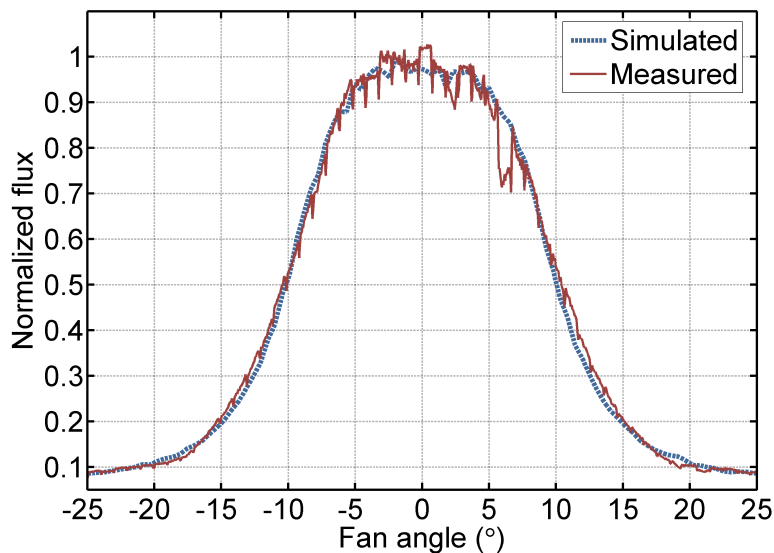


Figure 3.14: Comparison between the simulated and measured post-bowtie-filter flux distributions.

3.4 Determination of mAs-to-dose conversion factor

3.4.1 Methodology to determine mAs-to-dose conversion factor

The calculated dose from Monte Carlo simulations is given by dose per starting particle with the unit of mGy/particle. The dose to a patient from a CT scan is related to the spectrum and bowtie filter, the collimation setting, the pitch for the helical scan and the mAs. All this information can be simulated in Monte Carlo, except for the mAs, which is the product of tube current, mA, and time per rotation, s. To determine the dose to

the patient, a mAs-to-dose conversion factor is needed to convert dose per starting particle to dose at a certain mAs value. To determine this mAs-to-dose conversion factor, the methodology of Li et al. using an ionization chamber as was used [Li et al., 2011a]. Monte Carlo simulated dose per particle in the active volume of an ionization chamber can be determined as d_{sim} . Dose measurement with an ionization chamber at a scanner output of X mAs can be performed to obtain d_{meas} , with a unit of mGy/mAs. The ratio of these two items is the determined mAs-to-dose conversion factor (Equation 3.8). With a dose distribution per particle simulated in a Monte Carlo program, the determined mAs-to-dose conversion factor can be applied and multiplied by mAs to get dose distribution with the unit of mGy.

$$\text{mAs-to-dose conversion factor} = \frac{d_{\text{meas}}[\text{mGy/mAs}]}{d_{\text{sim}}}. \quad (3.8)$$

3.4.2 Linearity test of dose and mAs

The methodology to determine the mAs-to-dose conversion factor assumes a linear relationship between dose to the patient and mAs (scanner output). The linearity between measured dose and mAs should be discussed. An ionization chamber can be used to measure the dose delivered to a phantom. Different mAs values can be set on the CT console to test the linearity of the scanner output. In fact, both in-phantom measurement and in-air measurement are valid for this purpose. In this work, in-phantom measurements were performed.

3.4.2.1 Methods and materials

An Exradin A101 CT ionization chamber and Max-4000 electrometer (Standard Imaging, Middleton, WI) were used to perform the linearity test. This was a regular output check for CT scanner quality assurance. The ionization chamber was placed in the insert of a

head CT dose phantom, as shown in Figure 3.15. The CT scan was performed on a GE HD750 scanner. A chest scan protocol was used and the beam width was selected to be 40 mm. The table was kept stable and one rotation was performed with the rotation speed of 0.5 s/rotation. Different mA settings were chosen from 50 mA to 300 mA.

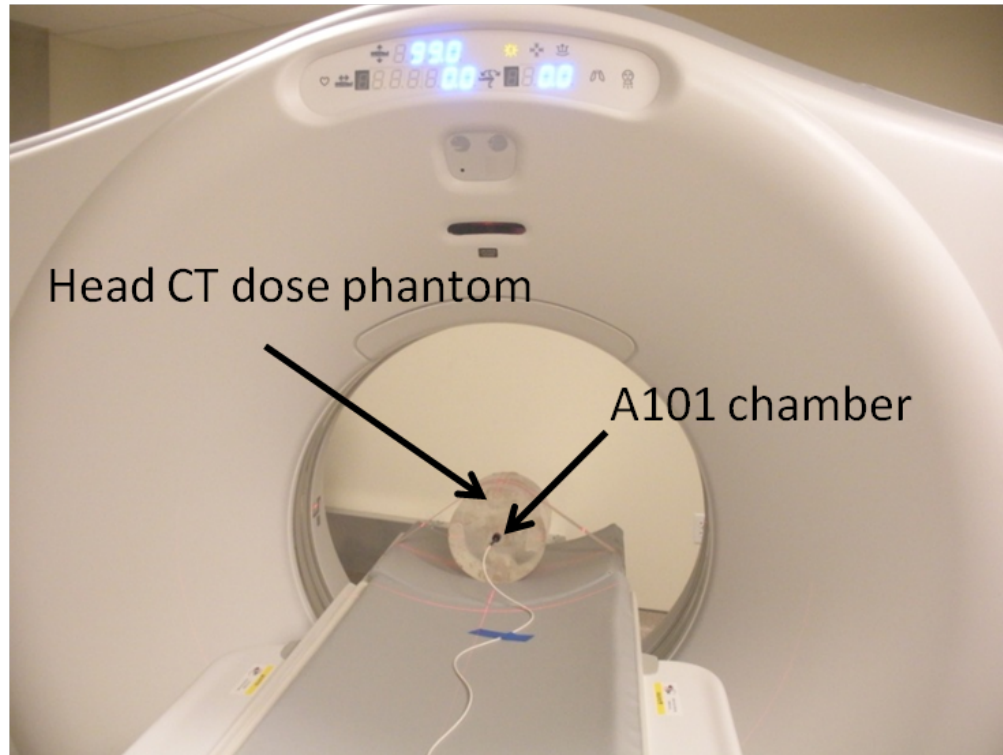


Figure 3.15: Photograph of linearity test setup. The Exradin A101 ionization chambers was placed in the central insert of the head CT dose phantom.

3.4.2.2 Results

The relationship between the ionization chamber readings and different mAs settings is shown in Figure 3.16. The coefficient of determination R^2 was 0.99998, which indicates a good linearity of scanner output to mAs.

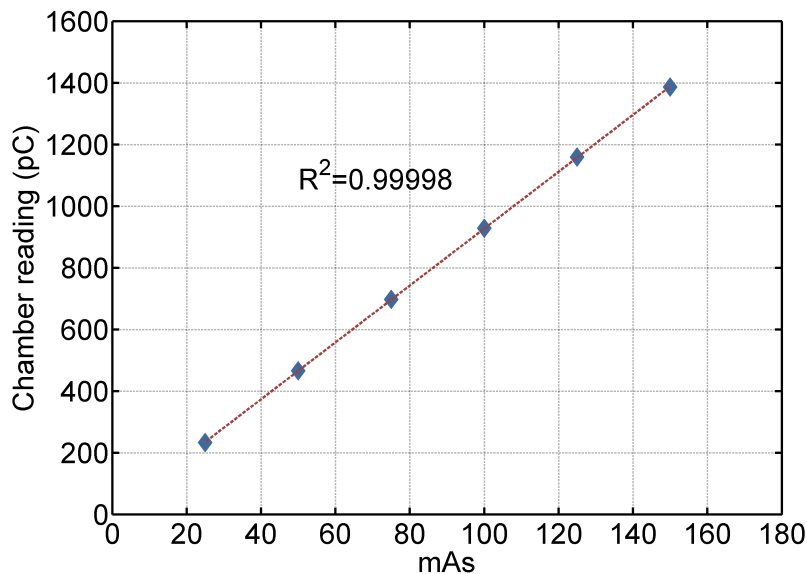


Figure 3.16: The relationship between the ionization chamber readings and different mAs settings.

3.4.3 A1SL ionization chamber modeling and in-air measurement

3.4.3.1 A1SL ionization chamber calibrations

In this work, to determine the mAs-to-dose conversion factor, an Exradin A1SL ionization chamber (Standard Imaging, Middleton, WI) with a 0.057 cm^3 active volume was used. The A1SL ionization chamber was calibrated on both the UW-120M beam and UW-RQT9 beam at UWADCL. Both of the beams have 120 kVp. The HVLs of these two beams are 6.92 mm Al and 8.37 mm Al, respectively. The HVL of the CT large-body post-bowtie-filter spectrum was determined to be 7.8 mm Al (see Section 3.2.2.2). For the A1SL ionization chamber used in this work (S/N XW090634), the air kerma calibration coefficients for UW120-M and UW-RQT9 beams were $4.991 \times 10^8 \text{ Gy/C}$ and $5.000 \times 10^8 \text{ Gy/C}$. A difference of 0.18% between these two calibration coefficients shows a flat response for different beam qualities of this A1SL ionization chamber. Interpolation between the air kerma calibration coefficients from the two beams based on the HVLs was performed and $4.996 \times 10^8 \text{ Gy/C}$

was used as the calibration factor for the CT beam to get the measured air-kerma value, or dose to the air within the active volume of the ionization chamber.

3.4.3.2 Measurements

An in-air scan of the Exradin A1SL ionization chamber was performed on the GE HD 750 CT scanner using the setup shown in Figure 3.17. The center of the active volume was aligned at the isocenter of the CT scanner using the lasers on the CT scanner. The large-body spectrum and large-body bowtie-filter were used for this scan. The beam width was set to be 40 mm and one rotation (1 s/rotation) was performed with the couch fully retracted and stationary. 300 mA was used in this scan. d_{meas} was obtained by applying the calibration coefficient and temperature-pressure correction to the raw chamber readings (with units of C).

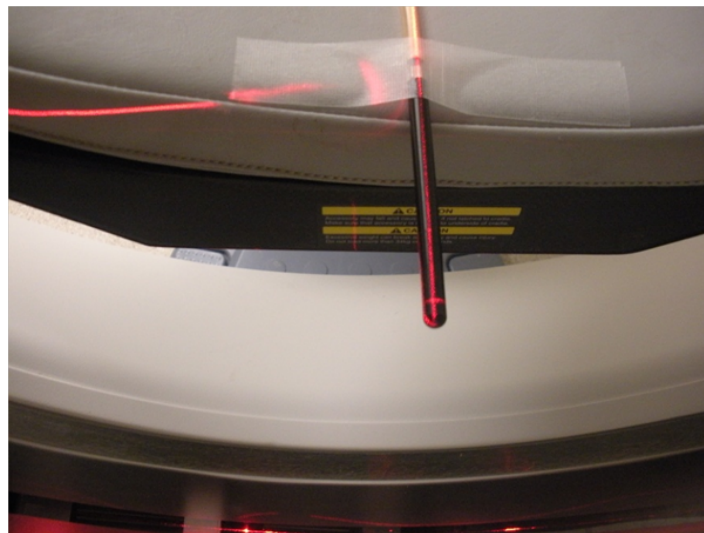


Figure 3.17: Photograph of the setup of A1SL in-air CT scan.

3.4.3.3 Monte Carlo simulations

A Monte Carlo model of the A1SL ionization chamber was established using the EGSnrc code based on the dimensions and material information from the manufacturer. The di-

3.4.4 Conversion factor for absolute dose

For a large-body scan with the large-body bowtie filter at 120 kVp, the conversion factor using the methodology described in Section 3.4.1 was determined to be $2.406 \times 10^{15} [\text{mGy}/\text{mAs}/d_{\text{sim}}]$. This value will be verified (see Section 4.2) and used in the future work (Chapter 7) to determine dose to patient at a certain mAs level.

It should be noted that this conversion factor was determined using an in-air measurement of the A1SL ionization chamber. In-phantom measurement was not performed for the purpose of determining mAs-to-dose conversion factor. In the next chapter, in-phantom measurements with TLDs will be described for the purpose of verifying this determined mAs-to-dose conversion factor.

Chapter 4

Monte Carlo verification and clinical implementation

4.1 Verification of spectrum and bowtie filter

4.1.1 In-phantom output measurements

Percentage depth dose (PDD) is commonly used as a beam quality indicator, especially for high-energy x-ray or electron beams. In the AAPM's TG-51, the percentage depth dose at 10 cm depth of water ($\%dd(10)$) is recommended as the beam quality indicator for photon beams, and R_{50} , the depth in water in cm at which the absorbed dose falls to 50% of the maximum dose, is recommended as the beam quality indicator for electron beams [1999]. For a routine beam energy constancy check, the measurement of the output ratio at two different depths in water or other tissue-equivalent phantom is recommended to perform for external radiation therapy beams [1994, 2009]. The similar methodology of using the output relative to a reference point to test the beam quality was applied in this work for the verification of the post-bowtie-filter spectrum of a CT scanner.

Since CT scanners have a rotational source, it is preferable to test the beam quality under the operational status when the source is rotating. For a uniform cylindrical phantom, when the center of the phantom is aligned to the isocenter of the CT scanner and the longitudinal direction of the phantom is aligned to the z direction of the scanner system, the dose distribution is cylindrically symmetric about the axis of the phantom as a function of the radial distance. Therefore, instead of taking the output at different depths for one view angle, the output at a certain distance from the source was measured in a cylindrical phantom. The output at different locations relative to isocenter was used to represent the quality of the post-bowtie-filter beam, and compared with Monte Carlo simulated output ratios to verify the source spectrum and bowtie filter.

4.1.1.1 Methods and materials

Measurements A PMMA CT dose phantom kit (Model 007A, CIRS, Norfolk, VA) that includes a pediatric head, an adult head and an adult body parts was used to perform the output measurements. The diameters of these three components are 10 cm, 16 cm, and 32 cm, respectively. The length of the phantom kit is 14 cm. There are four holes for inserts at the edge of each component of the phantom and one central hole in the center of the pediatric head part, for a total of 13 inserts. The holes have a nominal inner diameter of 13.1 mm. The centers of the holes are 1 cm away from the edges of each component. CT ionization chambers with a similar length as the phantom, or other custom-designed inserts can be placed at any of the insert positions. All of the phantom parts fit together and were used at the same time for measurements in this work. Figure 4.1 shows a photograph of this CT dose phantom kit.

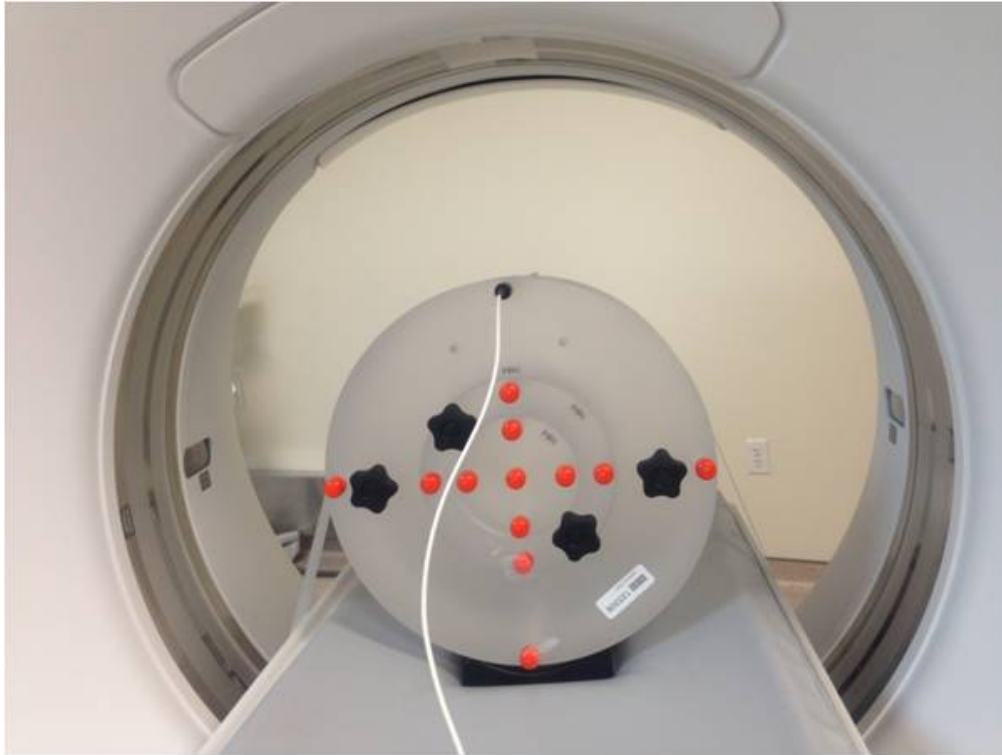


Figure 4.1: Photograph of the CT dose phantom kit used for output measurements. An Exradin A101 CT ionization chamber is inserted at one of the peripheral locations.

The scan was performed on a GE HD750 CT scanner (GE Healthcare, Waukesha, WI) at the University of Wisconsin Imaging Center. The center of the CT dose phantom kit was aligned to the isocenter of the CT scanner with the lasers of the scanner. This scan used a 120 kVp with a large-body bowtie filter in the beam and a 20 mm collimation. The couch was kept stationary. One rotation at a speed of 0.5 s/rotation and 400 mAs were applied for the CT scan. An Exradin A101 CT ionization chamber (Standard Imaging, Middleton, WI) with a nominal length of 13.1 mm and 4.54 cm³ collecting volume and a Max 4000 electrometer (Standard Imaging, Middleton, WI) were used to take the output measurements at different locations in the phantom. A bias of +300 V was applied to the ionization chamber to allow collection of negative charge.

The A101 ionization chamber was placed at the peripheral locations of each component and the central location of the phantom. The same scan parameters were used for the measurements at each location. The average of the four peripheral chamber readings at the peripheral positions of each part of the phantom, which have the same distance from the central position, was obtained. The ratios of the average readings to the chamber reading obtained at the central position were calculated and compared with those from Monte Carlo simulations.

Monte Carlo simulations Monte Carlo simulations were performed with the DICOM images of the CT dose phantom kit using GMctdospp. To obtain the CT images for dose calculations, no ionization chamber was present to avoid possible material assignment errors for dose calculations. The axial view of this phantom is shown in Figure 4.2. The CT number within the phantom ranged from 115 HU to 130 HU. For material assignment, the CT number boundary was set to be -50 HU to 200 HU for PMMA, and -1024 HU to -50 HU for air. The scan parameters in the Monte Carlo program were defined to reflect the conditions of the in-phantom output measurements. The spectrum and bowtie filter information used in the input file were those determined in Sections 3.2 and 3.3. A PEGS data file was created using egs-gui GUI [NRC, 2009] including materials for PMMA and air. The dose grid size was set to $2.5 \text{ mm} \times 2.5 \text{ mm} \times 2.5 \text{ mm}$. A 20 mm collimation size was used to match the one applied for the CT scan. The dose to the phantom from one single rotation at the center of the phantom was calculated. The average dose to each insert within different phantom parts corresponding to the measurement locations was obtained by taking the integral of dose profile along the z direction each location of the insert. For each of the three location groups (adult body peripheral, adult head peripheral, and pediatric head peripheral), the average value for the four inserts was used as the simulated dose. The ratios of these simulated doses relative to the simulated dose at the central location were calculated.

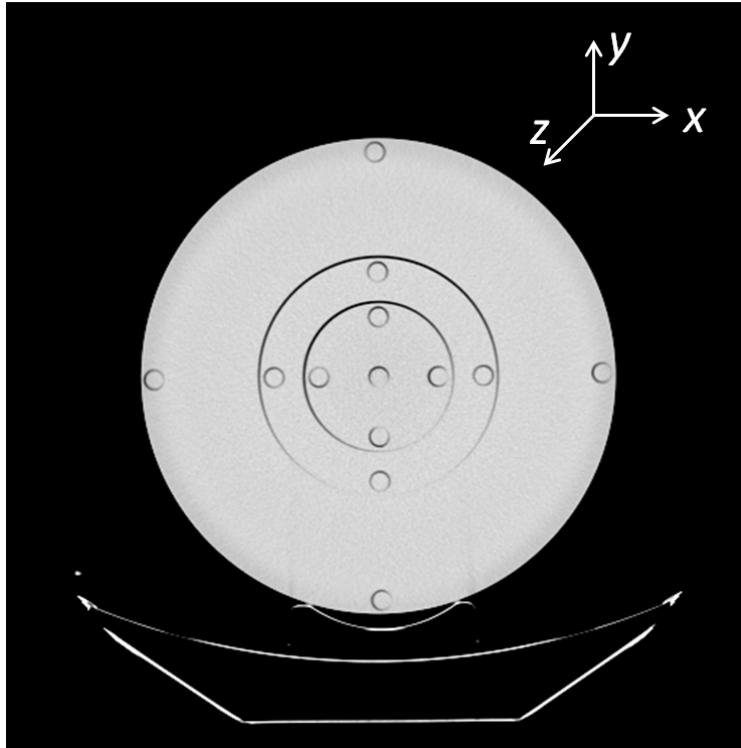


Figure 4.2: The axial view of the CT dose phantom kit. The images of the phantom were used to perform dose calculations using GMctdospp. No ionization chamber was inserted into this phantom. The x , y , and z directions are shown to represent the coordinates of CT system.

4.1.1.2 Results

The Monte-Carlo-calculated dose distribution within the middle slice along the z direction is shown in Figure 4.3. The asymmetric dose distribution along the y direction is due to the existence of the couch. The comparisons of the output at different locations relative to isocenter between the in-phantom measurements and Monte Carlo simulations are shown in Table 4.1. The output at the peripheral locations relative to the isocenter between measurements and Monte Carlo simulations are 0.22%, 1.42%, and 1.63%, for the distances to the isocenter of 15 cm, 7 cm and 4 cm, respectively.

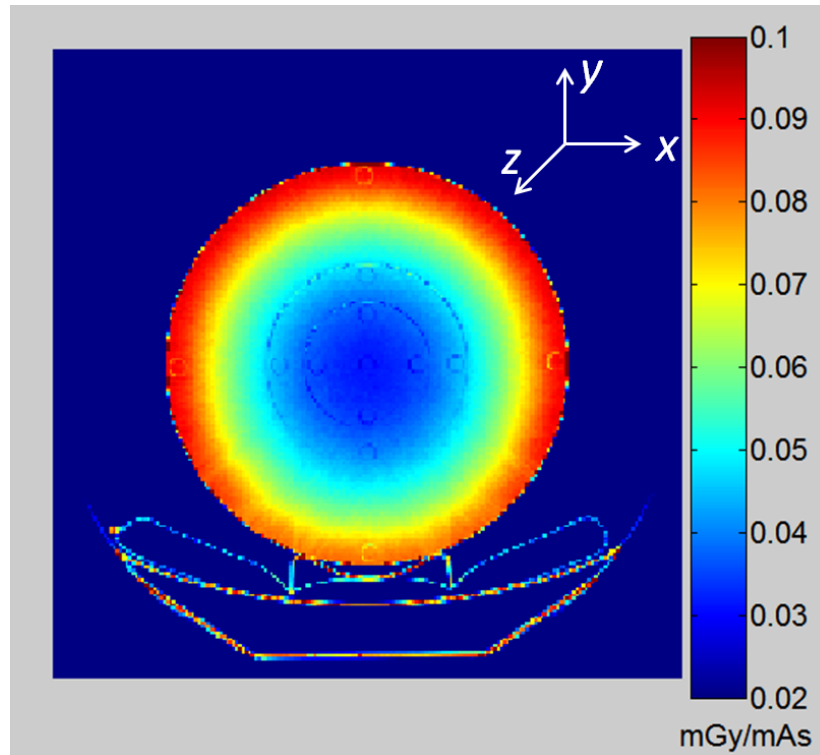


Figure 4.3: The dose distribution (mGy/mAs) within the central slice along the z direction.

The discrepancies between the measurements and the simulations decrease with the distance from the center. One possible reason for the discrepancies is the nonuniformity of the phantom, especially the air gaps between phantom parts with a measured width of less than 1 mm, as shown in Figure 4.2. The dose grid size set in GMctdospp was $2.5 \text{ mm} \times 2.5 \text{ mm}$ in the $x - y$ plane, which did not appropriately model the small air gap between phantom parts. This effect had a larger effect at the locations closer to the center and resulted in a larger discrepancy between measurements and simulations.

4.1.2 Sensitivity tests of different beam qualities

In order to test the accuracy of using the output ratio for the validation of the spectrum and bowtie filter or post-bowtie-filter spectrum, a sensitivity test was designed. Four 120 kVp

Table 4.1: Comparisons of the output at different locations relative to isocenter between in-phantom measurements and Monte Carlo simulations.

Phantom component and location	Distance from center (cm)	Relative output (measured)	Relative output (simulated)	Difference (%)
Center	0	1	1	-
Adult body peripheral	15	2.013	2.009	0.22
Adult head peripheral	7	1.346	1.326	1.42
Pediatric head peripheral	4	1.127	1.109	1.63

spectra with different HVLs were selected, and each was used as the source spectrum to simulate the output at different locations relative to the output at the center.

4.1.2.1 Descriptions of the four different spectra

The first beam quality used for this sensitivity test was the UW120-M beam, which matches the first and second half-value layers of the M120 beam at the National Institute of Standards and Technology (NIST). The spectrum for this beam is from the measured data in the thesis of Moga, who used a high-purity Ge spectrometry system to measure the kilovoltage x-ray beams at the UWADCL [Moga, 2011]. The UW120-M beam has a 120 kVp and a HVL of 6.98 mm Al.

The second beam quality used for this sensitivity test is the RQT9 beam, which is a reference radiation quality for CT as described in International Atomic Energy Agency (IAEA) Technical Report Series No 457 (TRS-457) [2007]. This beam quality has a 120 kVp and 8.37 mm Al HVL. The spectrum was obtained using SpekCalc, with the filtration information provided in TRS 457, which includes 3 mm Be, 3.5 mm Al, and 0.246 mm Cu.

The third beam quality is termed “GE-filtration match”. The spectrum for this beam quality was generated in SpekCalc using the filtration information for a large body spectrum provided in the GE HD750 manual. In the manual, it is specified that for a large body scan, the quality equivalent filtration of the x-ray tube is nominally 4.3 mm of aluminum. For

Table 4.2: The kVp and HVL of the four x-ray beams for sensitivity test.

Beam code	kVp	HVL (mm Al)
UW120-M	120	6.98
RQT9	120	8.37
GE-filtration match	120	7.24
GE-HVL match	120	7.80

the collimator with a large filter, the filtration includes 1.998 mm graphite (C), 0.25 mm Al and 0.075 mm Cu, which is equivalent to 3.1 mm Al. The GE HD750 has an anode angle of 7°. The spectrum for this beam was simulated in SpekCalc based on anode angle and filtration material composition. Since SpekCalc does not include C as a selection of filtration material, 1.998 mm Be was used instead as it has a close atomic number ($Z=4$) compared to C ($Z=6$). A total of 4.55 mm Al and 0.075 mm Cu was added as the filtration in SpekCalc. This beam quality has a 120 kVp and a HVL of 7.24 mm Al.

The last beam quality for this sensitivity test is termed “GE-HVL match”, which matches the measured HVL of the large body beam from the GE HD750 CT scanner. The spectrum is the one determined as described in Section 3.2 and to be verified in this work. This beam has a 120 kVp and a HVL of 7.8 mm Al.

The four different spectra have the same kVp and relatively close HVLs, ranging from 6.98 to 8.37 mm Al, as shown in Table 4.2. The four spectra are plotted in Figure 4.4.

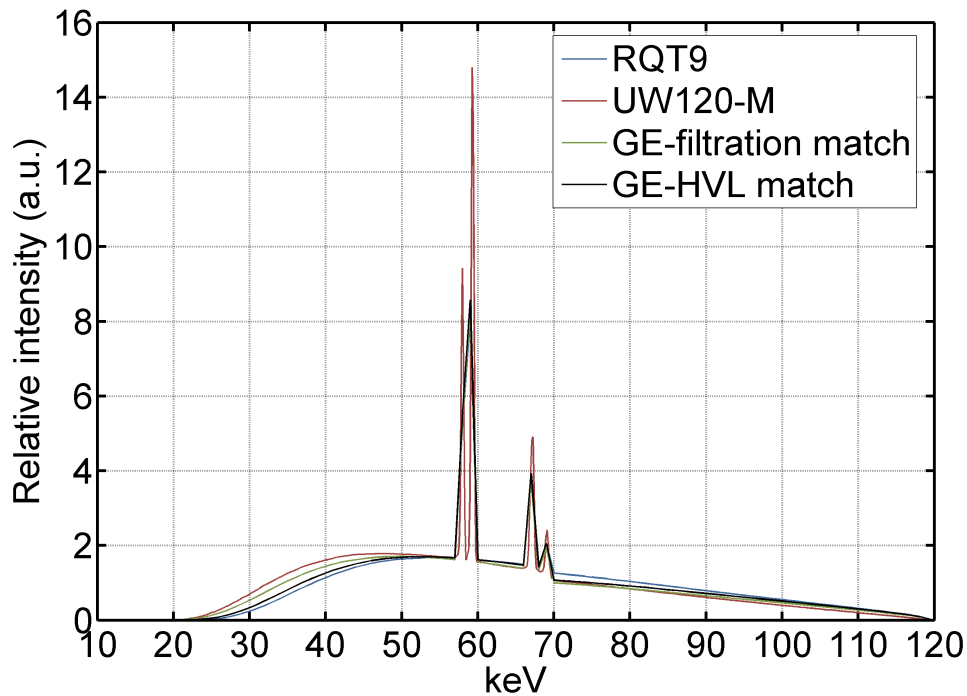


Figure 4.4: Four different spectra for the sensitivity test of simulated output for different beam qualities.

4.1.2.2 Monte Carlo simulations

Monte Carlo simulations were performed using GMctdospp based on the DICOM images of the CT dose phantom (Figure 4.2). The four different spectra were included in the input files separately to obtain the dose distributions within the phantom. All the other simulation parameters, including bowtie filter geometry, collimation setting, and the material assignment boundaries were the same as specified in Section 4.1.1.1. The dose distributions within the central axial plane of the the PMMA phantom were calculated for the four spectra. The average dose at the position of each insert was obtained by taking the integral of the dose profile in the z direction within the phantom at each insert location. The average values for the four inserts of the three location groups (adult body peripheral, adult head

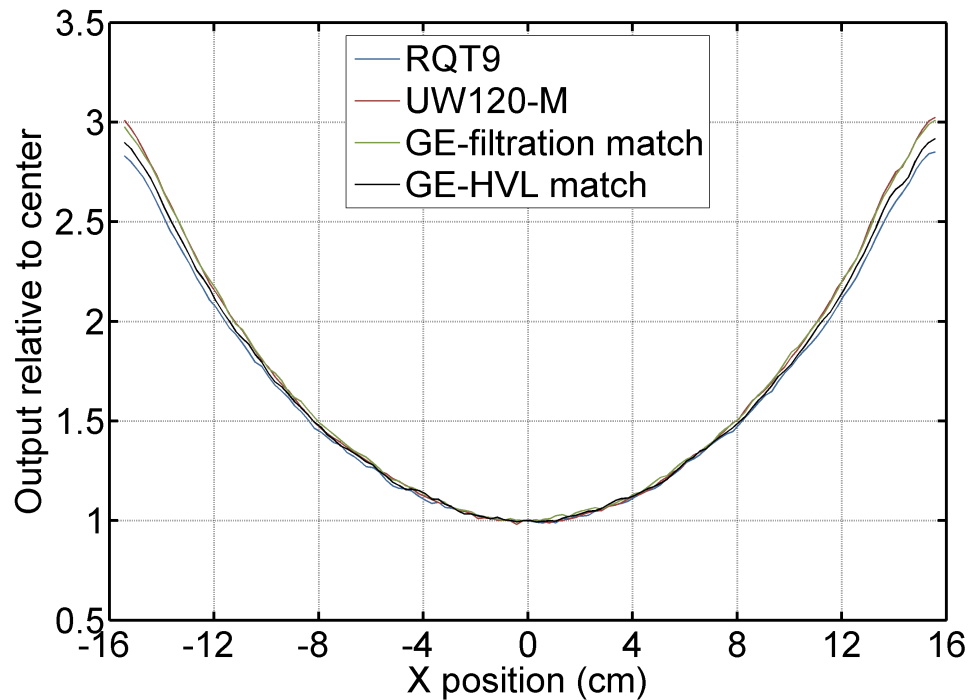


Figure 4.5: The x -direction dose profiles crossing the center of the phantom within the central axial plane of the CT dose phantom when using the four different spectra for Monte Carlo simulations.

peripheral, and pediatric head peripheral) were used as the simulated doses. The ratios of these simulated doses relative to the simulated dose at the central location were calculated.

4.1.2.3 Results

The x -direction dose profiles crossing the center of the phantom within the central axial plane of the CT dose phantom when using the four different spectra are shown in Figure 4.5. The dose at each point was normalized to the dose at the center for each profile. The largest difference of the dose relative to the center appears at the edge of the cylinder. The maximum difference of relative dose among the four different spectra was 5.5% between UW120-M and RQT9 at the edge slice of the phantom, near the edge of the cylinder.

The simulated output at the peripheral positions relative to center are different when using the different spectra, as shown in Table 4.3. Differences of the output at each insert relative to the output at the center between the in-phantom measurements and Monte Carlo simulations are shown in Table 4.3. Root mean square deviations (RMSD), which sums up the differences for the three locations for each beam quality are listed in the last column of Table 4.3. It is seen that when using the GE-HVL match beam spectrum, the Monte-Carlo-simulated output has the smallest discrepancy (2.18% RMSD) compared to the in-phantom measurements performed on the scanner. Two conclusions can be drawn here. First, the sensitivity test shows that when using different spectra in Monte Carlo simulations, even with the same kVp and similar HVL values, the simulated outputs at different locations are different. Therefore, the output at different locations relative to the center is sensitive to the source spectrum. Second, a good agreement is shown when using the large body spectrum and effective large body bowtie filter determined in this work for Monte Carlo simulations compared to the measurements on the CT scanner. The accuracy of the large body spectrum and the effective large body bowtie filter determined for the GE HD750 CT scanner is verified with the in-phantom output measurements on the CT scanner.

4.2 TLD measurements for mAs-to-dose conversion factor

To verify the mAs-to-dose conversion factor determined in Section 3.4.4, another type of radiation dosimeter, the thermoluminescent dosimeter (TLD), was used to test the accuracy of the conversion factor.

4.2.1 Thermoluminescent dosimeter (TLD) use and calibration

4.2.1.1 TLD handling

TLDs measure ionizing radiation by producing visible light (thermoluminescent light, TL) when the detector is heated. The amount of light emitted is dependent upon the radiation

Table 4.3: Differences of the output relative to center at each location between in-phantom measurements and Monte Carlo simulations, and the root mean square deviation (RMSD) of the differences at three locations for four different beam qualities.

Beam quality	Location	Distance from center (cm)	Relative output (measured)	Relative output (simulated)	Difference (%)	RMSD* (%)
RQT9	Adult body	15	2.013	1.959	2.73	
	Adult head	7	1.346	1.317	2.14	3.95
	Pediatric head	4	1.127	1.106	1.90	
UW120-M	Adult body	15	2.013	2.143	6.42	
	Adult head	7	1.346	1.350	0.36	7.37
	Pediatric head	4	1.127	1.087	3.60	
GE-filtration match	Adult body	15	2.013	2.086	3.62	
	Adult head	7	1.346	1.342	0.30	3.79
	Pediatric head	4	1.127	1.115	1.07	
GE-HVL match	Adult body	15	2.013	2.009	0.22	
	Adult head	7	1.346	1.326	1.42	2.18
	Pediatric head	4	1.127	1.109	1.63	

* The root mean square deviation (RMSD) is calculated by: $RMSD = \sqrt{\sum \sigma^2}$, where σ is the percent difference between the measured and simulated output at different locations in the CT dose phantom kit relative to the center for each beam quality.

exposure level. TLD readers heat the TLD, and TL signal is detected by a photomultiplier tube (PMT). TL signal intensity is plotted as a function of temperature in a plot called a glow curve.

LiF:Mg,Ti (TLD-100, Harshaw) TLD chips with the nominal size of (3 mm \times 3 mm \times 0.9 mm) were used in this work. TLDs were handled with a vacuum tweezer to avoid scratches or dirt on dosimeters. The TLDs were annealed before each irradiation to reset the traps in the material. Constant annealing parameters are required to minimize TLD sensitivity drift [Attix, 2004]. The annealing process included heating at 400 °C for 1 hour in an aluminum holder (see Figure 4.6) followed by quick cooling on an aluminum block for 20-30 minutes, and then heating at 80 °C for 24 hours. A Harshaw 5500 hot gas reader (Thermo Scientific, Franklin, MA) was used to read out TLDs 24 hours after exposure. TLD readout parameters (time-temperature profile) include a preheat temperature, heating rate and maximum temperature. The time-temperature profile for chip factor readings included a 100 °C preheat temperature and 300 °C maximum temperature with a heating rate of 25 °C/s. For dose profile measurements, the time-temperature profile included a 50 °C preheat temperature and 350 °C maximum temperature with a heating rate of 15 °C/s. These readout parameters followed the UWADCL TLD readout protocols for chip factor determinations and dose measurements. Previous work has demonstrated that the preheat temperature and heating rate do not affect the TL output [Liang and DeWerd, 2009]. The integral area under a glow curve was obtained as the TL signal.

4.2.1.2 Chip factor determination

Each TLD has an individual sensitivity, termed a “chip factor”. The chip factors to be applied to an experimental measurement can be determined by taking the average of chip factors for an individual TLD determined before and after the experimental cycles. For chip factor determination, all TLDs were irradiated to the same dose level in a uniform



Figure 4.6: Photograph of an aluminum holder for TLD annealing.

field using the UWADCL's Theratronics T1000 ^{60}Co irradiator (Theratronics, Kanata, ON, Canada), as shown in Figure 4.7. For these irradiations, the TLDs were placed in an acrylic holder with 5.2 mm build-up. A known air-kerma level of 10 cGy was given to the TLDs in a $(20\text{ cm} \times 20\text{ cm})$ field at 1 m from the ^{60}Co source. The chip factor, CF_i , for each TLD was determined by

$$CF_i = \frac{M_i}{M_{\text{median}}}, \quad (4.1)$$

where M_i is the reading of the individual TLD and M_{median} is the median of the readings for all the TLDs within the set. The chip factor for each individual TLD was tracked and used to correct for the individual sensitivity in experimental measurements.

In addition to chip factor corrections for individual sensitivity, a background reading, the average of corrected readings for five unirradiated TLDs, was subtracted from the raw reading. Thus, the fully corrected TLD reading (in nC), $M_{\text{corrected}}$ was given by

$$M_{\text{corrected},i} = \frac{M_{\text{raw},i}}{CF_i} - M_{\text{bg}}, \quad (4.2)$$

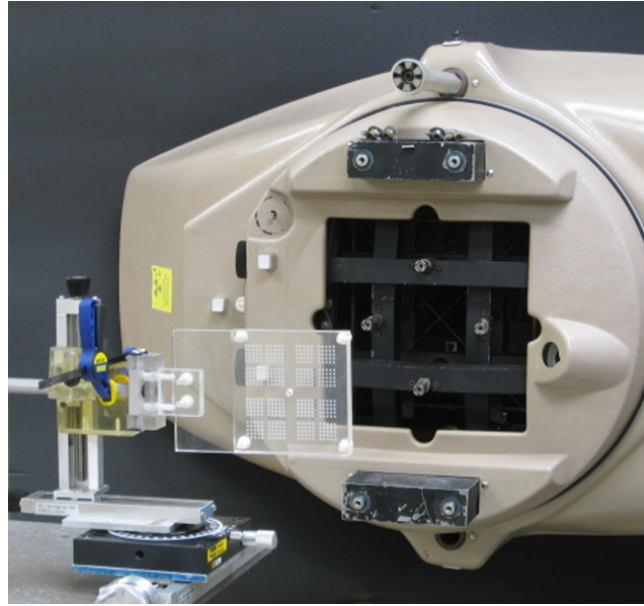


Figure 4.7: Setup for ^{60}Co irradiations of TLDs.

where $M_{\text{raw},i}$ is the raw reading (in nC), CF_i is the chip factor and M_{bg} is the averaged background reading. A calibration is needed to convert $M_{\text{corrected}}$ to dose measured with TLDs.

4.2.1.3 TLD air kerma calibration

The TLD readings were calibrated to air kerma in this work. TLD calibrations were performed on a constant potential x-ray system with a Gulmay CP 320 generator and a COMET 320/26 tungsten anode tube at the UWADCL. Five TLDs were placed in a custom-designed holder, which consisted of two Kapton[®] sheets and Kevlar[®] threads, as shown in Figure 4.8. Two 120 kVp x-ray beams, UW120-M and RQT9, were used for TLD air-kerma calibration (see Section 4.1.2.1 for more details). In all cases, the raw TLD readings were corrected by subtracting the background signal from five unirradiated TLDs and applying the sensitivity correction factor for each TLD.

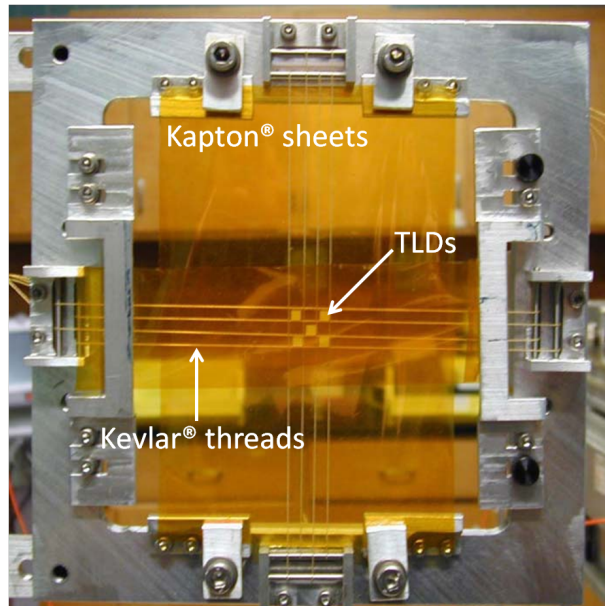


Figure 4.8: Custom-designed holder for x-ray irradiations of TLDs.

The air kerma rate at 1 m from the x-ray source was measured using an Exradin A3 ionization chamber (Standard Imaging, Middleton, WI), which is a NIST-traceable ionization chamber. The TLD in-air holder was aligned using in-room lasers so that the surface of the TLDs was 1 m away from the x-ray source. For each calibration x-ray beam, X , the air-kerma calibration factor of the TLDs, KC_X , is given by:

$$KC_X = \frac{K_{\text{air}}}{M_{\text{corrected}}}, \quad (4.3)$$

where $M_{\text{corrected}}$ is the average of the corrected readings of the five calibration TLDs and K_{air} is the air kerma at the 1 m from the x-ray source. In this work, different exposure times were determined based on the air kerma rate measured with the NIST-traceable ionization chamber to obtain a same air kerma level for calibration irradiations on both UW120-M beam and RQT9 beam, which was 400 mGy.

4.2.1.4 Dose to TLD determinations

The air-kerma determination with TLD is a calibration-based determination. To convert the TLD-measured air kerma to dose, the methodology from Nunn et al.'s work [2008] was applied. Nunn et al. performed Monte Carlo simulations using MCNP5 to determine the dose to TLD per unit incident fluence (D_{TLD}/Φ) using the irradiation geometry and simulations of the air kerma per unit incident fluence (K_{air}/Φ) using a thin slab of air. The ratio $(D_{\text{TLD}}/K_{\text{air}})_X$ was then calculated for a specific x-ray beam, X . The tabulated Gesellschaft für Strahlen und Umweltforschung (GSF) spectra [Seelentag and Panzer, 1979] were used to match the UW-M x-ray beams as approximations. The $(D_{\text{TLD}}/K_{\text{air}})$ for TLD-100 was determined to be 1.098 for the UW120-M beam. Moga ran the same simulations in MCNP5 using both tabulated GSF spectra and the measured spectra. The $(D_{\text{TLD}}/K_{\text{air}})$ ratios for UW120-M were determined to be 1.101 and 1.097 when using the tabulated GSF spectrum and the measured UW120-M spectrum, respectively [2011].

In this work, the $(D_{\text{TLD}}/K_{\text{air}})$ ratios for UW120-M were determined using the same Monte Carlo simulations in MCNP5. The measured UW120-M spectrum and the SpekCalc-determined RQT9 spectrum were used to get the $(D_{\text{TLD}}/K_{\text{air}})$ ratios for TLD-100.

The product of the air-kerma calibration factor, KC_X , and $(D_{\text{TLD}}/K_{\text{air}})_X$ gives the dose-to-TLD conversion factor, DC_X , for different beams, as shown in Equation 4.4.

$$DC_X = KC_X \times \left(\frac{D_{\text{TLD}}}{K_{\text{air}}} \right)_X. \quad (4.4)$$

The dose-to-TLD conversion factor for the large body CT beam, DC_{large} , was obtained by interpolating between $DC_{\text{UW-120M}}$ and DC_{RQT9} based on their HVL values. The in-phantom measured dose to TLD from raw TL readings was determined by

$$D_{\text{TLD},i} = \left(\frac{M_{\text{raw}}}{CF_i} - M_{\text{bg}} \right) \times DC_{\text{large}}. \quad (4.5)$$

4.2.2 z -profile measurements on a CT scanner

4.2.2.1 Methods and materials

Dose profiles along the z direction (the couch direction) were measured on a GE HD750 CT scanner. Arrays of TLDs were placed in custom-designed PMMA inserts for a CT dose phantom, as shown in Figure 4.9. There is a 20 mm gap in the center of the insert that holds 22 stacked TLDs and 1 mm cuts every 5.5 mm apart on each side. A total of 42 TLDs were placed in the insert.



Figure 4.9: Photograph of the custom-designed TLD insert for z -direction profile measurements

The TLD inserts were placed in the CT dose phantom kit at the four peripheral locations of the adult body component. Cine scan mode was performed with the source continuously rotating for 60 rotations. Cine scan mode is the scan mode when the couch does not move and the source is continuously rotating, which is commonly performed for CT perfusion studies and 4D CT imaging [AAPM CT Protocol, 2012, Pan, 2005]. The purpose of using Cine scan mode to perform multiple rotations in this work was to increase the signal to TLDs. Large-body scan parameters of 120 kVp with the large-body bowtie filter were used. The collimation was set to 20 mm at the isocenter. 600 mA and 0.5 s/rotation (i.e., 300 mAs) were used during the scan. 24 hours after the CT scan was performed, the TLDs were read

out and the dose to each TLD was obtained using Equation 4.5 to get the TLD-measured z -profile expressed in dose to TLD.

For Monte Carlo simulations, the same scan parameters as were used in the measurements were simulated and the DICOM images of the CT dose phantom kit were used to perform dose calculations. The simulated scan parameters included 20 mm collimation size and one single rotation with the beam going through the center of the phantom's longitudinal direction. The dose grid size was set to be $2.5 \text{ mm} \times 2.5 \text{ mm} \times 2.5 \text{ mm}$. The spectrum matching the measured HVL and the determined large body bowtie filter were used for the simulations. The dose profiles that were 1 cm away from the phantom edge were obtained as the simulated dose profile. As specified in Section 3.4, the calculated dose is given by dose per particle (in mGy/particle). To get the dose at a certain mAs level, the mAs-to-dose conversion factor and the mAs were applied to the Monte-Carlo-calculated dose to calculate dose (in mGy) to the PMMA phantom.

4.2.2.2 Comparison between simulation and measurement

Figure 4.10 shows the comparison between the TLD-measured z profile and the Monte-Carlo-simulated z profile after applying the mAs-to-dose conversion factor and mAs. It should be noted that the comparison was made between the dose to TLD and dose to PMMA. Because both of these materials are considered to be tissue equivalent [Geraldelli et al., 2013, Chen and McKeever, 1997], the discrepancy of the dose values due to different materials is not discussed here. Good agreement is shown within the beam width, with the largest difference between the measurements and simulations within the beam width being 3.9%. This result verified the accuracy of the mAs-to-dose conversion factor determined in Section 3.4.

More significant discrepancies appeared at the penumbra region and the low-dose region (outside of the beam width), and the discrepancies on one side of the scanner were larger

than on the other side. The averaged absolute differences between the TLD measurements and Monte Carlo simulation within the two low dose regions on each side were 10.8% and 39.8%, respectively. This is mainly due to the fact that the anode heel effect is not modeled in GMctdospp. The asymmetric dose distribution along the z direction on the CT scanner was not properly modeled in the Monte Carlo simulations of this work. Another possible reason for the discrepancy is the presence of the couch. The couch of the CT scanner is not flat and includes a cushion for patient comfort. When the CT dose phantom was set on the couch, the alignment might be not perfect and some tilt along the z direction could happen, which would affect the shape of the z profile measured with TLDs. A third possible reason is that, as the x-ray beam goes through the phantom, the spectrum changes, also known as “beam hardening effect”. The calibration coefficient for TLDs could change due to the beam hardening effect, especially at the penumbra regions. This effect was not considered in this work.

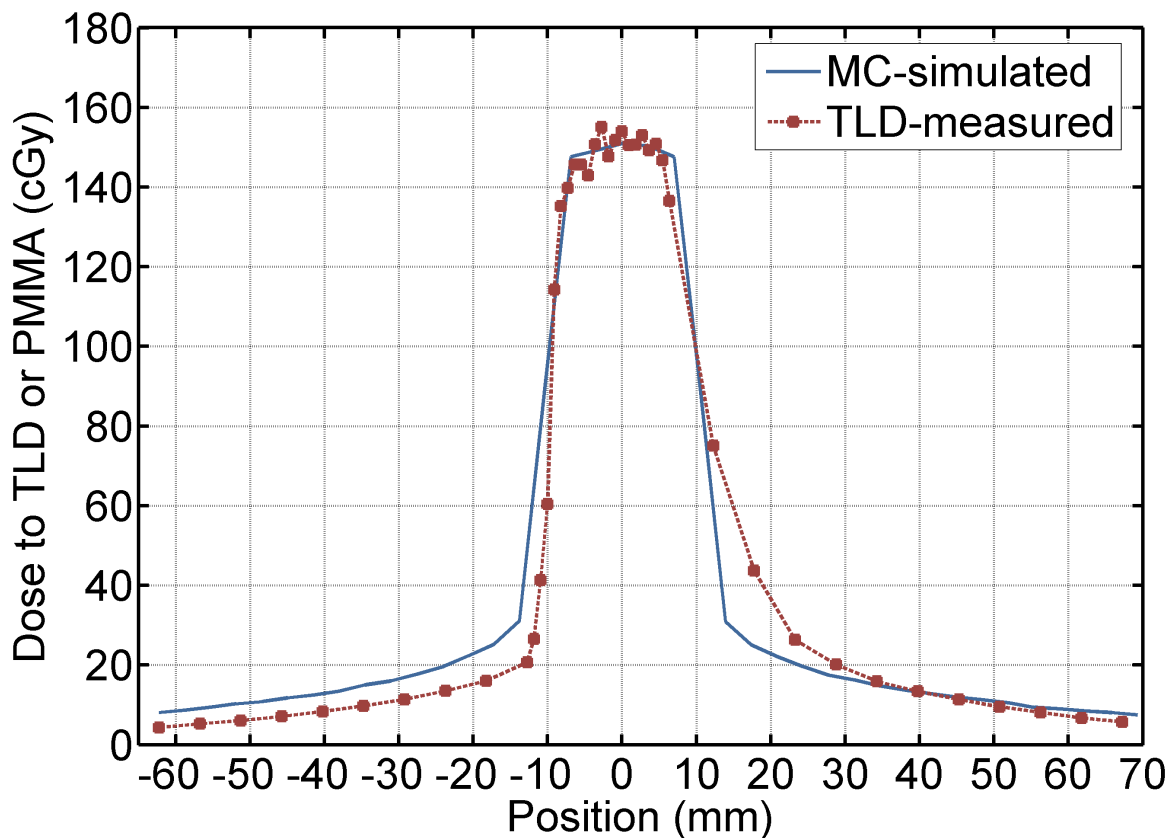


Figure 4.10: Comparison of TLD-measured z profile (dose to TLD) and Monte-Carlo-simulated z profile (dose to PMMA). For these profiles, the beam width is 20 mm.

4.2.2.3 Uncertainty analysis of TLD measurements

The uncertainty analysis of TLD measurements is shown in Table 4.4. Type A uncertainties refer to the standard deviation of the mean value of the measurements. Type B uncertainties are based on scientific judgment using all relevant information available, such as manufacturer specifications. The sources of uncertainty for the TLD experiments were TLD reproducibility, air kerma rate determination, TLD positioning, and TLD reader stability. The TLD reproducibility is a type A uncertainty, which was based on the standard deviation of three rounds of TLD chip factor determinations. The air kerma rate uncer-

Table 4.4: Uncertainties related to Monte-Carlo calculated organ dose.

Parameter	Relative Standard Uncertainty (%)	
	Type A	Type B
TLD reproducibility	4.50	
Air kerma rate determination		0.50
TLD positioning		0.30
TLD reader stability		0.20
Combined uncertainty	4.50	0.62
Total uncertainty (k=1)	4.54	
Expanded uncertainty (k=2)	9.08	

tainty was based on the value reported by the UWADCL, and stemmed primarily from the uncertainty on the NIST calibration of the reference chamber, which was 0.5% (k=1) for the x-ray beam. The uncertainties of TLD positioning and TLD reader stability are considered type B uncertainties, and the values were from Nunn et al.'s work [2008]. The combined uncertainty for TLD measurements is 4.54% at k=1 (66% confidence level) and 9.08% at k=2 (95% confidence level).

4.3 Summary and clinical implementation

In this chapter, the essential parts for modeling a CT scanner in a Monte Carlo program (the spectrum and bowtie filter) were verified. The mAs-to-dose conversion factor determined with an A1SL ionization chamber was verified by another type of dosimeter, TLD. The following is a summary of how the Monte Carlo model can be established in a clinic for a specific CT scanner.

If one starts to establish a model for a CT scanner, three measurements are required to obtain scanner-specific information: HVL measurements for spectrum determination, the flux distribution measurement using an air-scan for effective bowtie filter determination, and ionization chamber measurements for mAs-to-dose conversion factor determination. In this work, only a 120 kVp spectrum and large body bowtie combination is demonstrated.

In a clinic, a similar methodology can be applied to obtain spectra with different kVps and other bowtie filters. The mAs-to-dose conversion factor can be determined with a chamber measurement on the scanner and Monte Carlo model of this chamber. The ratio of the measured and the simulated dose to the active volume of the chamber can be used to determine the mAs-to-dose conversion factor for each post-bowtie-filter spectrum.

Chapter 5

Image extrapolations

In this work, instead of using the existing physical or computational phantoms to represent patient anatomy (see Section 2.5), we aim to use patient CT images to provide patient size and anatomic information. Ideally, if a whole body image is acquired, Monte Carlo simulation should be able to accurately determine the organ dose by simulating the most probable interactions between the x-ray photons and secondary charged particles and the patient. However, it is impractical and violates the As Low As Reasonable Achievable (ALARA) principle to expand the scan range solely for dose calculation purposes. Importing only the CT images to the Monte Carlo program to perform dose calculations would underestimate the dose to the patient. The reason is that CT scans generally include only a portion of the patient body, but photon interactions in regions adjacent to the scanned region also contribute to the overall scan dose. Thus, the use of the CT images alone, which do not include these adjacent regions underestimates the dose, especially at the scan edges. To accurately estimate dose, patient information beyond the scanned region is necessary. Li et al. modeled organs outside of the scanned region by morphing an existing male or female full-body adult Monte Carlo model with the CT images [Li et al., 2011a]. This technique results in accurate Monte Carlo calculations of dose; however, it involves substantial effort.

One way to predict the region beyond the scanned region is to use the existing CT images. By extrapolating the edges of the set of images, prediction of the geometry adjacent to the scanned region is possible. Incorporating image extrapolations into Monte Carlo calculations to simulate possible interactions between the x-ray photons and the patient anatomy could improve the accuracy of the calculated dose distribution within the scanned region. Another method proposed in this work to estimate the geometry beyond the scanned region is to use the two Scout images which are taken before CT scans for localizing the scanned region. Scout images usually include the anteroposterior (AP) and lateral views of the patient and cover a larger region of the patient compared to CT scans. They provide the outer dimensions of the patient beyond the scanned region. Measuring the size of the patient outline based on the AP and lateral Scout images at the positions adjacent to the scanned region would give some guidance on the geometry beyond the scanned region. This method is used in longitudinal mA modulation for modern CT scans, in which an ellipse is used to represent the elliptic asymmetric outline of the patient at each z position [Kalra et al., 2004]. Either the lengths of the long and short axes of an ellipse solely or with the edge slice within the scanned region to form an extrapolation region would also be a candidate to provide scatter to the scanned region and improve the dose calculation accuracy.

In this chapter, the investigation of image extrapolation to improve dose calculation accuracy is presented in two parts. The first part includes studies on a simple cylindrical phantom. The dose underestimation in the absence of the scatter region is demonstrated, and the size of the scatter region required to accurately simulate full-scatter conditions is determined. In the second part, anthropomorphic phantom studies involving a chest scan are performed. Four different image extrapolation methods based on CT images alone, and CT images and scout images are proposed. The dose was calculated with the chest images only and the chest images with the four types of extrapolated images. The results

were compared with the dose calculated using whole body images of the anthropomorphic phantom.

5.1 Cylindrical phantom study

5.1.1 Methods and materials

Since the GMctdospp Monte Carlo simulation program generates input files based on CT images, it was necessary to generate a CT dataset of a cylindrical phantom with the desired dimension and material. A CT DICOM image series from an arbitrary CT scan was loaded into Matlab, and the header information was extracted. The image data were then replaced by a water cylinder with the CT number of 0 HU inside the cylinder for water, and the CT number of -1000 HU outside the cylinder to represent air. The diameter of the phantom was defined as 20 cm. The reconstruction slice thickness of this set of CT DICOM images was 2.5 mm, and the number of image slices was 350, so the length of the cylindrical phantom was 875 mm. The longitudinal axis of the cylinder was along the z direction in the CT system.

A step-shoot CT scan was simulated to cover 120 mm in the center of this 875 mm long cylinder, as shown in Figure 5.1. Using the images within the 120 mm to perform dose calculations represents the scenario of using the CT images without including the adjacent scatter regions. Dose calculated using the images of the whole 875 mm cylinder is considered as the gold standard, since it models the full-scatter condition. The determined 120 kVp spectrum and large-body bowtie-filter geometry for the GE HD750 CT scanner (see Chapter 3) were used in the source definition for all the dose calculations. The calculation grid size was set as (1.25 mm \times 1.25 mm \times 2.5 mm).

To investigate the effect of different collimation sizes on dose determination, two collimation sizes were defined in the Monte Carlo simulation program: 40 mm and 5 mm,

representing the largest and smallest collimation sizes of a typical CT scan. To achieve the same scan coverage with these two collimation settings, 3 and 24 rotations were defined in GMctdospp for these two collimation sizes, respectively.

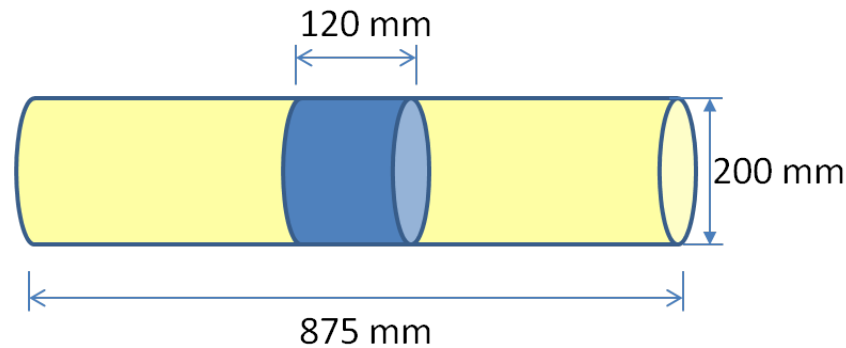


Figure 5.1: Illustration of the mathematical water cylinder size and scanned region (shown in blue).

Dose profiles along the z axis of the scanned region were compared between the cases with no additional scatter and the gold standard. Dose differences compared to gold standard were calculated at five different locations along the z direction, in the center of the cylinder and at 1 cm from the periphery of the cylinder. The dose comparison locations are shown in Figure 5.2.

Dose underestimation was also determined by comparing the dose on the edge slice of the 120 mm scanned region that was calculated with only the acquired CT images to that determined using the whole length of the cylinder. To determine how large a scatter region is needed to accurately approximate full-scatter conditions, 5 mm, 10 mm, 20 mm, and 40 mm-long scatter regions with the same diameter and material were included adjacent to the scan area, as shown in Figure 5.3. The calculated doses on the edge slice of the scanned region with different amounts of adjacent scatter region were compared with the dose at the same position calculated using the whole cylinder.

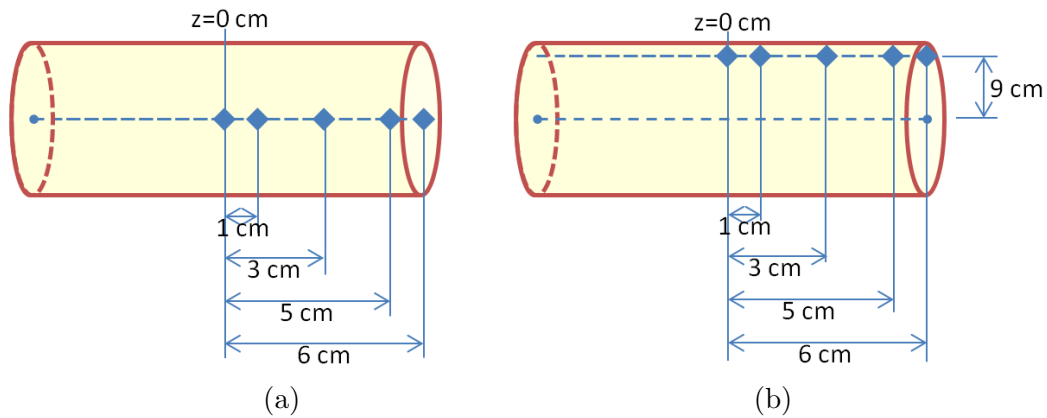


Figure 5.2: Locations for dose comparison between using only the images within the scanned region and the gold standard. The diamonds show the different locations along the z direction. The location where $z = 0$ cm represents the center of the cylinder. (a) Locations are on the central axis of the cylinder. (b) Locations are at 1 cm from the periphery of the cylinder, i.e. 9 cm from the center of the cylinder.

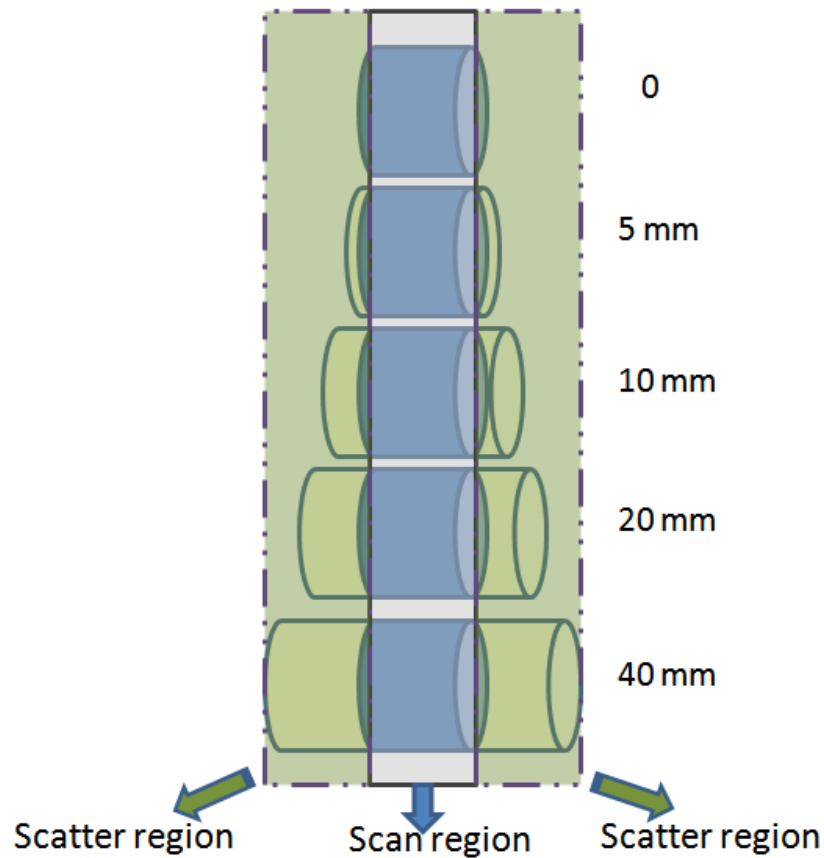
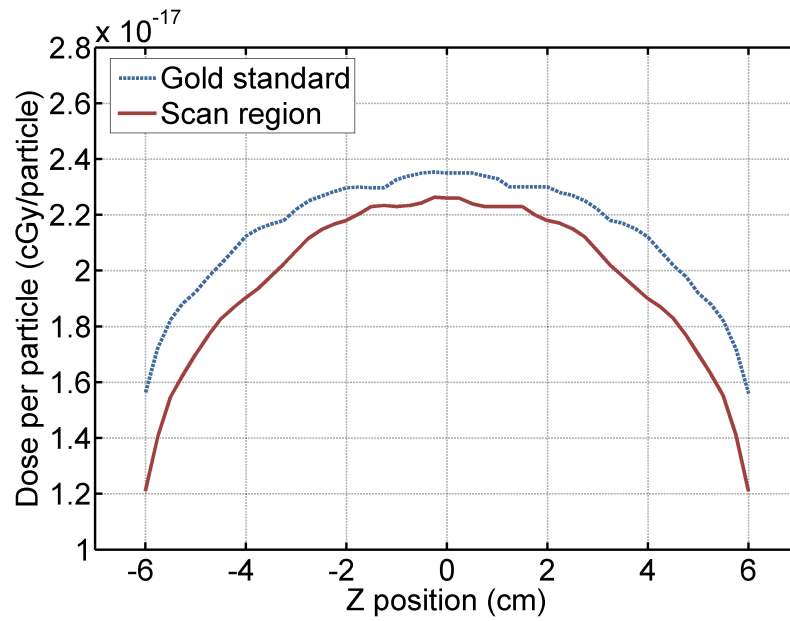


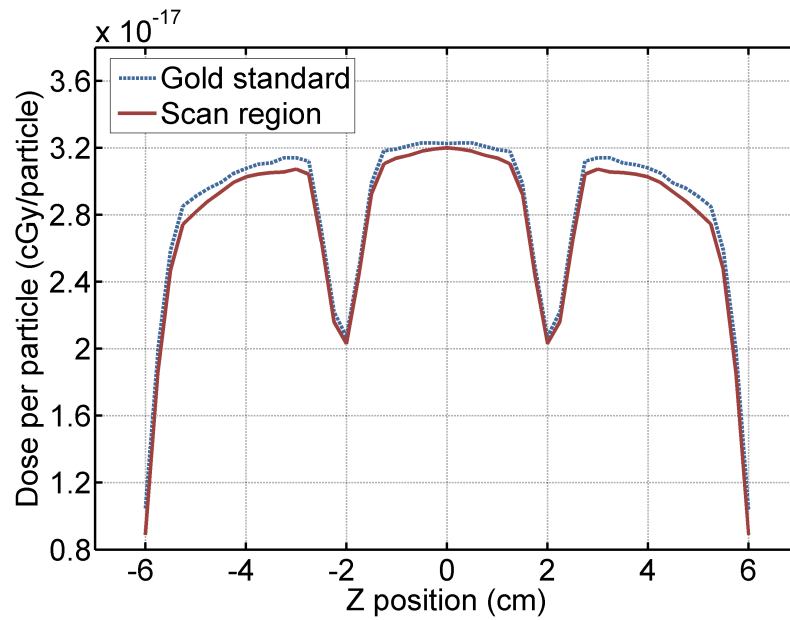
Figure 5.3: Illustration of scanned region and various scatter region sizes for the mathematical phantom study.

5.1.2 Results

The dose profiles along the longitudinal direction within the scanned region at the center of the cylinder and at 1 cm from the periphery of the cylinder are shown in Figure 5.4. The grooves in the dose profiles at the periphery of the cylinder were due to the fact that the beam width was narrower on the periphery than in the center (see Figure 5.5). This underdose effect was partially compensated for when the source was on the opposite side. However, the dose deposition was lower when the source was on the other side of the phantom due to the longer distance from the source and more attenuation the beam went through, and the grooves still appeared.



(a)



(b)

Figure 5.4: Longitudinal dose profiles within the scanned region using the images within the scanned region only and the gold standard for a collimation size of 40 mm. (a) Longitudinal dose profile at the central location of the cylinder. (b) Longitudinal dose profile at 1 cm from the edge of the cylinder.

Table 5.1: Dose underestimation at different locations when using only the images within the scanned region compared to the gold standard. Collimation size: 40 mm.

Distances from scan center along z direction	Dose difference compared to gold standard (%)	
	Center	1 cm from periphery
6 cm	22.4	14.6
5 cm	11.6	3.2
3 cm	6.8	2.1
1 cm	4.1	1.7
0 cm	3.8	0.8

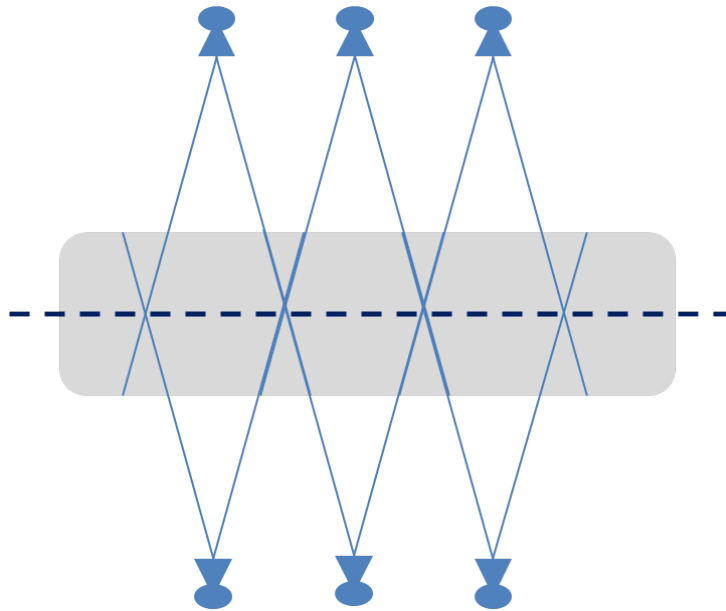


Figure 5.5: Illustration of the grooves on the dose profiles at the edge of the cylinder. The dash line shows the isocenter positions when the source rotates.

The dose differences at five z locations in the center and on the periphery of the cylinder are shown in Table 5.2. The largest discrepancy between the gold standard and the case with no additional scatter appeared to be at the edges of the scanned region. Consequently, the dose underestimation within the plane of the scan edge was further investigated.

The percent dose differences on the edge slice of the scanned region compared to the dose calculated with the whole cylinder are shown in Figure 5.6, including the dose underestimation in the absence of a scatter region, and with 5 mm, 10 mm, 20 mm, and 40 mm-long

scatter regions. It is shown that dose underestimations of up to 25% occur on the edge slice of the scanned region when no additional scatter region was included. The difference was higher in the central region of the cylindrical phantom. The dose underestimation was improved with the inclusion of a scatter region next to the scanned region. Based on the results, a 40 mm scatter region is sufficient to reduce the error of dose estimation within the 875 mm phantom to below 5%.

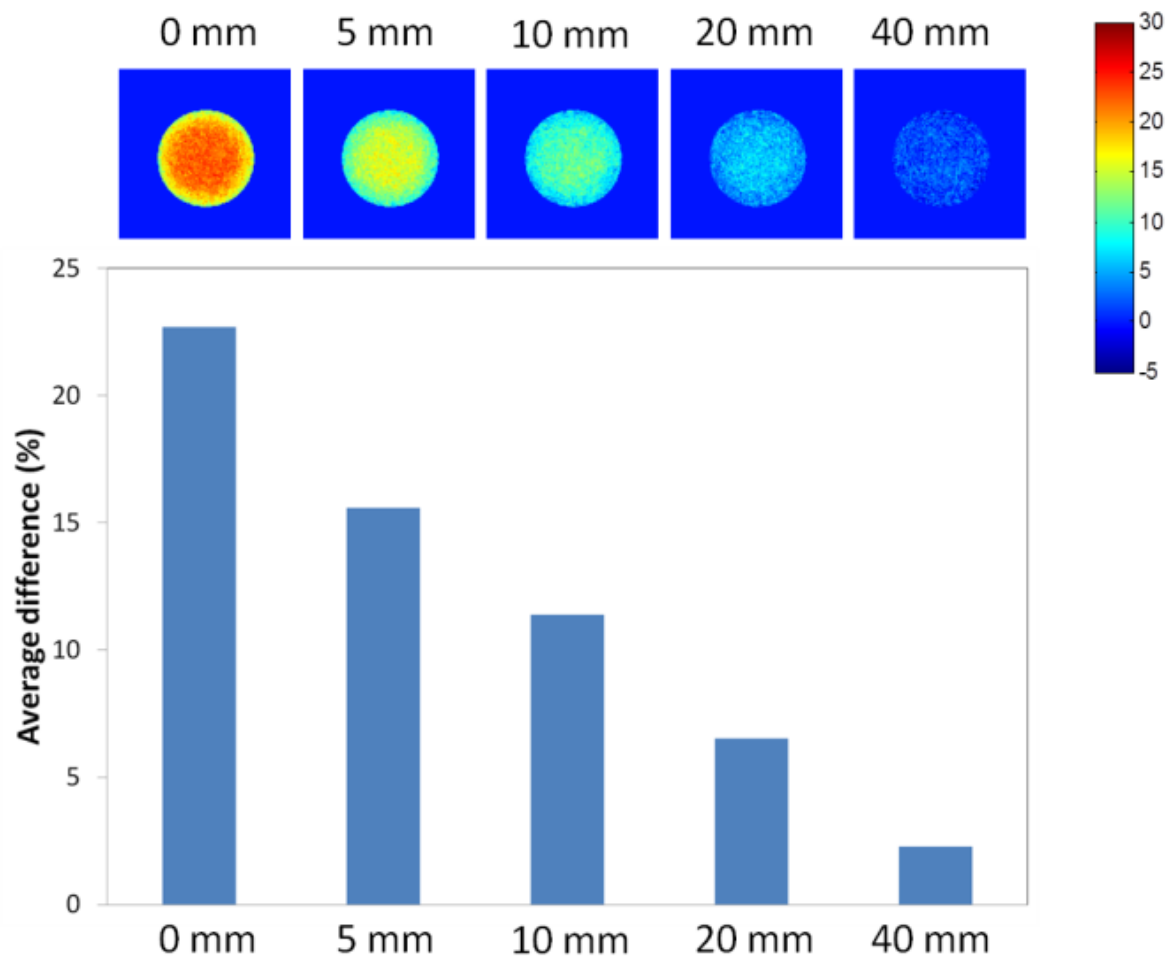


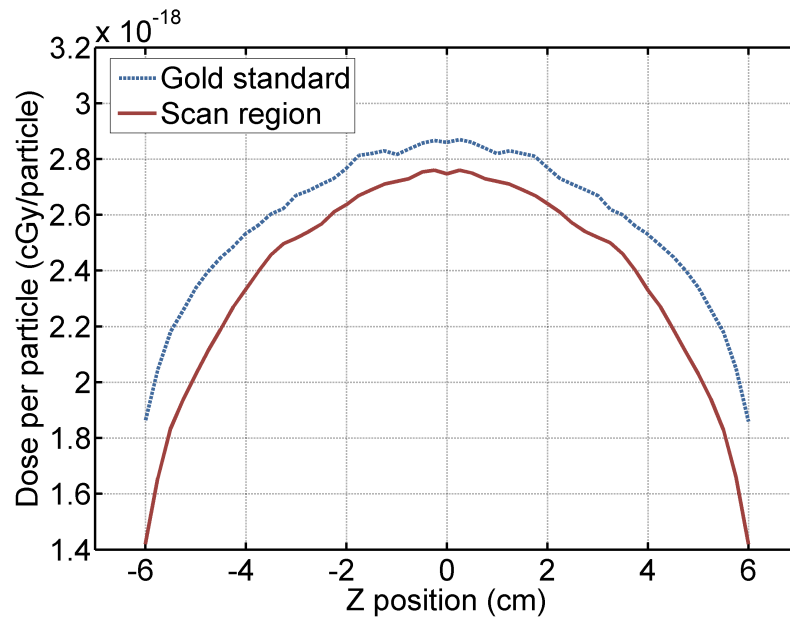
Figure 5.6: Dose underestimation on the edge slice of the cylinder with different scatter regions. Comparisons were made with the gold standard. The simulations were performed using a 40 mm collimation.

Table 5.2: Dose underestimation at different locations when using only the images within the scanned region compared to the gold standard. Collimation size: 5 mm.

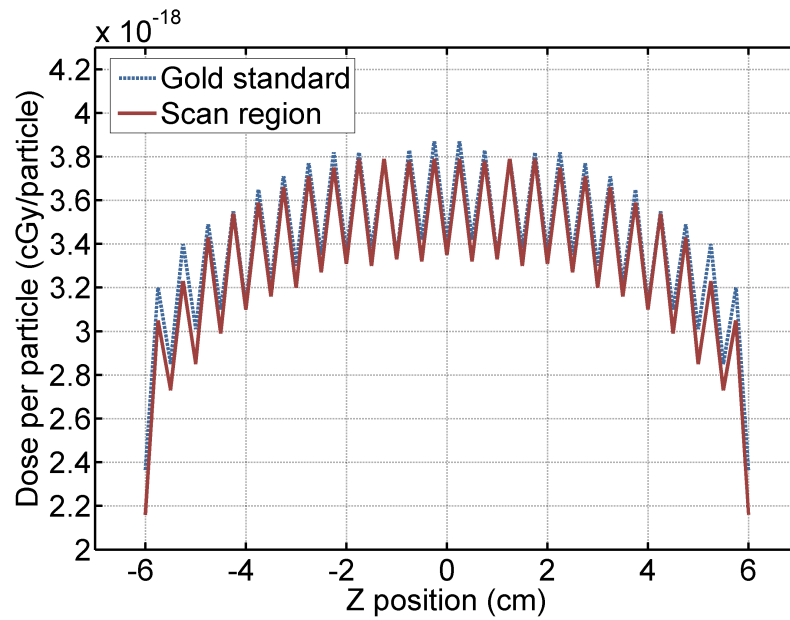
Distances from scan center along z direction	Dose difference compared to gold standard (%)	
	Center	1 cm from edge
6 cm	23.7	8.5
5 cm	13.3	5.3
3 cm	5.7	3.0
1 cm	3.4	2.4
0 cm	4.0	1.8

Similar comparisons were performed when using a 5 mm collimation size to investigate the effect of collimation size on dose underestimation without taking scatter region into account. The grooves on the dose profiles at the edge of the cylinder also appeared similar to those in the 40 mm collimation results. The longitudinal dose profiles along the center of the cylinder and 1 cm from the periphery of the cylinder for the gold standard and the case with on additional scatter regions are shown in Figure 5.7. The dose differences at five z locations in the center and on the periphery of the cylinder are shown in Table 5.2. Similarly to the 40 mm collimation size, the largest discrepancy between the gold standard and the case with no additional scatter regions appeared to be at the edges of the scanned region.

The percent dose differences on the edge slice of the scanned region compared to the dose calculated with the whole cylinder are shown in Figure 5.8. It is also shown that a 40 mm scatter region is required to accurately approximate the full-scatter conditions for 5 mm collimation. In the next part of this chapter, when testing the performance of the different image extrapolation methods proposed in this work, a 40 mm extrapolation region was used.



(a)



(b)

Figure 5.7: Longitudinal dose profiles within the scanned region using the images within the scanned region only and the gold standard for a collimation size of 5 mm. (a) Longitudinal dose profile at the central location of the cylinder. (b) Longitudinal dose profile at 1 cm from the edge of the cylinder.

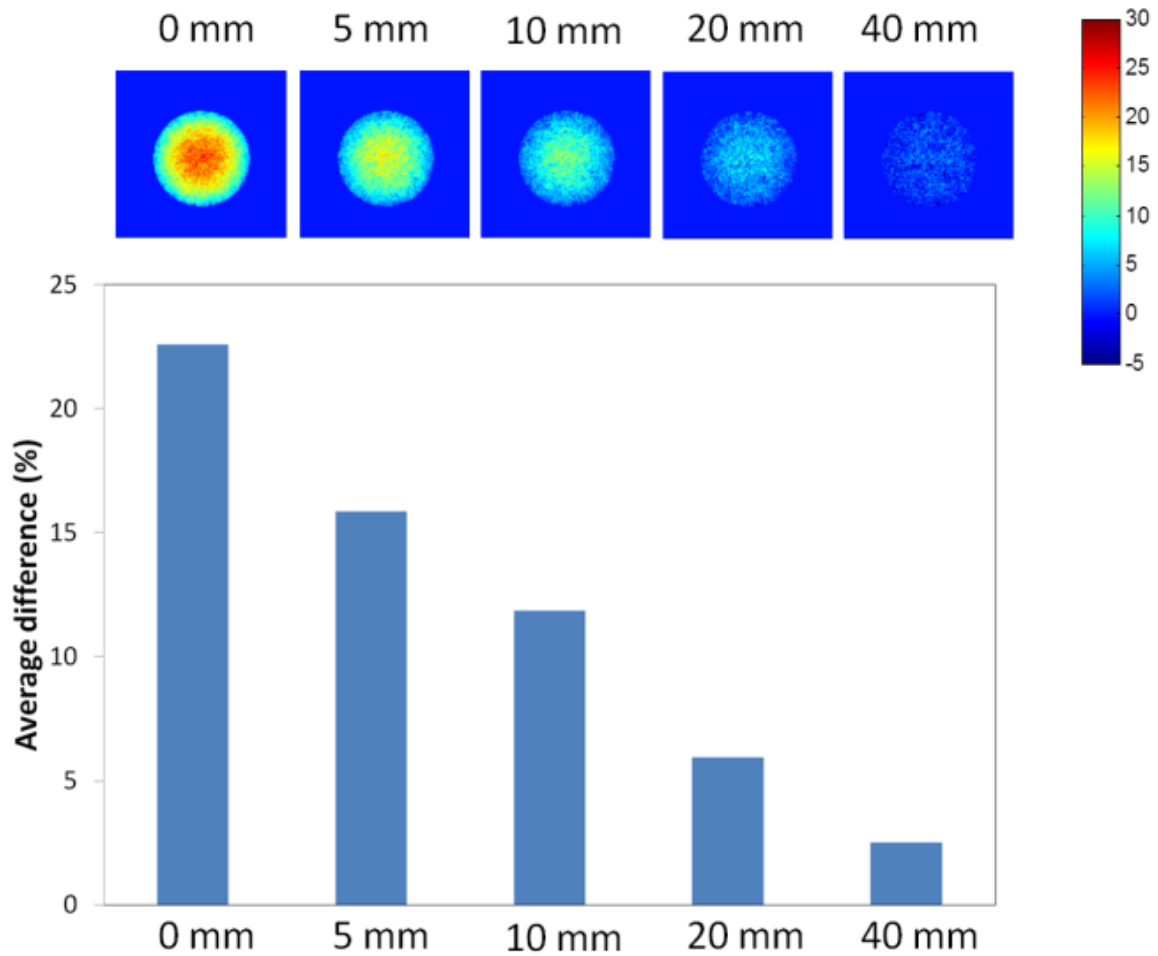


Figure 5.8: Dose underestimation on the edge slice of the cylinder with different scatter regions. Comparisons were made with the gold standard. The simulations were performed using a 5 mm collimation.

5.2 Anthropomorphic phantom study

5.2.1 Methods and materials

5.2.1.1 CT scan

An adult male anthropomorphic phantom, Rando[®] Man (The Phantom Laboratory, Salem, NY), as shown in Figure 5.9, was used to further demonstrate the dose underestimation

that occurs when using only the CT images in real clinical cases and to study the ability of different image extrapolation methods to accurately model full-scatter conditions within the scanned region. A whole body CT scan of the phantom was performed on a GE HD750 CT scanner at the University of Wisconsin Imaging Center, with the head first, supine orientation. A typical large body scan protocol was applied, and a 2.5 mm reconstruction slice thickness was chosen. The thorax region of the whole body image set was taken to represent a typical chest CT scan.



Figure 5.9: Photograph of the setup for the CT scan of a male anthropomorphic phantom.

5.2.1.2 Monte Carlo simulations

Both step-shoot mode and helical scan mode were simulated for dose calculations with Monte Carlo. For the step-shoot mode simulation, a 40 mm collimation size was chosen. A

total of 9 rotations was used to cover the chest region. For the helical scan mode simulation, 40 mm collimation and a pitch of 0.984:1 were chosen. The determined 120 kVp spectrum and large-body bowtie-filter geometry for the GE HD750 CT scanner (see Chapter 3) were used in the source definition for all the dose calculations. The calculation grid size was set to be (1.25 mm \times 1.25 mm \times 2.5 mm).

5.2.1.3 Image extrapolation methods

Four different image extrapolation methods to create the scatter region for dose calculations were investigated. Two of the methods were based on the patient CT images only. The other two methods take advantage of Scout images, which are the radiographic type of images taken prior to CT scans for localization. Scout images usually cover a larger region compared to the CT scan, and therefore, provide some information of the patient anatomy in the regions that are adjacent to the scanned region.

The first method is termed “nearest neighbor stacking”. This method uses the last slice of the scanned region as the template to build the scatter region beyond the scanned region. The edge slice of the CT image (nearest neighbor) is repeatedly stacked upon itself so that all the images in the extrapolated scatter region are the same as the template slice. The number of image slices is determined by the desired amount of additional scatter (40 mm in this work) and the reconstruction slice thickness. This method is demonstrated in Figure 5.10(a). The second extrapolation method is linear extrapolation, which uses the 5 slices of the CT images closest to the edge of the scanned region and performs a pixel-by-pixel linear extrapolation to create the 40 mm scatter regions at each end of the chest images. The demonstration of linear extrapolation is shown in Figure 5.10(b). Both of these methods generate the extrapolation regions based on the CT images only.

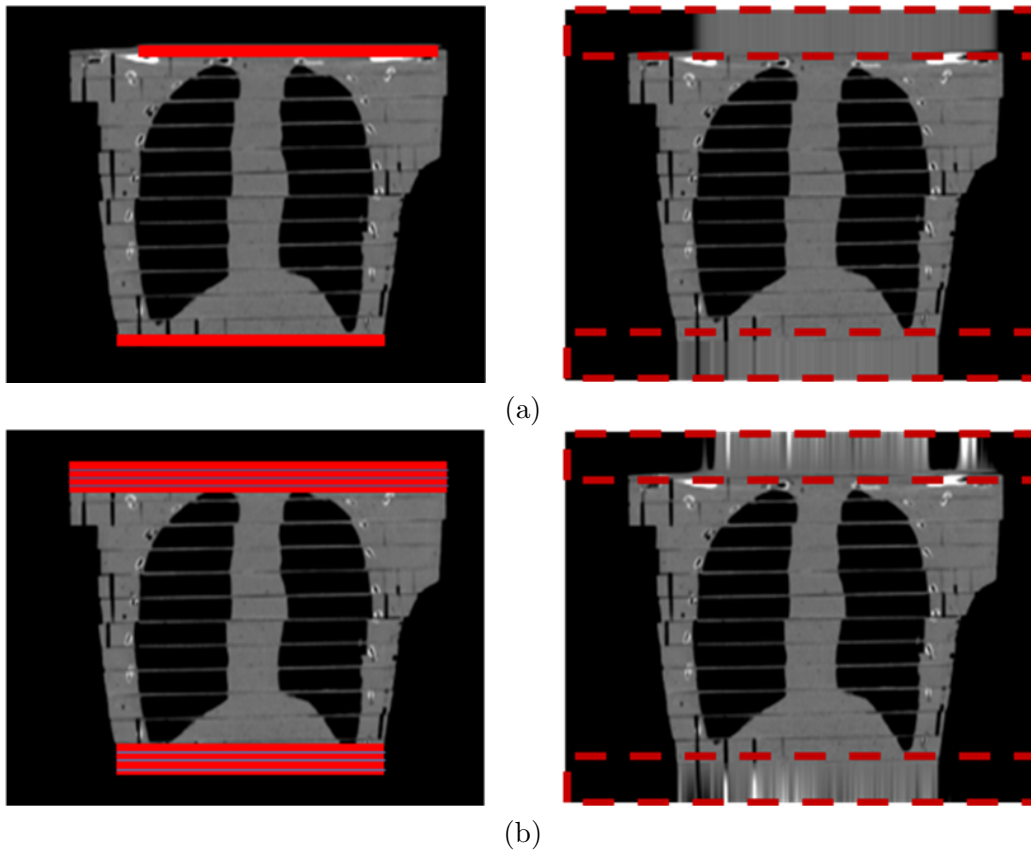


Figure 5.10: (a) The coronal view of a chest scan with the red line indicating the slice used for the nearest neighbor stacking (left), and the extrapolated scatter region shown in the dashed boxes generated by the nearest neighbor stacking (right). (b) The coronal view of a chest scan with the red lines indicating the slices used for the linear extrapolation (left) and the extrapolated scatter region shown in the dashed boxes generated by the linear extrapolation (right).

The third method measures the lateral and AP dimensions of the patient on the Scout images at each z location adjacent to the scanned region. At each z location, an ellipse is formed, with long and short axes determined based on the lateral and AP dimensions measured from the Scout images at the corresponding z position, as shown in Figure 5.11(a). These ellipses are stacked next to the scanned region to form the extrapolated images. This method is shown in Figure 5.11(b). The fourth method is termed “the resized nearest neighbor”, which resizes the image on the edge based on the ellipse dimensions determined

from the Scout images. The resized images are then used as the extrapolated images to provide scatter to the scanned region, as shown in Figure 5.11(c). These two methods used both the patient CT images and the Scout images.

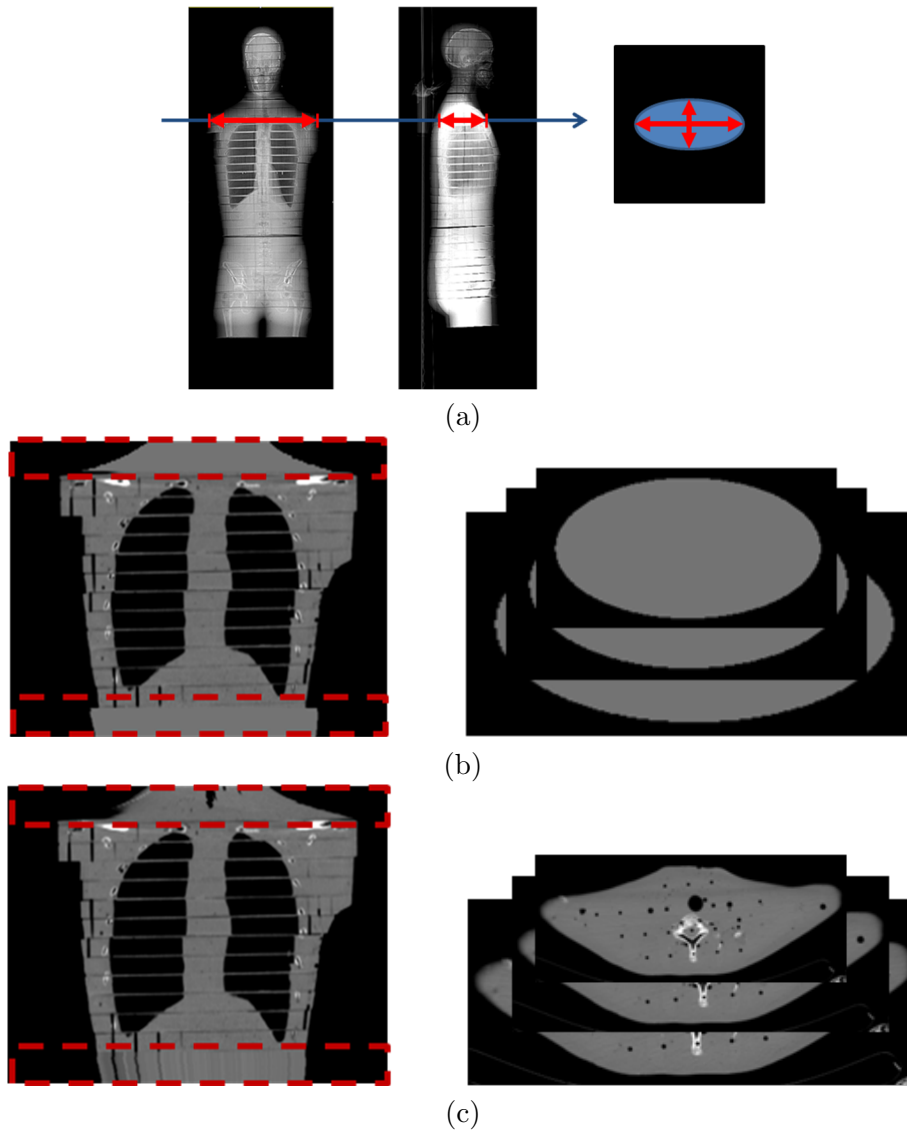


Figure 5.11: (a) The determination of the long and short axes at a z location from AP and lateral scout images; (b) the coronal view of the chest scan with the scatter region shown in dashed boxes generated by the ellipses based on scout images; (c) the coronal view of the chest scan with the scatter region shown in dashed boxes generated by resized nearest neighbor based on scout images.

Based on the results of the cylindrical phantom study, a 40 mm scatter region was shown to provide sufficient scatter to the scanned region. Such extrapolated scatter regions were generated using each of the four methods. For each method, the dose to the edge slice of the scanned region was computed and compared with that calculated using the CT images only and the dose calculated from the full body CT scan.

5.2.2 Results

5.2.2.1 Nearest neighbor and linear extrapolations

For the chest scan case studied in this work, the dose distribution on the edge slice of the scan region was calculated in GMctdospp using the chest CT images. Similar to the cylindrical phantom study, the dose distribution on the edge slice was also calculated using the whole-body Rando phantom images as the gold standard. Simulation parameters, including collimation settings and scan coverage, were identical for all of these simulations. The dose underestimation in the absence of an additional scatter region is shown in Figures 5.12 and 5.13 for superior and inferior slices of the scanned region when simulating a step-shoot CT scan. Dose underestimation of up to 35% is evident when the region which was not scanned was not taken into account in the Monte Carlo simulations. The accuracy of the dose calculation was improved by adding extrapolation regions to both ends of the received CT images from the scanner.

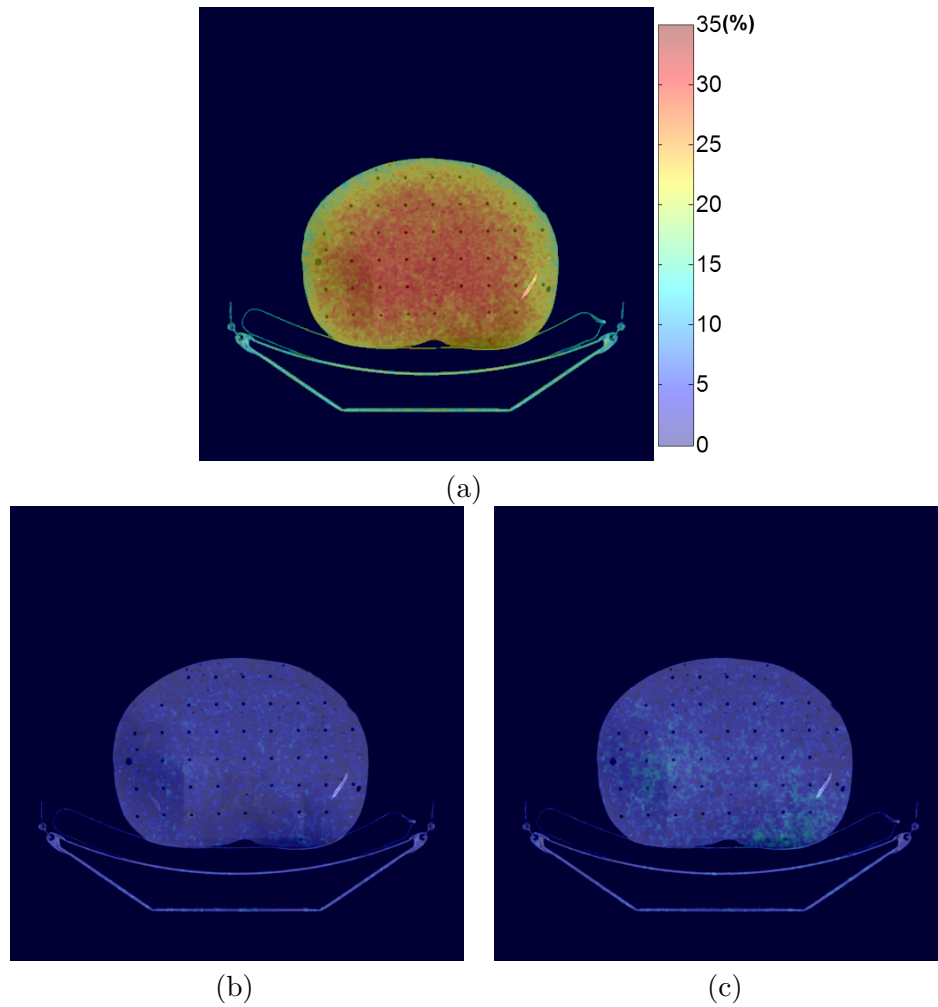


Figure 5.12: Dose difference (%) on the inferior slice of the chest scan (pelvic) compared to using whole-body Rando CT images. Monte Carlo simulations were performed for a step-shoot scan mode using (a) chest CT images; (b) chest CT images with extrapolated images by stacking the nearest neighbor; and (c) chest CT images with extrapolated images by linear extrapolation of 5 slices on the edge.

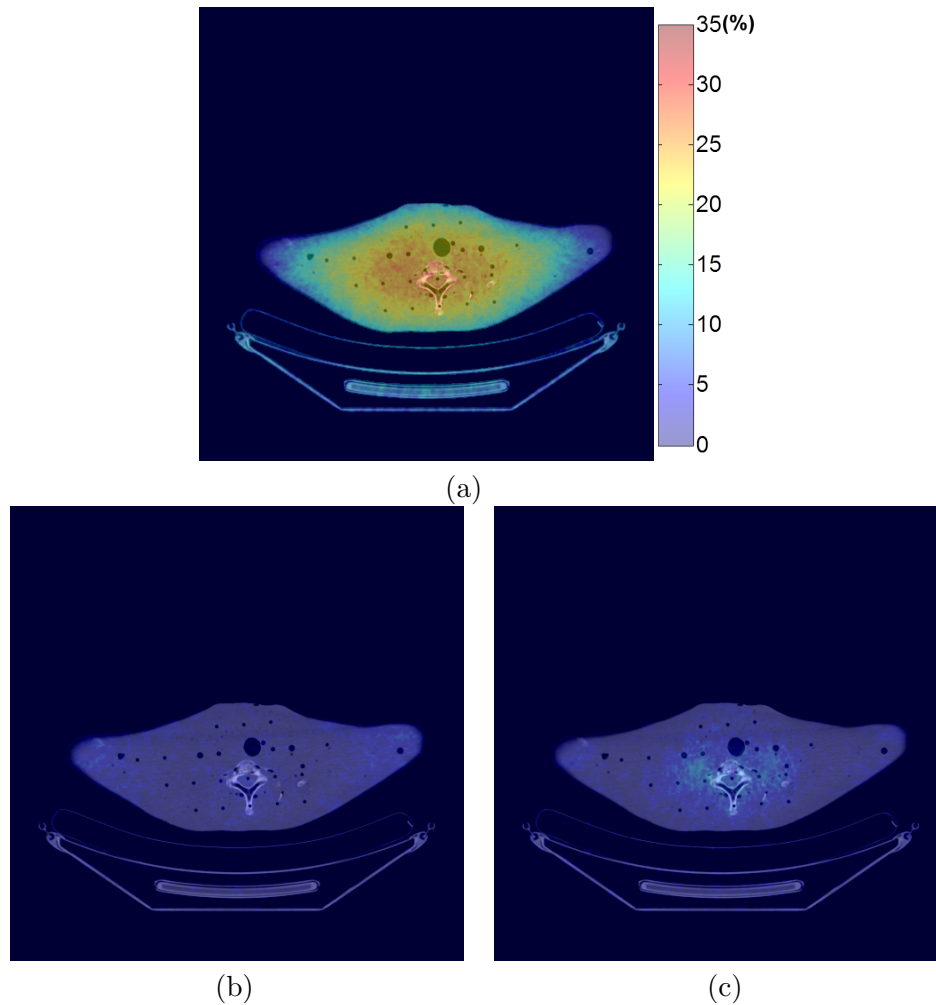


Figure 5.13: Dose difference (%) on the superior slice of the chest scan (shoulder) compared to using whole-body Rando CT images. Monte Carlo simulations were performed for a step-shoot scan mode using (a) chest CT images; (b) chest CT images with extrapolated images by stacking the nearest neighbor; and (c) chest CT images with extrapolated images by linear extrapolation of 5 slices on the edge.

Monte Carlo simulations of dose from a helical scan were also performed following the same methodology. The comparisons between dose calculations using the chest CT images only, chest images plus extrapolated images, and the whole-body images are shown in Figures 5.14 and 5.15 for the superior and inferior slices, respectively. For the helical scan case, the dose calculations were still improved by adding extrapolated regions to the CT images. The dose underestimation was minimal on the inferior slice (in the pelvic region) with addition of an extrapolation region. However, a dose underestimation of up to 5% and 20% was evident in the superior slice (in the shoulder region) of the scan for the nearest neighbor stacking and linear extrapolation methods, respectively. This is due to the fact that the outline of the shoulder region changes dramatically with position. Stacking the edge slice of the existing images to obtain the extrapolation region does not reflect the real geometry of the patient. When using linear extrapolation, the discrepancy between real patient geometry and extrapolated images could be even worse because the internal anatomy of the human body does not change linearly.

5.2.2.2 Extrapolation using Scout images

The dose differences compared to the gold standard for simulations of step-shoot scan mode are shown in Figures 5.16 and 5.17 when using the chest CT images plus the ellipses determined from Scout images and chest CT images plus the resized nearest neighbor extrapolated images. The dose differences compared to the gold standard for simulations of helical scan mode when including the ellipses determined from Scout images and the resized nearest neighbor extrapolate images are shown in Figures 5.18 and 5.19

Comparing the two image extrapolation methods based on Scout images, the one using the ellipses method performed better than the resized nearest neighbor. One explanation is that the resized nearest neighbor method introduces some dislocation of the patient anatomy and results in different scatter conditions compare to the real patient anatomy. Dose cal-

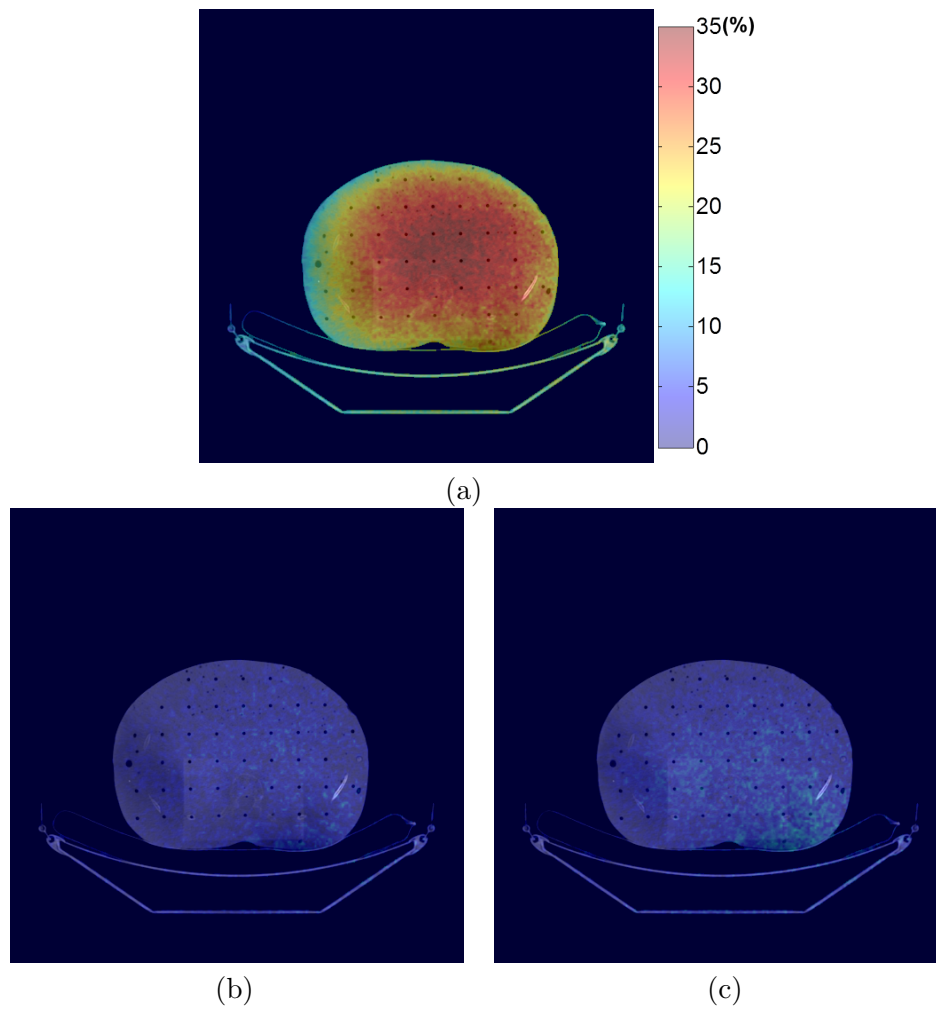


Figure 5.14: Dose difference (%) on the inferior slice of the chest scan (pelvic) compared to using whole-body Rando CT images. Monte Carlo simulations were performed for a helical scan mode using (a) chest CT images; (b) chest CT images with extrapolated images by stacking the nearest neighbor; and (c) chest CT images with extrapolated images by linear extrapolation of 5 slices on the edge.

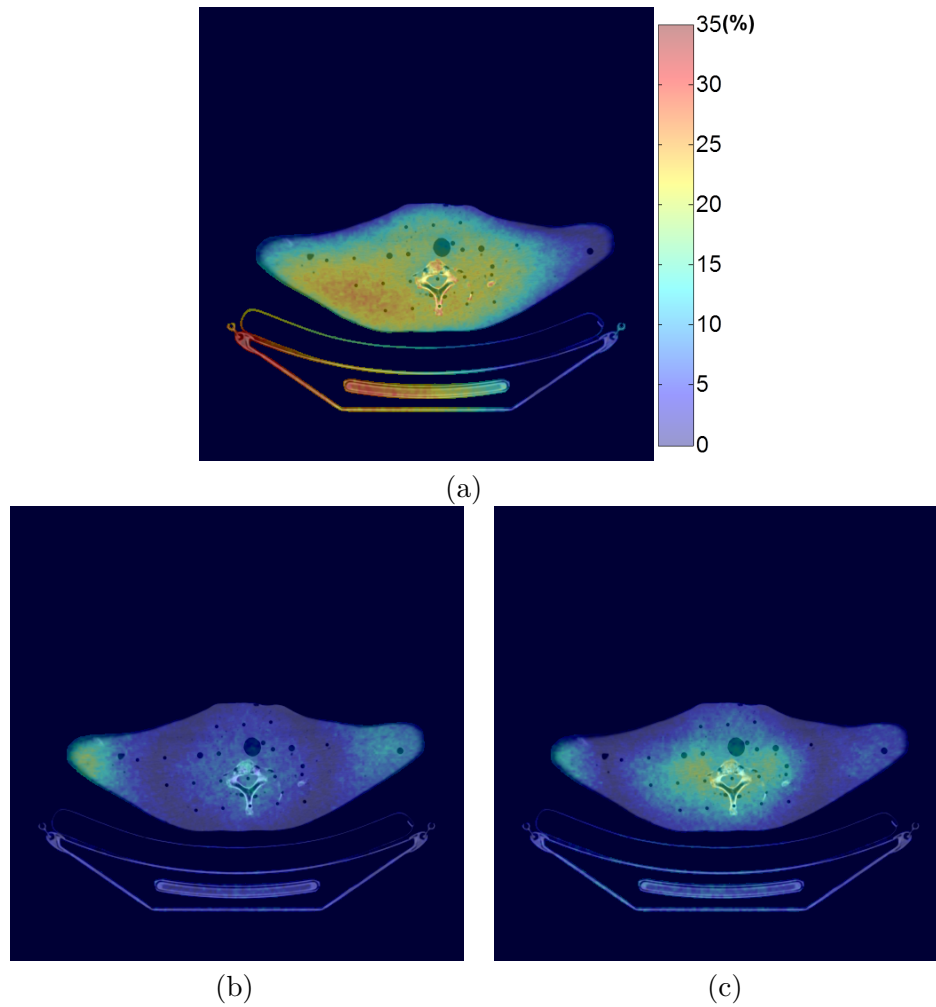


Figure 5.15: Dose difference (%) on the superior slice of the chest scan (shoulder) compared to using whole body Rando CT images. Monte Carlo simulations were performed for a helical scan mode using (a) chest CT images; (b) chest CT images with extrapolated images by stacking the nearest neighbor; and (c) chest CT images with extrapolated images by linear extrapolation of 5 slices on the edge.

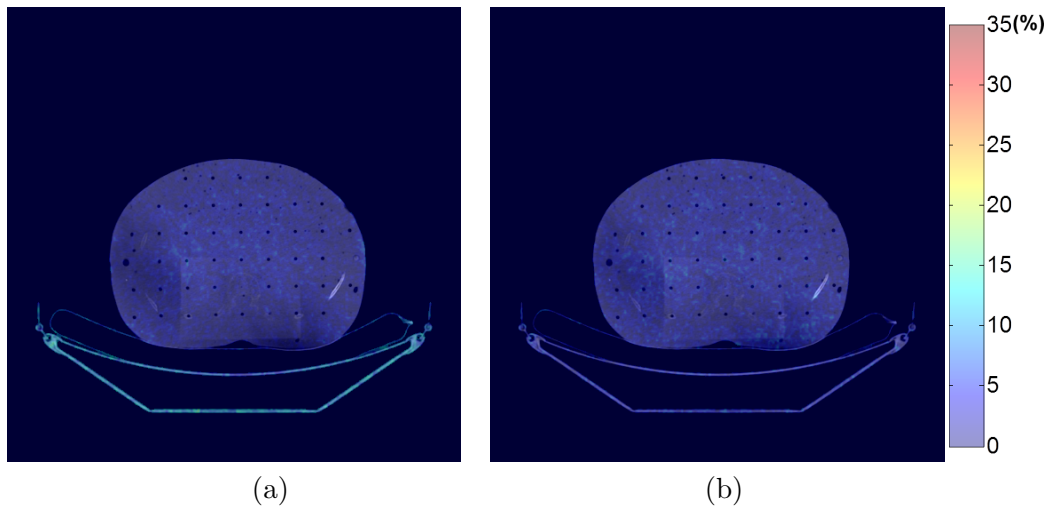


Figure 5.16: Dose difference (%) on the inferior slice of the chest scan (pelvic) compared to using whole-body Rando CT images. Monte Carlo simulations were performed for a step-shoot scan mode using (a) chest CT images plus the ellipses determined from Scout images and (b) chest CT images plus the resized nearest neighbor extrapolated images.

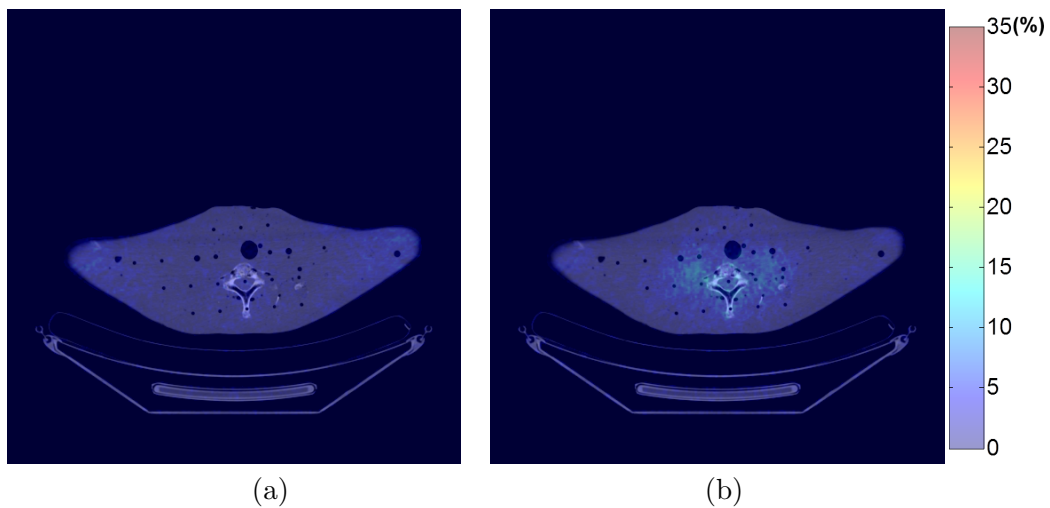


Figure 5.17: Dose difference (%) on the superior slice of the chest scan (shoulder) compared to using whole-body Rando CT images. Monte Carlo simulations were performed for a step-shoot scan mode using (a) chest CT images plus the ellipses determined from Scout images and (b) chest CT images plus the resized nearest neighbor extrapolated images.

culations using the ellipses determined from the Scout images to generate the extrapolated region gave a dose distribution that agrees well with the gold standard, with some discrepancies in small bony regions. This is due to the fact that only water was assigned to the ellipses adjacent to the scanned region, and the attenuation difference between water and bone results in different scatter interactions to the bony structures. Simply using the ellipses determined from the Scout images gave a more accurate dose calculation within the scanned region compared to using just chest images, except for in the vicinity of bony structures.

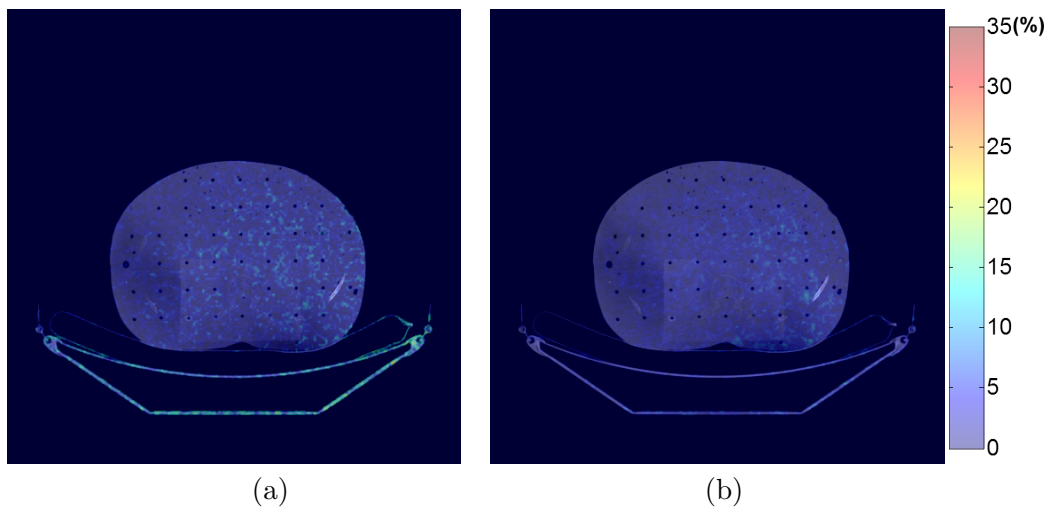


Figure 5.18: Dose difference (%) on the bottom slice of the chest scan (pelvic) compared to using whole body Rando CT images. Monte Carlo simulations were performed for a helical scan mode. (a) using chest CT images plus the Scout-images-determined ellipses ; (b) using chest CT images plus the extrapolated images by resized nearest neighbor.

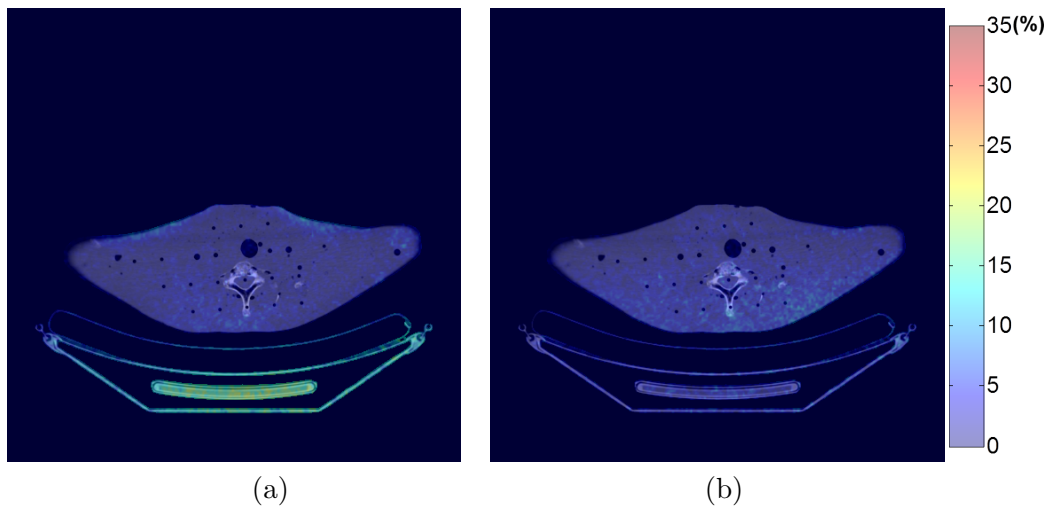


Figure 5.19: Dose difference (%) on the superior slice of the chest scan (shoulder) compared to using whole body Rando CT images. Monte Carlo simulations were performed for a helical scan mode. (a) using chest CT images plus the Scout-images-determined ellipses ; (b) using chest CT images plus the extrapolated images by resized nearest neighbor.

5.3 Summary of image extrapolations

The cylindrical phantom study demonstrated that dose calculations made without a scatter region added to the scanned region can produce a 25% underestimation of the dose to the patient, and that a scatter region with a length of 40 mm was required to provide sufficient scatter to the scanned region.

Based on the anthropomorphic phantom study, four different image extrapolation methods were proposed and compared in this work. For both the step-shoot scan mode and helical scan mode, all four of the extrapolation methods improved the dose calculation accuracy compared to the calculation without a scatter region. The linear extrapolation method produced the largest error since the human anatomy does not change linearly along the z direction. In addition to using the image slices on the edges of the existing CT images, AP and lateral Scout images were used to perform image extrapolation. Scout images are used as a localizer for CT imaging and are available immediately. By using the Scout images to

perform image extrapolation, the dose calculation accuracy under both the step-shoot scan mode and helical scan mode was greatly improved. The image extrapolation method using the ellipses determined from the Scout images performed better than the resized nearest neighbor method.

The image extrapolation methods proposed in this work are easy to perform and could be implemented in Monte Carlo CT dose calculations for patient-specific CT dose determinations and could help to improve the dose calculation accuracy. Based on the results shown in this chapter, it is recommended to include an additional scatter region appended to the ends of the scanned region for Monte Carlo dose calculations to accurately approximate full-scatter conditions. Both the nearest neighbor stacking and the ellipses determined from Scout images are good candidates for performing the image extrapolations.

Chapter 6

Clinical studies on patient CT dose

Using the established and verified Monte Carlo model for the CT scanner, this chapter presents two clinical studies for patient-specific CT dose calculations based on patient CT images. Comparisons were performed between Monte-Carlo-based patient-specific organ dose calculations and conventional dose metrics, including $CTDI_{vol}$ and DLP, effective dose, and the AAPM TG-204 recommended SSDE methods.

6.1 Study design

Patient-specific dose calculations were performed using the patient's diagnostic CT images. Anonymized patient CT images were obtained using a protocol approved by the Institutional Review Board (IRB) with the reference number of 2010-0310.

There are several technological strategies commonly used in modern CT scanners to improve dose efficiency. One common method to optimize radiation dose from CT scans is to adjust the x-ray tube current using weight- or size- based protocols. An example is automatic exposure control (AEC), which automatically modulates the tube current to accommodate differences in attenuation due to patient anatomy, shape and size. The tube current may be modulated as a function of projection angle (angular modulation), longi-

tudinal location along the patient (z-modulation) or both. The AEC trade name for GE CT scanners is “Auto mA” for z-modulation and “Smart mA” for angular modulation [Yu et al., 2009].

At the University of Wisconsin Hospital and Clinics, (UWHC, Madison, WI), Auto mA and smart mA techniques are commonly adopted for patient diagnostic CT scans performed on GE CT scanners. However, since the mA modulation technique is beyond the scope of this work, constant mA was simulated following the constant mA scan protocols for different scan regions in the CT department at the UWHC. The $CTDI_{vol}$ and DLP, effective dose, SSDE, and Monte-Carlo-based organ doses were all determined based on the constant mAs scan parameters.

6.1.1 $CTDI_{vol}$ and DLP determinations

To obtain the $CTDI_{vol}$ and DLPs corresponding to the simulated scan parameters, phantom scans were performed based on the constant mA scan protocols for different scan regions. For the constant mA scan protocols, the scanner output is independent of the scanning objects. Therefore, the $CTDI_{vol}$ values for phantom scans and patient scans using the same constant mA protocol should be the same. In this work, a GE performance phantom (GE Healthcare, Waukesha, WI) was scanned to obtain the scanner-reported $CTDI_{vol}$ corresponding to the scan parameters in the Monte Carlo simulations.

The DLP by definition is the product of $CTDI_{vol}$ and scan length. The scan length for each patient was determined by the reconstruction thickness and the number of the slices of the patient CT image set. The DLP for each patient was calculated by multiplying the scan length by the $CTDI_{vol}$ reported from the phantom scans.

6.1.2 Effective dose determinations

Effective dose was determined by multiplying the $CTDI_{vol}$ by k factors for different scan regions. The k factors were obtained from the European Commission (EC) and National Radiological Protection Board (NRPB) for chest and abdomen/pelvis CT scans [Bongartz et al., 2004, Shrimpton et al., 2005].

6.1.3 SSDE determinations

To calculate SSDE values, both the $CTDI_{vol}$ and the patient size information were required. AAPM TG-204 suggests four different ways to determine patient size, the lateral dimension (LAT), the anterior-posterior dimension (AP), the (AP+LAT) dimension, and the effective diameter. The LAT and AP can be measured on the lateral and AP CT radiograph or CT images using digital clippers. TG-204 provides corresponding look-up tables for conversion factors for each of the four patient-size parameters. In this work, the effective diameter was chosen to represent patient size and the conversion factors were looked up from Table 1D in TG-204. AP and lateral dimensions were measured from patient CT images and the effective diameters were calculated using the following formula:

$$\text{Effective Diameter} = \sqrt{LAT \times AP}. \quad (6.1)$$

Linear interpolations of the size-specific correction factors in the table were performed based on the patient size.

However, it is not clearly defined in TG-204 which location in a patient CT volume should be used to measure effective diameter. As the patient outline changes longitudinally, the effective diameter varies within the patient. In this work, size measurements were performed every five slices (6.25 cm) along the superior-inferior direction. The effective diameters for

each measured slice were calculated, and the average value was used to represent the size for this patient.

6.1.4 Monte-Carlo-based organ dose determinations

6.1.4.1 Image processing

Before calculating patient doses, image extrapolations were performed. The method of generating ellipses described in Chapter 5 was applied here. 40 mm long extrapolated regions were generated on each end of the CT image set. The material of water was assigned to the ellipses.

An image processing program, ImageJ, developed at the National Institutes of Health, was used in this work for organ contouring on the patient CT images. The heart was contoured for chest scan patients (clinical study 1). The left and right kidneys were contoured for the pelvic patients (clinical study 2). The contour information for each axial slice of the CT images was saved separately with coordinate information for the organ of interest. Lung, bony structures and soft tissue were assigned based on thresholding CT numbers for the regions not being contoured as organs of interest. In other words, if a voxel was not assigned to any of the organs of interest, it was assigned as lung (CT numbers of -700 HU to -300 HU), soft tissue (CT numbers of -300 HU to 300 HU), bony structure (CT numbers larger than 300 HU), or air (CT numbers less than -700 HU) based on the CT number of this voxel. For each slice, a map of organ/region localization was generated based on this methodology.

Some of the studies involved a contrast agent for diagnostic purposes. The CT number for a contrast agent is generally high and would affect the accuracy of dose calculations. Density overriding was generated for the patient images with contrast present. Since the CT numbers for bony structure and contrast agent were similar, manual contours of the contrast region were performed using ImageJ program. The contrast contours were saved

for each slice of the CT images. The CT number for voxels within the contoured-contrast region were changed to 1000 HU for water in the DICOM files.

The final processed images included the extrapolated regions for each patient and density overriding for patients with contrast injection. These processed data were imported into the GMctdospp program for dose calculations. Scan parameters were chosen in this program (See Sections 6.2.2 and 6.3.2 for each case).

After the 3-D dose distributions (in mGy/starting particle) within the scan region were calculated, the mAs-to-dose conversion factor was applied to compute dose (in mGy) at the mAs level studied. For each organ, the mean dose was calculated based on the 3-D dose distribution and the organ/region map.

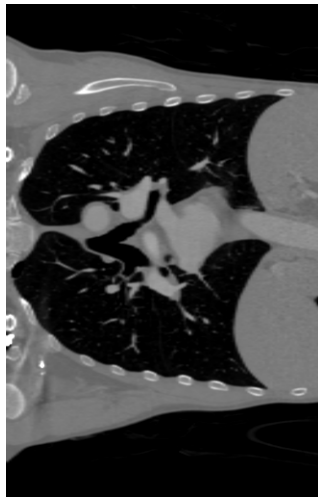
6.2 Clinical study case 1

In this clinical study, the scenario in which a group of patients have similar anatomical structure but different sizes was evaluated. This is the situation for which SSDE was designed to correct the impact on dose from patient sizes. Comparisons of patient CT dose from the current CT dosimetry methods and the patient-specific MC dose calculation proposed in this thesis work were made.

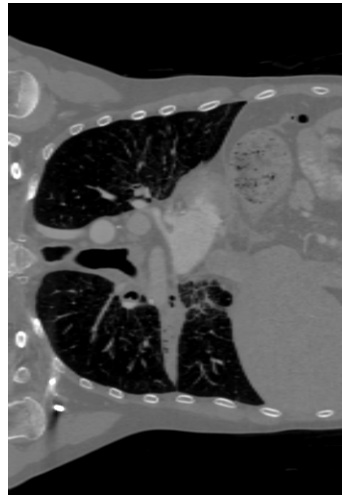
6.2.1 CT images and patient size measurement

Three sets of patient CT images from chest CT scans were included in this study. The coronal views of the patients (a), (b), and (c) are shown in Figure 6.1. All images were acquired with intravenous (IV) injection of contrast.

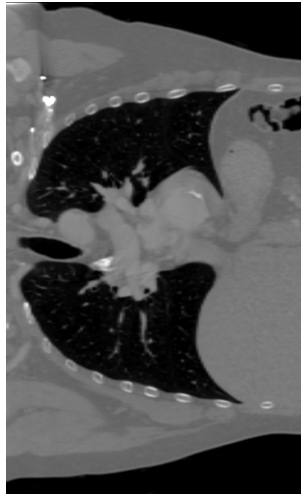
The longitudinally averaged effective diameters and the scan lengths for the three patients in this study are shown in Table 6.2.



(a)



(b)



(c)

Table 6.1: Coronal views of the patient CT images for the three patients.

Table 6.2: Averaged effective diameters and scan lengths for the three patients in clinical study 1.

	Effective diameter (cm)	Scan length (cm)
Patient (a)	29.4	32
Patient (b)	30.4	34
Patient (c)	37.0	30

6.2.2 Scan parameters for Monte Carlo simulations

The UWHC chest CT scan protocol using constant mA was simulated in the Monte Carlo simulation program, which included a helical scan mode, a 40 mm beam width, a pitch of 0.984:1, a tube voltage of 120 kVp, a tube current of 150 mA, and a 0.5 s per rotation speed (150 mAs). The large-body bowtie filter was in the beam. The beam width and pitch were selected from the GMctdospp program. The spectrum and large-body bowtie filter determined and verified in Chapter 3 were included in this Monte Carlo model.

6.2.3 Results

6.2.3.1 Dose determinations following current CT dosimetry

The $CTDI_{vol}$ corresponding to the scan parameters used for this study was reported as 5.88 mGy from the GE HD750 CT scanner. This value was specified to be valid for the 32 cm diameter CT dose phantom (adult body CTDI) on the CT scanner. Since $CTDI_{vol}$ is an indicator for scanner output and only depends on the scan parameters, the values of $CTDI_{vol}$ for these three patients were the same.

DLP was determined by taking the product of $CTDI_{vol}$ and the scan lengths for each of the three patients. The DLPs were 188.16 mGy·cm, 199.92 mGy·cm, and 176.40 mGy·cm, for patient (a), (b), and (c), respectively. Since $CTDI_{vol}$ was the same, the differences of DLP between the three patients were due to their different scan lengths. Compared to

patient (a), 5.8% and 8% differences in the DLPs were found for patient (b) and patient (c), respectively.

Effective dose for each patient was determined based on their DLP and the looked-up k factors. k factors are only dependent on the scan region and all of the three patients were chest scan patients, so the k factors were the same for each patient (0.014 for chest scan). As a result, the effective dose followed the same trend as the DLPs for the three patients: 5.8% and 8% differences for patient (b) and (c), respectively, compared to patient (a). Similar to the DLP results, the differences in effective dose among the three patients were also due to their different scan lengths.

The effective diameters averaged along the longitudinal direction for the three patients were 29.4 cm, 30.4 cm and 37.0 cm, respectively. The size-specific dose correction factors corresponding to these values were 1.26, 1.214 and 0.97, respectively, for the three patients based on AAPM TG-204. These correction factors were applied to CTDI_{vol} to obtain the SSDEs for the three patients. It should be noted that SSDE does not include the effect of scan length. The largest discrepancy (26%) was between patient (a) and patient (c) and was caused by the large difference in effective diameters between the two patients. The results agrees with the AAPM TG-204 results that the patient dose decreased with increasing patient size.

The CTDI_{vol} , DLP, effective dose and SSDE for each patient were summarized in Table 6.3. To compare the dose differences among the three patients, all of these dose-related values were normalized to patient (a). The normalized dose values are shown in Table 6.4 and plotted in Figure 6.1. Using current CT dosimetry, DLP and effective dose only reflected the difference in scan lengths for different patients, while SSDE results estimated the dose discrepancy due to patient size.

Table 6.3: Patient CT doses determined from current CT dosimetry.

	Current CT dosimetry			
	CTDI _{vol} (mGy)	DLP (mGy·cm)	Effective dose (mSv)	SSDE (mGy)
Patient (a)	5.88	188.16	2.63	7.41
Patient (b)	5.88	199.92	2.80	7.14
Patient (c)	5.88	176.40	2.47	5.59

Table 6.4: Patient CT doses determined from current CT dosimetry. Values are normalized to patient (a).

	CTDI _{vol}	DLP	Effective dose	SSDE
Patient (a)	1	1.000	1.000	1.000
Patient (b)	1	1.063	0.963	1.063
Patient (c)	1	0.938	0.754	0.938

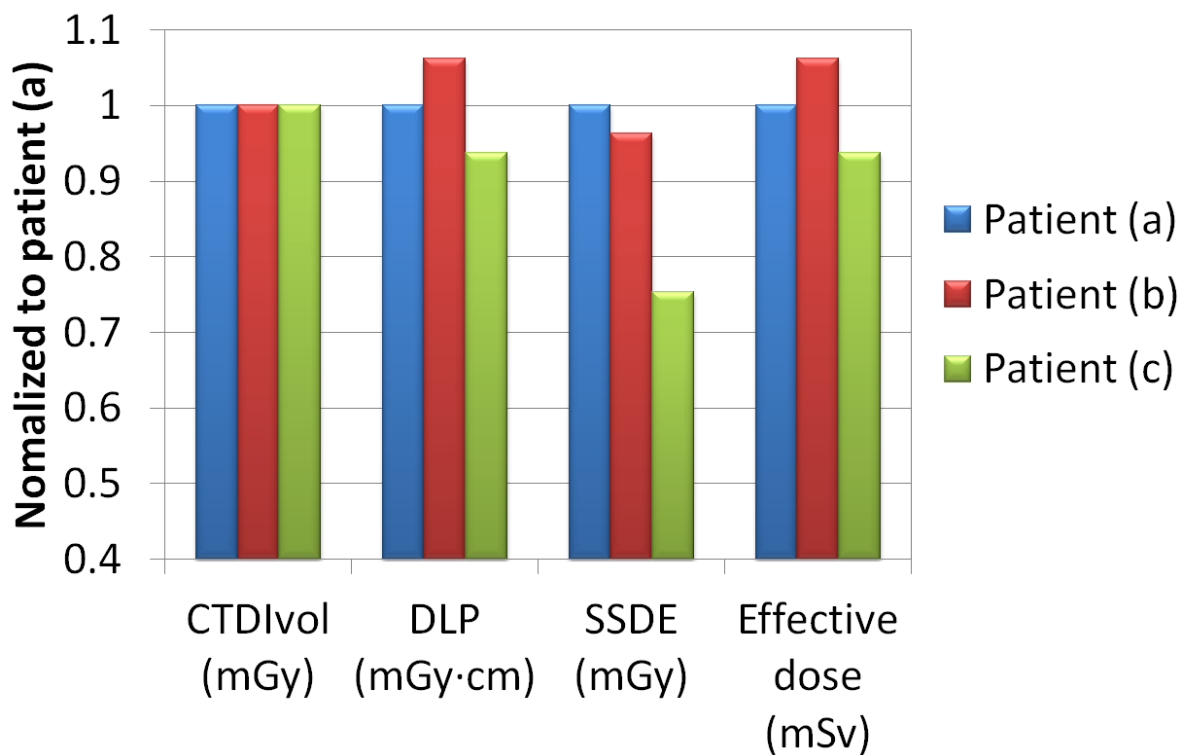


Figure 6.1: Determined dose-related term normalized to patient (a) from current CT dosimetry.

6.2.3.2 Monte-Carlo-based dose determinations

The mean doses for heart, lung, soft tissue, and bony structures were calculated with the GMctdospp program for each patient. The results are shown in Table 6.5. For all of the four different organs or regions, the dose values agreed with the results of AAPM TG-204 which indicated that organ dose decreases with patient size. The dose values were normalized to patient (a). The normalized dose values are shown in Table 6.6 and plotted in Figure 6.2. For different organs and regions, the dose differences among the three patients were different. The discrepancies between patient (a) and patient (c) who had the smallest and largest effective diameters were 23.4%, 18.1%, 21.1%, and 28.2% for heart, lung, soft tissue and bony structures, respectively.

Table 6.5: Patient CT doses determined with Monte Carlo simulations.

	Heart (mGy)	Lung (mGy)	Soft tissue (mGy)	Bony structure (mGy)
Patient (a)	1.24	1.16	1.14	3.73
Patient (b)	1.15	1.08	1.05	3.16
Patient (c)	0.09	0.95	0.90	2.68

Table 6.6: Patient CT doses determined with Monte Carlo simulations. Values are normalized to patient (a).

	Heart	Lung	Soft tissue	Bony structure
Patient (a)	1	1	1	1
Patient (b)	0.927	0.931	0.921	0.847
Patient (c)	0.766	0.819	0.789	0.718

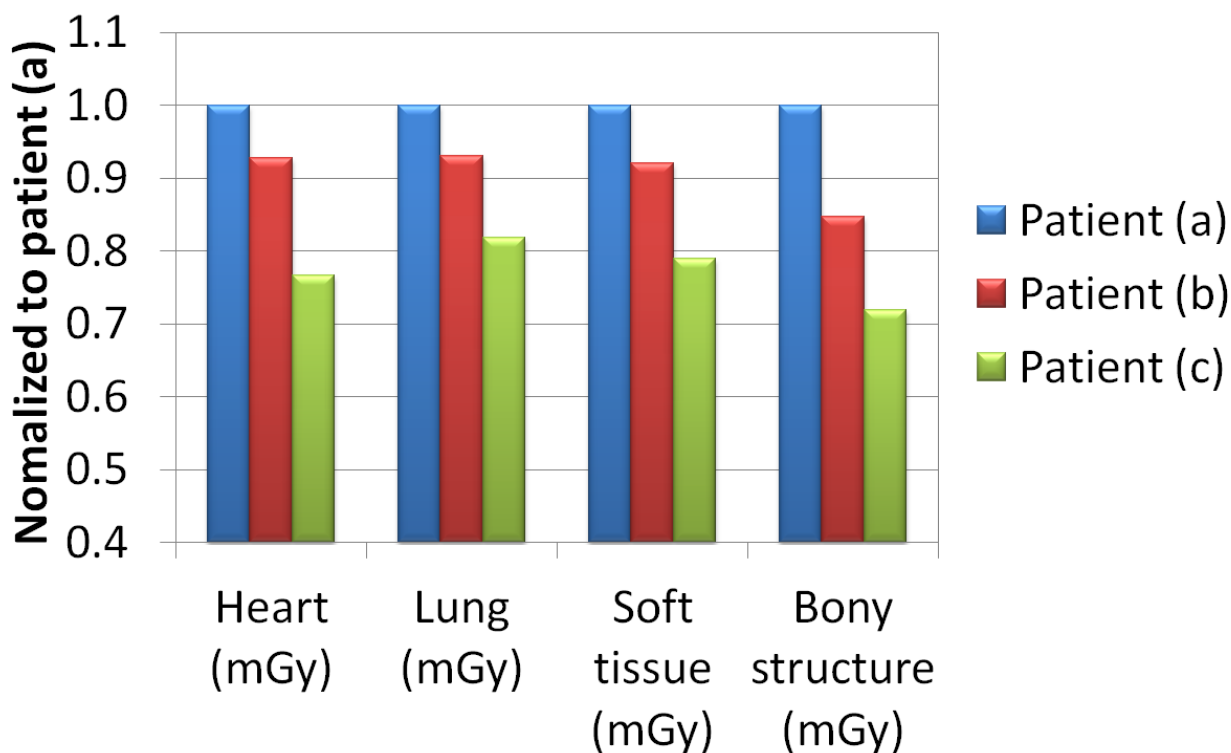


Figure 6.2: Determined dose-related term normalized to patient (a) from current CT dosimetry.

6.2.3.3 Summary for clinical study 1

In this clinical study, CT dose was determined by the current CT dosimetry and the Monte-Carlo-based dose calculation technique proposed in this work. The three chest scan patients studied in this work represented patients with similar anatomy, different sizes, and different scan lengths. One single set of scan parameters was applied for each of the dose calculation methods. $CTDI_{vol}$ failed to predict any dose difference between patients, since it is only dependent on scan parameters. The discrepancies of DLPs and effective doses among the three patients were related to the different scan lengths only. The SSDE method was the only current CT dosimetry technique which gave patient-size-specific dose estimates. The SSDE values agreed with the trend of Monte-Carlo-calculated organ doses that patient CT

dose decreases with increasing patient size, however, the SSDE method does not provide organ-specific dose information.

6.3 Clinical study case 2

6.3.1 CT images and patient size measurement

Two patient CT image sets of the abdomen/pelvis region were included in this study. One of the CT image sets was acquired using an abdomen/pelvis with IV contrast protocol and the other was acquired using a CT colonography (CTC) protocol. CTC, also called “virtual colonoscopy” is an imaging method for detection of colon polyps and cancer [Rex et al., 1999]. Before the CTC scan, the colon is filled with carbon dioxide or air via a tube introduced into the rectum. This results in a different inner-anatomical structure than the normal abdomen/pelvis CT scans. Axial CT images of the patients are shown in Figure 6.3. It is observed that the amount of gas in the colon was much higher in the CTC scan than in the abdomen/pelvis scan.

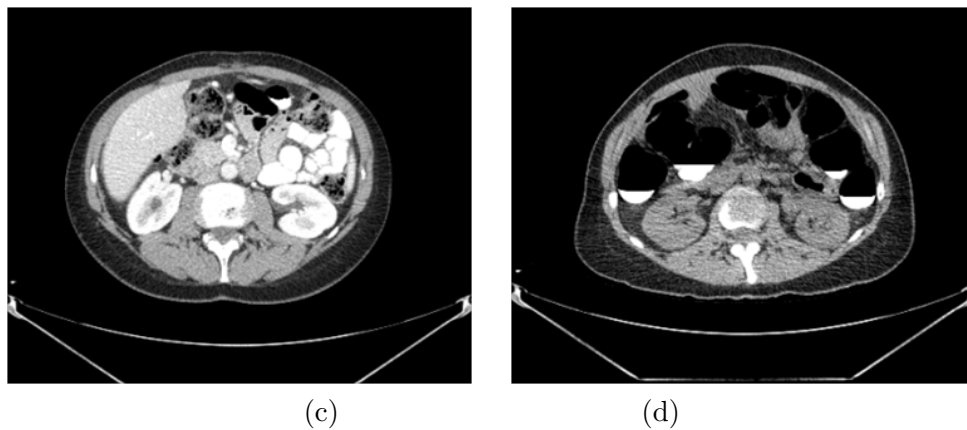


Figure 6.3: Axial CT images of abdomen/pelvis patient (left) and CTC patient (right).

The effective diameters averaged along the longitudinal dimension of the measurements of patient dimensions were similar (23.6 cm). The scan lengths of the two patients were both 38 cm, as shown in Table 6.7.

Table 6.7: Averaged effective diameters and scan lengths for the two patients in clinical study 2.

	Effective diameter (cm)	Scan length (cm)
Patient (d)	23.6	38
Patient (e)	23.6	38

6.3.2 Scan parameters for Monte Carlo simulations

The UWHC abdomen/pelvis CT scan protocol using constant mA was simulated in the Monte Carlo simulation program. The protocol and simulations included a helical scan mode, a 40 mm beam width, a pitch of 0.984:1, a tube voltage of 120 kVp, a tube current of 240 mA, and a 0.5 s per rotation speed (120 mAs). The large-body bowtie filter was in the beam. The beam width and pitch were selected from the GMctdospp program. The spectrum and large-body bowtie filter determined and verified in Chapter 3 were included in this Monte Carlo model.

6.3.3 Results

6.3.3.1 Dose determinations following current CT dosimetry

Since $CTDI_{vol}$ is only dependent on scan parameters, the $CTDI_{vol}$ s for these two patients were the same. The $CTDI_{vol}$ corresponding to the scan parameters used for this study was reported as 9.49 mGy from the GE HD750 CT scanner, and was specified to be valid for the 32 cm diameter CT dose phantom.

Both patients had the same scan length, and therefore, the DLP values for the two patients were the same. The DLP was 360.62 mGy·cm.

The k factor for abdomen/pelvic scans is 0.015 from EC and NRPB [Bongartz et al., 2004, Shrimpton et al., 2005]. By applying this factor to the DLP, the effective dose for each of the two patients were determined to be 5.41 mSv.

From AAPM TG-204, the size-specific dose correction factor corresponding to 23.6 cm is 1.554. The SSDEs for the two patients were both determined to be 14.75 mGy.

The effective diameter, CTDI_{vol} , DLP, effective dose and SSDE for both patients were the same and are summarized in Table 6.8. It is seen that all of the current CT dosimetry methods determined an equivalent dose level for these two patients, due to the same scan parameters, similar outer dimensions, and same scan lengths.

Table 6.8: Patient CT doses determined from current CT dosimetry.

	Current CT dosimetry			
	CTDI_{vol} (mGy)	DLP (mGy·cm)	Effective dose (mSv)	SSDE (mGy)
Patient (d)	9.49	360.62	5.41	14.75
Patient (e)	9.49	360.62	5.41	14.75

6.3.3.2 Monte-Carlo-based dose determinations

The Monte-Carlo-simulated doses to the left kidney, right kidney, soft tissue and bony structure are listed in Table 6.9. The dose differences between the two patients were 6.4%, 12.6%, 7.8%, and 5.3% for each of the organs and regions, respectively, shown in Table 6.10. The dose differences were caused by the different internal anatomy of each patient. Patient (e) (CTC patient) had a larger amount of air in the pelvic region which resulted in less mass and a higher relative average dose.

Table 6.9: Patient CT doses determined with Monte Carlo simulations.

	Left kidney (mGy)	Right kidney (mGy)	Soft tissue (mGy)	Bony structure (mGy)
Patient (d)	2.09	2.02	1.71	5.19
Patient (e)	2.22	2.28	1.81	5.60

Table 6.10: Differences of Monte-Carlo-calculated organ dose between the two patients.

	Left kidney	Right kidney	Soft tissue	Bony structure
Dose difference (%)	6.4	12.6	7.8	5.3

6.3.3.3 Summary for clinical study 2

In this clinical study, CT dose to a CTC patient and from a normal abdomen/pelvic scan patient were determined using current CT dosimetry methods and Monte-Carlo-based dose calculations. All of the current CT dose metrics failed to show the dose differences between the two patients, because all of the factors the current CT dosimetry metrics related parameters, including scan parameters (affecting $CTDI_{vol}$), scan lengths (affecting DLP), scan regions (affecting k factors for effective dose determination), and patient outer dimensions (affecting SSDE) were the same for the two patients. The patient CT dose is also dependent on the internal anatomy. This effect was only reflected by the Monte-Carlo based dose determination method. The Monte-Carlo-based dose calculation technique shows an improvement for patient-specific CT dose determination compared to the current CT dosimetry methods.

6.4 Uncertainty analysis

The uncertainties related to the Monte-Carlo calculated organ dose are listed in Table 6.11. The Monte Carlo statistical uncertainty (1.38%) was from the GMctdospp and is a type A uncertainty. A single organ was contoured 5 times and an uncertainty related to the reproducibility of organ contouring was performed. A standard deviation of mean volume of this organ was determined to be 3.50% and this value is considered as type A uncertainty. Since the source spectrum was determined based on HVL measurements, the uncertainty associated with the source spectrum was obtained from the variation in HVL measurements. The actual bowtie filter information was not available. A difference between an estimated

Table 6.11: Uncertainties related to Monte-Carlo calculated organ dose.

Parameter	Relative Standard Uncertainty (%)	
	Type A	Type B
Monte Carlo statistics	1.38	
Contour reproducibility	3.50	
HVL measurements	1.28	
Bowtie filter determination		5.45
Combined uncertainty	3.97	5.45
Total uncertainty (k=1)		6.7
Expanded uncertainty (k=2)		13.4

bowtie filter using similar methodology as this work and the actual bowtie filter was determined to be 5.45% for 120 kVp scan parameters by Turner et al [2009]. This value is considered as type B uncertainty related to bowtie filter determination for this work. Therefore the total uncertainty for organ dose calculations is 6.7% at $k = 1$ (66% confidence level) and 13.4% at $k = 2$ (95% confidence level).

Chapter 7

Conclusions and future work

7.1 Conclusions

In this work, a clinically applicable, Monte-Carlo-based CT dose calculation technique has been established and verified. This technique uses patient CT images and scanner characterizations to provide patient-specific organ dose information.

7.1.1 Monte Carlo model establishment and verification

An EGSnrc-based Monte Carlo simulation program, GMctdospp was cross validated with MCNP5 and used to perform dose calculations. Methodologies for determining two essential parts of the CT scanner model, the source spectrum and bowtie filter, were proposed. Based on the methodologies proposed in this work, only half value layer measurements and the flux distribution from an in-air CT scan are required for scanner-specific Monte Carlo model establishment.

To verify the determined source spectrum and bowtie filter, the relative output at different points in a cylindrical phantom was measured and compared with Monte Carlo simulated results. The root mean square deviation between the relative source output measurements and simulations was 2.18%, which verified the accuracy of the source spectrum and bowtie-

filter geometry determined in this work. The method of using relative output for beam quality verification was shown to be sensitive to different spectra by using a sensitivity test, which compared the simulated relative output using four 120 kVp spectra with different half-value layers.

7.1.2 Determination and verification of mAs-to-dose conversion factor

A linear relationship between CT dose and scanner output (mAs) was shown with an in-phantom ionization chamber measurement. Since the calculated dose from Monte Carlo simulations is normalized per starting particle, and the patient dose is linearly related to the scanner output, mAs, the determination of mAs-to-dose conversion factor was necessary. The mAs-to-dose conversion factor was determined with the in-air dose measurements using an Exradin A1SL ionization chamber, and Monte-Carlo-simulated dose per particle in the active volume of this chamber. To verify the ionization-chamber-determined mAs-to-dose conversion factor, another type of dosimeter, TLD, was used to perform z-direction dose profile measurements. Applying the determined mAs-to-dose conversion factor to Monte-Carlo-simulated z-direction dose profile showed less than 3.9% difference compared to TLD measurements.

7.1.3 Image extrapolations

Using patient CT images for dose calculations provides patient-specific information within the scanned region. However, the lack of regions adjacent to the scanned region can cause dose underestimation due to the lack of scatter material. A mathematical cylindrical phantom study demonstrated that up to 25% of dose underestimation was shown at the edge of the scan region due to the lack of scatter, and a scatter region with a length of 40 mm was required to approximate the full-scatter condition.

Based on the anthropomorphic phantom study, four different image extrapolation methods were proposed and compared in this work. Dose calculation accuracy was significantly improved by including the extrapolated regions to approximate the scatter conditions. The nearest neighbor stacking and the ellipses determined from Scout images are good techniques to generate the extrapolated images as they produced the most accurate dose calculations within the region of interest.

7.1.4 Clinical studies

Two clinical case studies were designed for patient-specific CT dose calculations based on patient CT images and compared with the current CT dosimetry. Clinical study 1 evaluated the proposed patient-specific CT dose calculation against current CT dosimetry in a group of patients with similar anatomical structures but different external sizes. SSDE method was the only current CT dosimetry method which gave patient-size-specific dose estimates. The SSDE values agreed with the trend found for Monte-Carlo-calculated organ doses that patient CT dose decreases with patient size, however, the SSDE method does not provide organ-specific dose information. Clinical study 2 compared the CT doses of two patients with similar outer dimensions but different internal anatomies. All current CT dose metrics failed to show the dose differences between the two patients. The effect of differing anatomical information on dose was only reflected by the Monte-Carlo-based organ dose calculations.

7.2 Future work

7.2.1 CT dose calculations for CT-based screenings

The use of CT for mass screening of asymptomatic patients is a recent innovation. Four primary applications have been suggested for CT-based screening: screening for colon polyps (CTC, or virtual colonoscopy), screening for early-stage lung cancer in smokers and ex-

smokers, screening for cardiac disease, and full-body screening. All of these applications are relatively new, and the benefits of the CT-based screening procedures should be evaluated with the related potential risks associated with the x-ray radiation involved. Accurate dose estimation becomes important for CT-screening patients, since a large portion of the patients are relatively young, healthy, and have longer remaining life spans [Hall and Brenner, 2008].

There has been some work on risk estimation for CT-screening procedures based on the data of the atomic bomb survivors. While an individual's risk is associated with the scan parameters for a specific patient and the patient specific anatomy information, very few studies on individual dose tracking or risk estimation based on patient-specific CT dose have been reported. Studies on patient-specific CT dose, especially to organs at risk are needed to enable the professional societies to make future suggestions on whether these kinds of screening procedures should be recommended as routine procedures.

With the methodology developed in this work, and the CT images obtained from screening patients, the proposed Monte-Carlo-based organ dose calculation technique could be used for dose tracking purposes. With the collaboration of radiologists and radiobiologists, working on risk tracking and benefit/risk balance estimations could be further investigated.

7.2.2 Modeling for mA modulated CT scans

Currently, all the major manufacturers of CT scanners offer automatic tube current modulation (mA modulation) for dose reduction purposes. mA modulation techniques enable automatic adjustment of the tube current in the $x - y$ plane (angular modulation) or along the z -axis (z -axis modulation) according to the size and attenuation characteristics of the body part being scanned to achieve constant CT image quality with lower radiation exposures. Figure 7.1 illustrates of the concept of angular modulation, in which the tube current is varied as the x-ray tube rotates around the patient. Figure 7.2 illustrates the concept of longitudinal mA modulation with variation of the tube current along the z -axis.

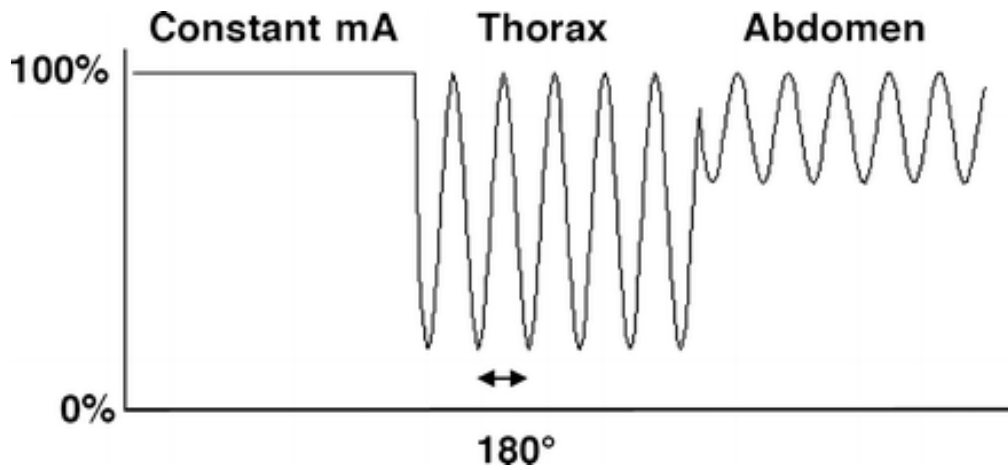


Figure 7.1: Illustration of the concept of angular mA modulation, in which the tube current (mA) (vertical axis) is varied as the x-ray tube rotates around the patient (horizontal axis). Adopted from McCollough et al., 2006.

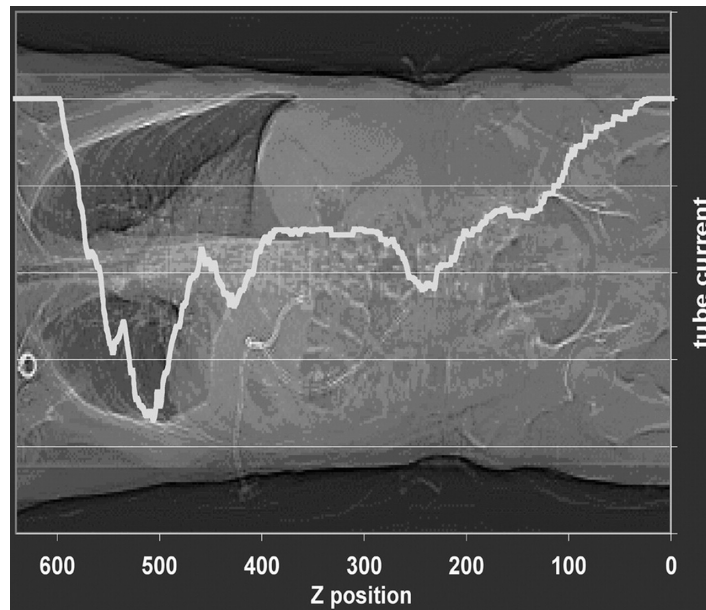


Figure 7.2: Graph of tube current (in mA) superimposed on a CT projection radiograph that illustrates the concept of z -axis modulation, with variation of the tube current along the z -axis. The curve is determined by using attenuation data from the CT projection radiograph and a manufacturer-specific algorithm. Adopted from McCollough et al., 2006.

This work only used constant mA simulations in the Monte Carlo dose calculation model. It has been demonstrated in this thesis (Chapter 3) that the dose has a linear relationship with the scanner output, mA or mAs. For mA modulation, once the tube current value at each longitudinal direction and each projection is available, an mA-related weighting matrix could be applied to the 3-D dose distribution for mA modulated CT dose determination. Determination of mA-modulated CT dose would be a future improvement to better represent actual patient CT scans.

7.2.3 In-phantom dose calibrations of TLDs for CT sources

This work focuses on Monte Carlo simulations for CT dose determinations. Verification of the simulations were performed with ionization chamber measurements and TLD measurements. Calibrations of an A1SL ionization chamber and a PS-033 ionization chamber performed at the UWADCL demonstrated that these ionization chambers have a flat response for a variety of kilovoltage x-ray beams. However, TLD energy response for x-ray beams from CT, especially when TLDs are placed at different depths in phantom, has not been discussed in this work.

For TLD calibrations in this work, two beam qualities similar to x-ray beams from the CT scanner were used to perform air-kerma calibration in air. The air-kerma-to-dose conversion factor was obtained from Monte Carlo simulations. However, the beam qualities for calibration are close but not exactly the same as those of the CT source, and the spectrum could change with depth when attenuated by phantom materials. If the spectrum changes significantly enough, the response of the TLDs could change due to their energy dependence, and the accuracy of the dose determination by TLD could be reduced. Ideally, the TLD calibration should be performed on the beam of interest, which is the clinical CT beam in this work, and at a depth in the phantom similar to the dose measurement conditions. With



Figure 7.3: Photograph of the custom-designed PMMA cylindrical insert for A1SL ionization chamber.

the known dose at a point in phantom measured, the dose-to-TLD calibration coefficient can be determined.

A custom-designed PMMA cylindrical insert has been manufactured specifically for A1SL chambers, as shown in Figure 7.3. This insert can be placed in a cylindrical CT dose phantom, such as the one used in this work (Chapter 4). The dose at the position of the center of the A1SL active volume can be determined with chamber measurements for a set of specific CT scan parameters. When TLDs are placed at the same location as the active volume of the ionization chamber, and the same scan parameters are used, the TLDs can be calibrated in the clinical CT beam. The corrected TLD readings ($M_{\text{TLD,corrected}}$, nC) and the chamber-determined dose ($D_{d,\text{chamber}}$, cGy) give a calibration factor ($C_{D,d}$, cGy/nC) for the TLDs that is specifically for the CT source at each measured location, (d), in a phantom, as shown in Equation 7.1.

$$C_{D,d} = \frac{D_{d,\text{chamber}}}{M_{\text{TLD,corrected}}}. \quad (7.1)$$

It should be mentioned that the dose determination with ionization chambers is challenging since the calibration of ionization chambers for kilovoltage x rays is given by air kerma or exposure. A bridge from air kerma or exposure to dose to water or tissue-equivalent phantom should be established. The AAPM TG-61 “Protocol for 40–300 kV x-ray beam

dosimetry in radiotherapy and radiobiology” [Ma et al., 2001] and the IAEA TRS-398 “Absorbed dose determination in external beam radiotherapy: An international code of practice for dosimetry based on standards of absorbed dose to water” [2004] would be referenced for the establishment of the dose to medium determination methodology of ionization chambers.

Bibliography

The AAPM Statement on Radiation Dose from Computed Tomography, in response to the Brenner and Hall NEJM article published Nov 29, 2007., November 2007.

AAPM Response in Regards to CT Radiation Dose and its Effects, December 2009.

The AAPM Statement on CT Scans Are An Important Diagnostic Tool When Used Appropriately, June 2012.

Medical Imaging in Canada, 2005.

IMV 2006 CT Market Summary Report. Des Plains, IL: IMV Medical Information Division, 2006.

URL www.impactscan.org.

URL <http://www.doseinfo-radar.com/RADARDoseRiskCalc.html>.

American Association of Physicists in Medicine. Size-Specific Dose Estimates (SSDE) in pediatric and adult body CT examinations. *AAPM Report No. 204*, 2011.

American Association of Physicists in Medicine. Comprehensive QA for radiation oncology. *AAPM Report No. 40*, 1994.

American Association of Physicists in Medicine. Protocol for clinical reference dosimetry of high energy photon and electron beams. *AAPM Report No. 51*, 1999.

- American Association of Physicists in Medicine. The measurement, reporting and management of radiation dose in CT. *AAPM Report No. 96*, 2008.
- American Association of Physicists in Medicine. Quality assurance of medical accelerators. *AAPM Report No. 142*, 2009.
- E. S. Amis, P. D. Butler, K. E. Applegate, S. B. Birnbaum, L. F. Brateman, J. M. Hevezi, F. A. Mettler, R. L. Morin, M. J. Pentecost, G. G. Smith, K. J. Strauss, and R. K. Zeman. American College of Radiology white paper on radiation dose in medicine. *J. Am. Coll. Radiol.*, 4:272–284, 2007.
- F. H. Attix. *Introduction to Radiological Physics and Radiation Dosimetry*. Wiley-VCH, Weinheim, Germany, 2004.
- B. Axelsson, J. Persliden, and P. Schuwert. Dosimetry for computed tomography examination of children. *Radiat Prot Dosim.*, 64:221–226, 1996.
- M. R. Ay and H. Zaidi. Development and validation of MCNP4C-based Monte Carlo simulator for fan- and cone-beam x-ray CT. *Phys. Med. Biol.*, 50:4863–4885, 2005.
- N. Ban, F. Takahashi, K. Sato, A. Endo, K. Ono, T. Hasegawa, T. Yoshitake, Y. Katsunuma, and M. Kai. Development of a web-based CT dose calculator: WAZA-ARI. *Radiat Prot Dosimetry*, 147:333–337, 2011.
- J. Baróa, J. Sempaub, J.M. Fernández-Vareac, and F. Salvat. PENELOPE-an algorithm for Monte-Carlo simulation of the penetration and energy-loss of electrons and positrons in matter. *Nucl. Instrum. Methods Phys. Res. B*, 100:31–46, 1995.
- G. Bongartz, S. J. Golding, and A. G. Jurik AG. *European guidelines for multislice computed tomography*. Brussels, Belgium: European Commission, 2004.
- J. M. Boone. Method for evaluating bow tie filter angle-dependent attenuation in CT: Theory and simulation results. *Med Phys*, 37:40–48, 2010.

- D. J. Brenner and E. J. Hall. Computed tomography - An increasing source of radiation exposure. *N Engl J Med*, 357:2277–2284, 2007.
- J. F. Briesmeister. MCNP-a general Monte Carlo N-particle transport code. Technical report, Los Alamos National Laboratory Report LA-12625-M, 1993.
- M. Caon, G. Bibbo, and J. Pattison. A comparison of radiation dose measured in CT dosimetry phantoms with calculations using EGS4 and voxel-based computational models. *Med. Phys*, 42:219, 1997.
- I. A. Castellano, D. R. Dance, and P. M. Evans. CT dosimetry: getting the best from the adult Cristy phantom. *Radiat Prot Dosimetry*, 114:321–325, 2005.
- C. L. Chapple, S. willis, and J. Freame. Effective dose in pediatric computed tomography. *Med Phys*, 47:107–115, 2002.
- R. Chen and S.W.S. McKeever. *Theory of Thermoluminescence and Related Phenomena*. World Scientific, 1997.
- J. A. Christner, J. M. Kofler, and C. H. McCollough. Estimating effective dose for CT using dose-length product compared with using organ doses: Consequences of adopting international commission on radiological protection publication 103 or dual-energy scanning. *AJR: American Journal of Roentgenology*, 194:881–889, 2010.
- E. Christodoulou and M. Goodsitt. ICRP-103 based gender and age-specific DLP to effective dose conversion factors (k). *Med. Phys*, 38:3876, 2011.
- J. J. DeMarco, C. H. Cagnon, D. D. Cody, D. M. Stevens, C. H. McCollough CH, J. O’Daniel, and M. F. McNitt-Gray. A Monte Carlo based method to estimate radiation dose from multidetector CT (MDCT): cylindrical and anthropomorphic phantoms. *Phys Med Biol.*, 50:3989–4004, 2005.

- J. J. DeMarco, C. H. Cagnon, D. D. Cody, D. M. Stevens, C. H. McCollough, M. Zankl, E. Angel, and M. F. McNitt-Gray. Estimating radiation doses from multidetector CT using Monte Carlo simulations: effects of different size voxelized patient models on magnitudes of organ and effective dose. *Phys. Med. Biol*, 52:2583–2597, 2007.
- R. L. Dixon. A new look at CT dose measurement: Beyond CTDI. *Med. Phys.*, 30 (6): 1272–1280, 2003.
- P. Downes, R. Jarvis, E. Radu, I. Kawrakow, and E. Spezi. Monte Carlo simulation and patient dosimetry for a kilovoltage cone-beam CT unit. *Med. Phys*, 36:4156–4167, 2009.
- X. Duan, J. Wang, L. Yu, S. Leng, and C. H. McCollough. CT scanner x-ray spectrum estimation from transmission measurements. *Med Phys*, 38:993–997, 2011.
- A. J. Einstein, C. D. Elliston, A. E. Arai, M. Y. Chen, Mather R., G. D. N. Pearson, R. L. DeLapaz, E. Nickoloff, A. Dutta, and D. J. Brenner. Radiation dose from single-heartbeat coronary CT angiography performed with a 320 detector row volume scanner. *Radiology*, 254:698–706, 2010.
- H. L. J. Fish and W. S. Snyder. Variation of dose delivered by ^{137}Cs as a function of body size from infancy to adulthood. *ORNL-4007*, page 221, 1966.
- W. Geraldelli, A. Tomal, and M. E. Poletti. Characterization of tissue-equivalent materials through measurements of the linear attenuation coefficient and scattering profiles obtained with polyenergetic beams. *IEEE Transactions on Nuclear Science*, 60:566–570, 2013.
- A. González, M. Mahesh, K. P. Kim, M. Bhargavan, R. Lewis, and F. Mettler. Projected cancer risks from computed tomographic scans performed in the united states in 2007. *Arch Intern Med*, 169:2071–2077, 2009.
- J. Gu, B. Bednarz, P. F. Caracappa, and X. G. Xu. The development, validation and application of a multi-detector CT (MDCT) scanner model for assessing organ doses to

- the pregnant patient and the fetus using Monte Carlo simulations. *Phys. Med. Biol.*, 54: 2699–2717, 2009.
- M.A. Habibzadeh, M.R. Ay, A.R. Kamali Asl, H. Ghadiri, and H. Zaidi. Impact of mis-centering on patient dose and image noise in x-ray CT imaging: Phantom and clinical studies. *Physica Medica*, 28:191–199, 2012.
- E. J. Hall and D. J. Brenner. Cancer risks from diagnostic radiology. *Br. J. Radiol.*, 81: 362–378, 2008.
- W. Huda, S.r Tipnis, A.r Sterzik, and U. J. Schoepf. Computing effective dose in cardiac CT. *phys. Med. Phys*, 55:3675–3684, 2010.
- IAEA TRS-398. Absorbed dose determination in external beam radiotherapy: An international code of practice for dosimetry based on standards of absorbed dose to water. *INTERNATIONAL ATOMIC ENERGY AGENCY*, 2004.
- IAEA TRS-457. Dosimetry in diagnostic radiology: An international code of practice. *INTERNATIONAL ATOMIC ENERGY AGENCY*, 2007.
- ICRP Publication 103. *Recommendations of the International Commission on Radiological Protection*. Pergamon Press, 2007.
- ICRP Publication 26. *Recommendations of the International Commission on Radiological Protection*. Pergamon Press, 1977.
- ICRP Publication 60. *Recommendations of the International Commission on Radiological Protection*. Pergamon Press, 1991.
- G. Jarry, J. J. DeMarco, U. Beifuss, C. H. Cagnon, and M. F. McNitt-Gray. A Monte Carlo-based method to estimate radiation dose from spiral CT: from phantom testing to patient-specific models. *Phys Med Biol.*, 48:2645–2663, 2003.

- A. Jensen, L. DeWerd, J. Micka, S. Davis, and W. Culberson. Air-kerma length calibration of CT ionization chambers. (*abstract*) *Med. Phys.*, 33(6):2006, 2006.
- K. A. Jessen, P. C. Shrimpton, J. Geleijns, W. Panzer, and G. Tosi. Dosimetry for optimisation of patient protection in computed tomography. *Appl Radiat Isot*, 50:165–172, 1999.
- K. A. Jessen, W. Panzer, and P. C. Shrimpton. *European Guidelines on quality criteria for computed tomography*. Brussels, Belgium: European Commission, 2000.
- H. Jiang and H. Paganetti. Adaptation of GEANT4 to Monte Carlo dose calculations based on CT data. *Med. Phys.*, 31:2811–2818, 2004.
- M. K. Kalra, M. M. Maher, T. L. Toth, B. Schmidt, B. L. Westerman, H. T. Morgan, and S. Saini. Techniques and applications of automatic tube current modulation for CT. *Radiology*, 233:649–657, 2004.
- I. Kawrakow. Accurate condensed history Monte Carlo simulation of electron transport. II. Application to ion chamber response simulations. *Med. Phys.*, 27:499–513, 2000.
- A. Khursheed, M. C. Hiller, P. C. Shrimpton, and B. F. Wall. Influence of patient age on normalized effective doses calculated for CT examinations. *Br. J. Radiol.*, 75:819–30, 2002.
- B. Li and R. H. Behrman. Comment on the “Report of AAPM TG 204: Size-specific dose estimates (SSDE) in pediatric and adult body CT examinations”. *Med. Phys.*, 37:4613–4614, 2012.
- X. Li, E. Samei, and W. P. Segar. Patient-specific radiation dose and cancer risk estimation in CT: Part I. Development and validation of a Monte Carlo program. *Med. Phys.*, 38:397–407, 2011a.

- X. Li, E. Samei, and W. P. Segar. Patient-specific radiation dose and cancer risk estimation in CT: Part II. Application to patients. *Med. Phys.*, 38:408–419, 2011b.
- Q. Liang and L. A. DeWerd. The influence of readout parameters on the TL dose response of TLD100. *Med Ph*, 36:2585, 2009.
- C.-M. Ma, C. W. Coffey, L. A. DeWerd, C. Liu, R. Nath, S. M. Seltzer, and J. P. Seuntjens. AAPM protocol for 40–300 kV x-ray beam dosimetry in radiotherapy and radiobiology. *Med. Phys.*, 28:868–893, 2001.
- K. Maeda, M. Matsumoto, and A. Taniguchi. Compton-scattering measurement of diagnostic x-ray spectrum using high-resolution schottky CdTe detector. *Med. Phys.*, 32:1542–1547, 2005.
- G. Matscheko and G. A. Carlsson. Compton spectroscopy in the diagnostic x-ray energy range. I. spectrometer design. *Phys. Med. Biol.*, 34:185–198, 1989.
- G. Matscheko and R. Ribberfors. A generalized algorithm for spectral reconstruction in Compton spectroscopy with corrections for coherent scattering. *Phys. Med. Biol.*, 34:835–841, 1989.
- G. Matscheko, G. A. Carlsson, and R. Ribberfors. Compton spectroscopy in the diagnostic x-ray energy range. II. effects of scattering material and energy resolution. *Phys. Med. Biol.*, 34:199–208, 1989.
- C. H. McCollough, M. R. Bruesewitz, and J. M. Kofler. CT dose reduction and dose management tools: Overview of available options. *Radiographics*, 26:503–512, 2006.
- C. H. McCollough, S. Leng, L. Yu, D.D. Cody, J. M. Boone, and M. F. McNitt-Gray. CT dose index and patient dose: they are not the same thing. *Radiology*, 259:311–316, 2011.

- S. E. McKenney, A. Nosratieh, D. Gelskey, K. Yang, S. Huang, L. Chen, and J. M. Boone. Experimental validation of a method characterizing bow tie filters in CT scanners using a real-time dose probe. *Med P*, 38:1406–1415, 2011.
- J. D. Moga. *Characterization of low-energy photon-emitting brachytherapy sources and kilovoltage x-ray beams using spectrometry*. PhD thesis, UW-Madison, 2011.
- NCRP Report 160. Ionizing radiation exposure of the population of the united states. Technical report, National Council on Radiation Protection and Measurements, 2006.
- NRC. EGSnrc distribution site. <http://www.irs.inms.nrc.ca/EGSnrc/EGSnrc.html>, 2009.
- A. A. Nunn, S. D. Davis, J. A. Micka, and L. A. DeWerd. LiF:Mg,Ti TLD response as a function of photon energy for moderately filtered x-ray spectra in the range of 20–250 kVp relative to ^{60}Co . *Med. Phys.*, 35:1859–1869, 2008.
- N. Petoussi-Hens, M. Zankl, U. Fill, and D. Regulla. The GSF family of voxel phantoms. *Phys. Med. Biol.*, 47:89–106, 2002.
- G. Poludniowski, G. Landry, F. DeBlois, P. M. Evans, and F. Verhaegen. SpekCalc: a program to calculate photon spectra from tungsten anode x-ray tubes. *Phys. Med. Biol.*, 54:N433–N438, 2009.
- G. G. Poludniowski. Calculation of x-ray spectra emerging from an x-ray tube. Part II. X-ray production and filtration in x-ray targets. *Med. Phys.*, 34(6):2175–2186, 2007.
- G. G. Poludniowski and P. M. Evans. Calculation of x-ray spectra emerging from an x-ray tube. Part I. Electron penetration characteristics in x-ray targets. *Med. Phys.*, 34(6): 2164–2174, 2007.
- D. K. Rex, D. Vining, and K. K. Kopecky. An initial experience with screening for colon polyps using spiral CT with and without CT colography (virtual colonoscopy). *Gastroin-test Endosc.*, 50:309–313, 1999.

- R. Schmidt, J. Wulff, B. Kästner, D. Jany, J. T. Heverhagen, M. Fiebich, and K. Zink. Monte Carlo based calculation of patient exposure in x-ray CT examinations. *IFMBE Proceedings*, 25(632-634):632–634, 2009.
- W. W. Seelentag and W. Panzer. Stripping of x-ray bremsstrahlung spectra up to 300 kVp on a desk type computer. *Phys. Med. Biol.*, 24(4):767–780, 1979.
- C. Y. Shi and X. G. Xu. Development of a 30-week-pregnant female tomographic model from CT-images for Monte Carlo organ dose calculations. *Med Phys*, 31:2491–2497, 2004.
- P. C. Shrimpton, M. C. Hillier, M. A. Lewis, and M. Dunn. Doses from computed tomography (CT) examinations in the UK: 2003 review. Technical report, report NRPB-W67, 2005.
- Siemens. Guide to low dose.
- R. Smith-Bindman, J. Lipson J, R. Marcus, K.P. Kim, M. Mahesh, R. Gould, A. Berrington de González, and D.L. Miglioretti. Radiation dose associated with common computed tomography examinations and the associated lifetime attributable risk of cancer. *Arch Intern Med*, 146:2078–2086, 2009.
- G. Stamm and H. D. Nagel. CTexpo-a novel program for dose evaluation in CT. *Rofo.*, 174:1570–1576, 2002.
- K. J. Strauss and M. J. Goske. Estimated pediatric radiation dose during CT. *Pediatr. Radiol.*, 41 Suppl 2:472–482, 2011.
- R. E. P. Taylor, G. Yegin, and D. W. O. Rogers. Benchmarking BrachyDose: Voxel based EGSnrc Monte Carlo calculations of TG-43 dosimetry parameters. *Med Phys*, 34:445–457, 2007.
- A. C. Turner, D. Zhang, H. J. Kim, J. J. DeMarco, C. H. Cagnon, E. Angel, D. D. Cody, D. M. Stevens, A. N. Primak, C. H. McCollough, and M. F. McNitt-Gray. A method

- to generate equivalent energy spectra and filtration models based on measurement for multidetector CT Monte Carlo dosimetry simulations. *Med. Phys.*, 36(6):2154–2164, 2009.
- X-5 Monte Carlo Team. *MCNP — A General Monte Carlo N-Particle Transport Code, Version 5, Report LA-UR-03-1987*. Los Alamos National Laboratory, Los Alamos, NM, 2005.
- X. George Xu and Keith F. Eckerman. *Handbook of anatomical models for radiation dosimetry*. CRC press, 2009.
- M. Yaffe, K. W. Taylor, and H. E. Johns. Spectroscopy of diagnostic x-rays by a compton scatter method. *Med. Phys.*, 3:328–334, 1976.
- L. Yu, X. Liu, S. Leng, J. M. Kofler, J. C. Ramirez-Giraldo, M. Qu, J. Christner, J. G. Fletcher, and C. H. McCollough. Radiation dose reduction in computed tomography: techniques and future perspective. *Imaging Med*, 1:65–84, 2009.
- D. Zhang, A. S. Savandi, J. J. Demarco, C. H. Cagnon, E. Angel, A. C. Turner, D. D. Cody, D. M. Stevens, A. N. Primak, C. H. McCollough, and M. F. McNitt-Gray. Variability of surface and center position radiation dose in mdct: Monte carlo simulations using ctdi and anthropomorphic phantoms. *Med Phys*, 36:1025–1038, 2009.